

Cranfield University

Paul Michael Jones

Nanoparticle Synthesis via Thin Film Ferroelectric Templates:  
Surface interactions and effects

School of Applied Sciences

PhD

# Cranfield University

School of Applied Sciences

PhD Thesis

2008

Paul Michael Jones

Nanoparticle Synthesis via Thin Film Ferroelectric Templates:  
Surface interactions and effects

Supervisor: Dr Steve Dunn

Academic Year 2006 to 2008

Dedicated to the memory of Carole Dunn,

Brave to the last.

## Abstract

An investigation into the processes taking place at the surface interface of ferroelectric  $\text{Pb}(\text{Zr}_{1-x}\text{Ti}_x)\text{O}_3$  immersed in metal salt solution under ultraviolet illumination is presented. The semiconducting and switchable dipolar nature of this material allows the spatial separation and control of photo-induced reduction and oxidation across its surface interface. These properties can be of application in novel techniques such as the controlled growth of metallic nanoparticles across specific polar domains.

70nm thick  $\text{Pb}(\text{Zr}_{0.3}\text{Ti}_{0.7})\text{O}_3$  samples, PZT(30/70), are manufactured using the sol gel methodology, two crystallographic orientations being produced. The orientation being controlled by the substrate used; Si was used for [111] orientation and MgO for [100]. The initial work with wideband ultraviolet light shows that the reduction and growth of silver on the PZT surface is greatly influenced by the structure of the film.

The crystallographic orientation of the film affects metal deposition such that on [111] films the metal deposits only on positive domains, where as the [100] films experience deposition on both positive and negative domains. This is shown to be due to the difference in width of the space charge region,  $\Delta w = 4.4\text{nm}$ , between the [111] and [100] samples so that the negative domain on [100] samples have  $10^{19}$  times higher chance of electron tunnelling compared to the [111]. It is also shown that grain boundaries have the greatest effect on the growth of metal, with a metal cluster growth rate 51 times faster than elsewhere on the surface. This increased rate of growth is due to the effect a grain boundary has on the surrounding area, the energy band bending at the boundary attracting charge carriers from the grains around it. The interface types ranked from greatest to lowest influence are grain boundaries, positive domains, domain boundaries and finally interphase boundaries.



It is shown that the stern layer, strongly adsorbed charged ions of opposite sign to the surface charge, at the PZT/solution interface act as an insulating layer to metal reduction. The accumulation of photoexcited charge carriers at points along grain boundaries causes the surface potential gradient to alter and allows metal reduction and thus clusters to nucleate. The energy required to cause this variation is investigated by use of narrow band, 5nm bandwidth, ultraviolet. For energy from 4.4eV to 5 eV, it is found there is an increase in the average silver cluster cross sectional area by a ratio of *ca* 1.6 to 1 for both the [111] and [100] orientations of PZT.

Finally it is shown that the type of metal salt used in the photochemical process affects the type of reaction that takes place at the sample surface. For a cation to reduce on positive domains its reduction potential needs to be below the bottom edge of the conduction band of PZT. Chloride salts, that sit above the conduction band, cause decomposition of the negative domains. Use is made of these effects to find the position of the bottom of the conduction band for PZT. It is found that across similar [111] PZT samples  $\text{FeCl}_2$  can both reduce on positive domains and decompose negative domains, this puts the bottom of the conduction band for PZT(30/70) between 4.06 and 4.36 eV from vacuum. It is also discovered that the type of anion affects the decomposition of the negative domains. Nitrate salts with cations above the conduction band cause no decomposition whereas chlorides do. The decomposition is shown to be the loss of Pb from the negative surface.

Keywords:

Semiconductor, Lead-Zirconate-Titanate, Grain Boundaries, REDOX, Band Bending

## Acknowledgements

I wish to thank Dr Steve Dunn for his help, support and supervision and Dr Diego Gallardo for his invaluable support during this work.

I also send thanks to the following people: Dr Rob Dorey, Mr Andrew Stallard, Dr Chris Shaw, Ms Enza Giaracuni, Prof. Roger Whatmore, Ms Divya Tiwari, Dr Glen Leighton, Dr Qi Zhang, Mr Rob Evans, Dr Scott Harada, Dr Hannah Gardner, Mr Matthew Taunt, Dr Matthew Kershaw, Ms Christine Kimpton, Dr Sophie Rocks, Mr Andrew Dyer and Dr Heather Almond.

Special thanks also go to my family for their love and support, particularly to Julie who allowed me to do this work and who has been more than patient.

# Table of Contents

1	Introduction.....	1
2	Literature Review.....	3
2.1	Ferroelectricity.....	3
2.2	PZT Film growth and structure.....	6
2.3	Orientation and bulk properties .....	8
2.4	Semiconducting properties.....	9
2.5	Energy Band Bending.....	14
2.6	Grain boundaries.....	19
2.7	Electrical Double Layer .....	23
2.8	Photoelectrochemistry at ferroelectric surfaces .....	25
2.9	Objectives .....	31
3	Methodology.....	33
3.1	Samples Used.....	33
3.2	PZT Film Preparation .....	35
3.2.1	Pt Deposition.....	35
3.2.2	PZT Deposition.....	35
3.3	Reference marks on samples.....	35
3.4	Metal Salts and solutions .....	36
3.4.1	Metal salts .....	36
3.4.2	Tollens Reagent .....	37
3.5	AFM poling.....	37
3.6	PFM Characterisation .....	39
3.7	Spectral characterisation .....	40
3.7.1	Transmittance spectra of salts.....	40
3.7.2	Transmittance spectra of Ag films.....	40
3.8	UV Exposure Unit.....	41
3.8.1	Enclosure and cooling.....	41
3.8.2	UV lamps .....	41
3.9	Irradiation experiments .....	43
3.9.1	Stainless steel chamber preliminary tests .....	43
3.9.2	GI PZT Samples.....	43
3.9.3	PZT[111] Samples .....	44
3.9.4	PZT[100] Samples .....	44
3.9.5	Monochromatic UV Wavelength experiments .....	44
4	Film structure and metal reduction .....	46
4.1	Ag wire formation.....	46
4.2	Metal growth on PZT [111] .....	47
4.3	Growth at grain boundaries.....	50

4.4	Boundary effect ranking .....	55
4.5	Crystallographic orientation and metal deposition .....	57
4.6	Effect of illumination on band bending and Ag deposition .....	61
5	Photon energy dependence of metal reduction .....	67
5.1	Ag <sup>0</sup> Cluster size and density .....	67
5.2	Grain boundaries and the Stern layer .....	71
6	Reduction potential and band structure .....	79
6.1	Salt selection .....	79
6.2	Salts within PZT bandgap .....	82
6.3	Chlorides and nitrates with cation reduction potential above conduction band	83
6.4	Oxidation on negative domains .....	90
7	Conclusions and Future work .....	94
7.1	Conclusions .....	94
7.2	Future work .....	96
8	REFERENCES .....	97
	Appendixes .....	106

## Table of Figures

Figure 2.1 ABO <sub>3</sub> unit cell where A and B are both cations. ....	3
Figure 2.2 Phase diagram for PbZr <sub>1-x</sub> Ti <sub>x</sub> O <sub>3</sub> (Cross and Hardtl, 1984). ....	4
Figure 2.3 Ferroelectric hysteresis curve, with axis of applied electric field E, and the polarisation P. $\pm E_c$ is the coercive field, $\pm P_s$ the saturation polarisation and $\pm P_r$ the remnant polarisation. ....	5
Figure 2.4 Convention used for signifying polarisation direction and how it relates to the dipole moment and coercive field, $E_c$ . $C^-$ is the negative surface and $C^+$ the positive. By switching $E_c$ the dipole switches and the polarisation reverses. ....	5
Figure 2.5 AFM images of PZT(30/70) samples on different substrates, (a) PZT on unseeded ITO/glass has large, 15 $\mu$ m rosettes, (b) PZT on seeded ITO/glass gives a grain structure down to 160nm and (c) the PZT grown on Pt on Si[111] 70-100nm grains which are also columnar, (Jones, 2003). ....	7
Figure 2.6 Schematic of 4 unit cells from ABO <sub>3</sub> ferroelectric, the centre black ion is in the same off-centre position for all cells thus the polarisation direction is as the arrow shows. ....	7
Figure 2.7 Orientation dependence of (a) $d_{33}$ and (b) $\epsilon_{33}$ . The $d_{33}$ for PZT is at its maximum in the [001] orientation and its drops off as the angle increases (Du <i>et al.</i> , 1998). The $\epsilon_{33}$ is at its minimum in the [001] orientation (Du <i>et al.</i> , 1997). ....	8
Figure 2.8 Photocurrent versus time for PZT irradiated with pulsed UV through transparent electrodes. The direction of current flow is dependent on polarisation of film, shown are positive, negative and unpoled films as presented by Kholkin <i>et al.</i> (2001). ....	10
Figure 2.9 Plot of photocurrent in PZT film during pulsed UV irradiation with applied dc bias to film in same direction as polarisation from Kholkin <i>et al.</i> (2001). At low bias, 0-13 kV/cm, the photocurrent flow is in same direction as when no bias was applied. Above 13 kV/cm, but below $E_c$ , the photocurrent direction switches and becomes independent of polar direction. ....	11
Figure 2.10 Photovoltage against time for PZT under illumination obtained by Inoue <i>et al.</i> (1989). Voltage polarity is dependent on film polarisation. ....	12
Figure 2.11 Excitation of electron from valence band into conduction band by super bandgap photon. ....	13
Figure 2.12 Band bending at ferroelectric surface due to film polarisation and the formation of a space charge region, SCR. ....	15
Figure 2.13 Plots taken from Matsuura (2000) comparing band bending between a 'normal' non-polar semiconductor (dashed line) to that of a ferroelectric (solid line) as dielectric constant $\epsilon_r$ is changed. Left $\epsilon_r = 10$ , and Right $\epsilon_r = 100$ . ....	17
Figure 2.14 Accumulation of holes at surface of semiconductor due to a field applied out of the surface. The bottom plot shows the charge density moving from the surface into the bulk, the surface charge being due to holes. (From Fraser (1986)). ....	18
Figure 2.15 Inversion layer at surface of semiconductor due to a field applied into the surface. The bottom plot shows the charge density moving from the surface into the bulk, the charge being due to migrating electrons. (From Fraser (1986)). ....	19

Figure 2.16 Band bending at grain boundaries. Top images shows band bending, and lower images shows the charge density, $\rho$ , moving away from the grain boundary on both sides. The left image shows bending at positively charged grain boundaries, the charge is made up of electrons attracted to the boundary forming a depletion region and then an inversion region. The right hand side show the bending at a negatively charge boundary, the charge here made up of holes.....	20
Figure 2.17 Positions for electrodes used in Lee <i>et al.</i> work (Lee and Joo, 2002), A is within the grain, B is at the interface between two grains and C is at the intersection of 4 grains.....	22
Figure 2.18 hysteresis curves, left, and dielectric constant measurements, right, obtained by Lee and Joo, (2002) are presented. Curve A was the loop taken within the grain, curve B was taken at the boundary between two grains and curve C was taken at the intersection of 4 grains. In the right hand plot the circles represent to the dielectric constant and the squares $P_r$ . ....	22
Figure 2.19 Electrical double layer formed at the surface of a ferroelectric, left is $C^-$ domain and right is $C^+$ domain. The inner Helmholtz plane (IHP) is formed of species with a counter charge to the surface, followed by the outer Helmholtz plane (OHP) consisting of species of opposite charge to the IHP, these form the Stern layer. Following the stern layer is a diffusion region where the charged species concentrations reduce with distance form the surface, the region between the diffusion and OHP is a slip plane (SP). ....	24
Figure 2.20 Illustrative plot of electrical double layer formed at a negatively charged surface. SL is the end of the stern layer made up of the inner and outer Helmholtz planes. SP is the slip plane between fixed ions at the surface and the diffusion layer. It can be seen that the potential, $V$ , drops as the distance, $x$ , increases. It should also be noted that the drop is not linear but has different extinction characteristics depending on which layer it is in. ....	25
Figure 2.21 Image (a) PFM image of university of Pennsylvania crest on PZT, (b) Ag reduced onto $C^+$ domain surface by Bonnell and Kalinin (2002). The metal has grown as an area of independent nanoparticles. ....	28
Figure 2.22 (a) PFM image of Z shaped $C^+$ domains on Single crystal $\text{LiNbO}_3$ , (b) Ag wires deposited at domain boundaries (Hanson <i>et al.</i> , 2006). ....	29
Figure 2.23 Calculated potential at surface of lithium niobate (Hanson <i>et al.</i> , 2006), the potential peaks at the domain boundaries and reduces as the centre of the domains is approached.....	30
Figure 2.24 Plot of the Density of states for PZT as modelled by Silva <i>et al.</i> (2005). Each row represents the states provided by each of the elements within the PZT film. The bottom row shows the total DOS from all elements, the left hand side of the plot is the valence band. It can be seen that the DoS in the valence band is greater at points deeper into the band than near the edge of the bandgap. A photon of higher energy than the bandgap is required to generate electron hole pairs in any sufficient quantity. ....	31
Figure 3.1 AFM image of GI1 sample consisting of individual perovskite rosettes (Dark circles) surrounded by pyrochlore phase. ....	34
Figure 3.2 SEM of grain structure of 70nm thick PZT on PZT[111], grain size varies from 100 nm down. The 70 nm thick PZT[100] sample was of a similar structure. ....	34
Figure 3.3. Reference pattern FIB milled into surface of samples. ....	36

Figure 3.4. AFM configuration for poling PZT thin films. This setup will pole a $C^-$ domain, for a $C^+$ domain the wires to the PSU are switched. ....	38
Figure 3.5. Schematic of modified cantilever holder viewed from the top. The track at the top of the holder is cut and a trailing wire soldered to the track connected to the pin on the top left. ....	38
Figure 3.6. Poled pattern on PZT surface showing $C^+$ and $C^-$ domains, outside of the poled area the domains are random as grown, shown by the gray surround. ....	39
Figure 3.7. Set up of Atomic force microscope in piezoresponse mode, for polar domain characterisation. ....	40
Figure 3.8 UV irradiation chamber. ....	41
Figure 3.9. Normalised intensities for Honle Hg UV lamp (H-lamp) used in irradiation experiments. ....	42
Figure 3.10. Normalised intensities for Honle Fe doped Hg UV lamp (F-lamp) used in irradiation experiments. ....	42
Figure 3.11. Stainless steel block mounted onto sample as fluid holding chamber. ....	43
Figure 3.12. Setup of wavelength test equipment. ....	45
Figure 3.13. End attachment to position output fibre over PZT sample. ....	45
Figure 4.1 Ag wires formed in steel chamber during UV irradiation. It is believed they grew on step defects on the chamber walls and then fell to the surface of the PZT. ....	46
Figure 4.2 Preferential deposition of Ag clusters across the surface of a $C^+$ domain of PZT[111] 30/70 thin film after 20 minutes. ....	48
Figure 4.3 Single cluster on $C^+$ PZT domain. Electrons photoexcited in PZT film migrate to the surface of a $C^+$ domain. Where a cluster is growing the electrons near the edge migrate into it. These free electrons can then reduce the $Ag^+$ ions from solution to $Ag^0$ on the cluster surface, thus it grows both sideways and outwards. ....	49
Figure 4.4 Transmittance spectra for light through ca 2 nm Ag film. Up to 95 % of the UV above 4.5 eV is blocked. ....	49
Figure 4.5 Ag cluster growth retardation mechanism, clusters nucleate and grow as electrons migrate to the surface due to UV irradiation. As the clusters grow they shade the surface from the light until their edges meet and the surface is totally masked, which causes electron migration to stop. ....	50
Figure 4.6 AFM (left) and PFM (right) images of single perovskite rosette surrounded by pyrochlore phase on GI1 film after 2 minute UV irradiation. The Ag clusters are mainly on the $C^+$ domain, white area in PFM image, within the rosette and no clusters have formed in the pyrochlore phase. ....	51
Figure 4.7 Transmittance of 0.01 M $AgNO_3$ solution, photons with energy lower than 4.9 eV can pass with little absorption, but energies above this are strongly blocked by the solution. This means that 5 eV is the maximum photon energy incident to the surface of the PZT during irradiation. ....	52
Figure 4.8 AFM images of GI1 sample before (left) and after (middle) 45 seconds of UV exposure in $AgNO_3$ solution. Large Ag clusters have grown at the grain boundary between the two connecting rosettes, there are also some smaller clusters on some areas of the $C^+$ domains. On the right is the piezoresponse force image of the same area, showing $C^+$ , and $C^-$ polarisation. ....	52
Figure 4.9 AFM image of Ag growth on a line defect in the grain structure of a single rosette after 45 seconds exposure. ....	53

Figure 4.10 Migration of electrons in the PZT to grain boundaries during irradiation. The internal electric field due to the lattice mismatch at the core causes downward band bending at the grain boundary and thus electrons migration to it.....	54
Figure 4.11 The four types of boundary found on the GI1 PZT sample, A) interphase boundaries where the perovskite and pyrochlore phases meet , B) grain boundaries where the edges of the rosettes meet, C) domain boundaries where polar domains meet, and D) surface state effects and domain polarization. ....	55
Figure 4.12 Silver deposition on the surface of PZT(30/70) after 20 minutes exposure to the H-lamp. Left, PZT[100] with highly [100] orientated structure has cluster growth across both domains, the dashed line showing the interface between the $C^+$ and $C^-$ domains. Right, PZT[111] with highly [111] crystallographic orientation displays definite demarcation between $C^+$ domains where clusters have grown and the $C^-$ where there is no growth. ....	57
Figure 4.13 Comparative diagram of energy band bending at $C^-$ domain surface of PZT[111] and PZT[100]. The space charge regions are such that $SCR_{[111]} > SCR_{[100]}$ due to the greater curvature of the PZT[100] band bending.....	59
Figure 4.14 Ag deposition on PZT[100] sample after 20 minutes UV irradiation. Left, H-lamp illumination gives growth across both $C^+$ and $C^-$ domains. Right, F-lamp illumination gives deposition on $C^+$ domain only. ....	62
Figure 4.15 Plot of ratio of intensity between H-lamp and F-lamp versus wavelength. ....	63
Figure 4.16 Band diagrams for PZT immersed in $AgNO_3$ solution. As photon flux increase so the steepness of the band bending increases, this in turn leads to a narrower SCR.....	65
Figure 5.1 $C^+$ domain on [111] orientated PZT 30/70, after irradiation with 4.1 eV (Left) and 5 eV (Right) UV. ....	68
Figure 5.2 $C^+$ domain on [100] orientated PZT 30/70, after irradiation with 4.4 eV (left) and.....	68
Figure 5.3 Ag cluster size v photon wavelength and energy for the [111] and [100] samples.....	69
Figure 5.4 Apparent change in Ag cluster density on $C^+$ domains verses photon energy.....	70
Figure 5.5 According to work by Lei <i>et al.</i> (2004) the surface density of the Ag clusters increased with irradiation time. ....	70
Figure 5.6 Stern layer disturbance due to a PZT surface anomaly and cluster nucleation. (A) Under equilibrium conditions, i.e. no photoexcitation, the inner Helmholtz layer, consisting of $NO_3^-$ anions, acts as a barrier to the $Ag^+$ cations. (B) Upon UV illumination migrating photoexcited electrons cause a change in the local surface potential of the anomaly. (C) $Ag^+$ cations are attracted to the anomaly surface and reduce forming the initial nucleation point. ....	73
Figure 5.7 Simplified illustration of surface potential along a grain boundary. The variations in stoichiometry and surface morphology of the grain boundary (Top) affect the surface potential along its axis A-A (Bottom). ....	74
Figure 5.8 PZT surface after 30 minute irradiation with H-lamp wideband UV, it can be seen that the clusters vary in size.....	76
Figure 5.9 Wavelength dependence of silver deposition on PZT as presented by Lei <i>et al.</i> (2004).....	78



Figure 6.1 Standard hydrogen potential, $E_0$ , against absolute energy (Trasatti, 1986) displaying reduction potentials of the salts used with respect to the PZT band edges. PZT band edge values taken from Scott (1999).....	81
Figure 6.2 $\text{Sn}^0$ reduced onto the $\text{C}^+$ domains on PZT[111] film after irradiation with the H-lamp. ....	83
Figure 6.3 SEM image of PZT where the $\text{C}^-$ domain shows signs of photocorrosion by the $\text{FeCl}_2$ solution. ....	84
Figure 6.4 High magnification SEM image of PZT[111] $\text{C}^-$ domain showing photocorrosion by $\text{FeCl}_2$ solution. ....	85
Figure 6.5 XPS results for Pb in PZT[111] sample before and after UV irradiation in 0.01M $\text{AlCl}_3$ solution. It shows that there is a reduction in Pb content after irradiation has taken place. ....	85
Figure 6.6 SEM image of PZT where the $\text{C}^-$ domain shows signs of photocorrosion by $\text{FeCl}_2$ solution. ....	86
Figure 6.7 SEM image of Fe deposited on $\text{C}^+$ domain from $\text{FeCl}_2$ solution.....	86
Figure 6.8 Location of the reduction potential of $\text{Fe}^{2+}$ with respect to the conduction band in PZT showing an uncertainty region in the location of the conduction band edge at the surface. The actual position of this edge with respect to the $\text{Fe}^{2+}$ ion will result in either metal reduction, band above ion, or corrosion, band below ion. ....	87
Figure 6.9 SEM image of Mn oxide on $\text{C}^-$ domains of PZT[111] samples using (Left) $\text{Mn}(\text{NO}_3)_2$ salts and (Right) $\text{MnCl}_2$ salts. ....	91
Figure 6.10 Cu oxide formed on $\text{C}^-$ domain from $\text{CuCl}_2$ solution, larger objects are Cu clusters across most of the surface. ....	92

## Table of Tables

Table 3.1 Settings for Cookson G3-8 spin coater. ....	35
Table 3.2 Settings used for FIB of reference marks onto samples .....	36
Table 3.3 Metal salts used in experimentation.....	37
Table 4.1 Ranking of boundary types with respect to Ag cluster growth rate on PZT 56	
Table 6.1 Standard reduction potentials for metal salts used.....	80

## Table of Equations

Equation 2.1 .....	15
Equation 2.2 .....	15
Equation 2.3 .....	15
Equation 2.4 .....	16
Equation 2.5 .....	16
Equation 2.6 .....	17
Equation 2.7 .....	24
Equation 4.1 .....	58
Equation 4.2 .....	59
Equation 4.3 .....	60
Equation 4.4 .....	60
Equation 4.5 .....	60
Equation 4.6 .....	61
Equation 4.7 .....	63
Equation 4.8 .....	63
Equation 4.9 .....	64
Equation 4.10 .....	64
Equation 5.1 .....	72
Equation 6.1 .....	82
Equation 6.2 .....	82
Equation 6.3 .....	82
Equation 6.4 .....	90
Equation 6.6 .....	92

# 1 Introduction

Nanoparticles are defined as particles that have dimensions less than 100 nm. Due to their size nanoparticles have different quantum mechanical properties to that seen in the bulk material (Ozin and Arsenault, 2005). Though nanoparticles have always existed in nature, for example in smoke and soot, there is much interest in growing them artificially. From the Mesopotamians and ancient Egyptians (Hatton *et al.*, 2008) to the renaissance (Padovani *et al.*, 2003), nanoparticles have been used to give colour and lustre to pottery and glass, and cosmetics (Walter *et al.*, 2006). More recently, uses have been found for nanoparticles in areas such as light emitting diodes (Bertoni *et al.*, 2007), bio-markers in medical applications (Azzazy *et al.*, 2006), and sun block cream (Popov *et al.*, 2005).

The usefulness of nanoparticles is also down to their large surface area to volume Ratio which makes them particularly reactive at the surface. This property makes them ideal for use as catalysts (Tryk *et al.*, 2000) in the reduction of other materials. For example much use is made of TiO<sub>2</sub> nanoparticles in the purification of water (Byrne *et al.*, 2002; Beydoun *et al.*, 1999; Chen and Ray, 2001) and Fe nanoparticles in environmental remediation (Zhang, 2003).

Currently the majority of nanoparticle synthesis techniques are limited by the types of shape that can be grown. In many applications only spherical nanoparticles are required, but if more complex systems are to be developed, methods that can create a variety of shapes are needed (Jana, 2004). The idea of building up complex systems is also linked to the concept of synthesising individual building blocks for assembly. Khomutov *et al.* (2003) for example talks of structures created using supramolecular building blocks, DNA and nanoparticles, though they are mainly referring to planar 2D structures.

Triangular and Hexagonal CdS nanocrystals have been grown by Warner and Tilley (2005) using colloidal chemistry and it was found that when the solution was evaporated onto a substrate, the crystals self-assembled into structures, the type of structure depending on the molarity of the solution. The ability to produce and assemble shaped nanoparticles will facilitate the creation of functional nanostructured systems (Sun *et al.*, 2006) in areas as diverse as electronics, optics, biology and sensors.

Work by groups such as Yamamoto *et al.* (2005) on Au Star growth and Zhong *et al.* (2005) on dumbbell shaped MnO have shown that it is possible to grow complex morphologies. The drawback of these processes is that they are only capable of growing one type of shape, therefore they would have to be part of an arsenal of processes, one for each morphology. A possible method of growing nanoparticles of various morphologies in one process has been suggested by Bonnell and Kalinin (2002). This process is based on the ability of ferroelectric materials such as lead-zirconate-titanate and barium-titanate to reduce metal salts at domain specific sites. Under UV illumination it has been found that certain metal salts will be preferentially reduced to metal on positive domains. By poling specific shapes on the surface of the ferroelectric it could be possible to grow nanoparticles of specific shape and size.

Although some initial work has been undertaken into this process not much is understood about the processes taking place at the metal salt solution/ferroelectric interface. The purpose of this study is to investigate the chemical and physical interactions that are taking place in order to eventually optimise the process of metal particle growth.

## 2 Literature Review

### 2.1 Ferroelectricity

A ferroelectric is defined as a dielectric, or electrically polarisable material, in which the polarisation direction can be reoriented into symmetrically equivalent states by the application of an electric field, E-field (Jaffe *et al.*, 1971). Various forms of ferroelectric material exist, a subset of which are the  $ABO_3$ -based perovskites (Wang and Zhong, 2002) such as barium titanate,  $BaTiO_3$ , and lead zirconate titanate,  $Pb(Zr_{1-x},Ti_x)O_3$ , also known as PZT.  $ABO_3$  perovskites have a unit cell as in Figure 2.1, the oxygen atoms forming an octahedral array, with smaller off centre ions that occupy the central B sites. The interstitial A sites are filled by larger ions. In PZT the A ion is Pb and the B ion is Ti or Zr, in  $BaTiO_3$  A is Ba and B is Ti.

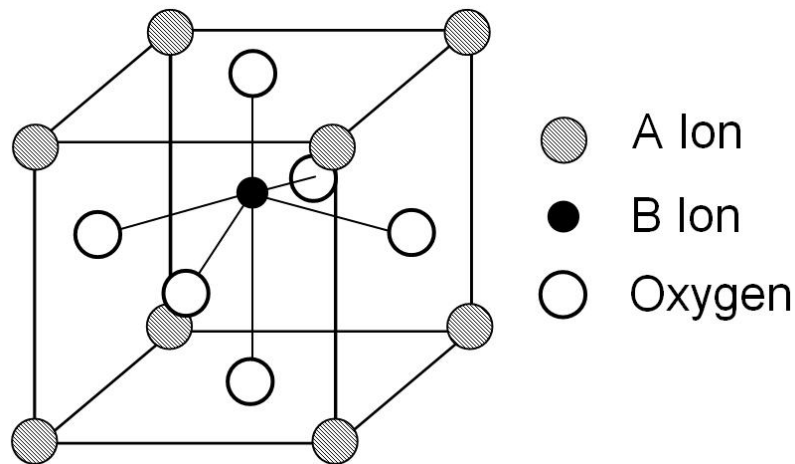


Figure 2.1  $ABO_3$  unit cell where A and B are both cations.

The ferroelectric phenomena in these materials are dependent on various factors such as the curie temperature,  $T_c$ , (Cross and Hardtl, 1984) i.e. the temperature where the unit cell morphology changes, and stoichiometry, for PZT this would be the Zr/Ti and PbO ratios. Figure 2.2 shows a phase diagram for PZT with temperature against stoichiometry and its link to unit cell morphology. It can be seen that as the Ti/Zr Ratio

changes so the morphology of the unit cell alters. As an example a ratio of 30% Zr to 70% Ti, written as PZT (30/70), will give a tetragonal unit cell that is ferroelectric up to about 430°C. Over this temperature it becomes a paraelectric centrosymmetric cubic structure, i.e. it is non ferroelectric as the B ion is centralised. If the Zr/Ti ratio were switched, as in PZT(70/30), then a rhombohedral unit cell exists that is ferroelectric up to about 350°C, at which point it changes to the paraelectric cubic structure again.

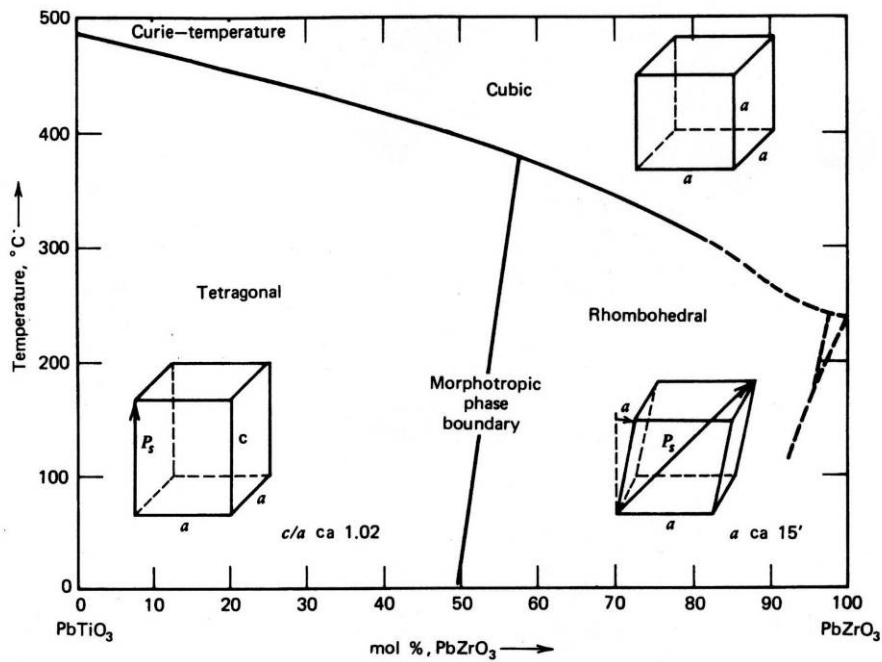
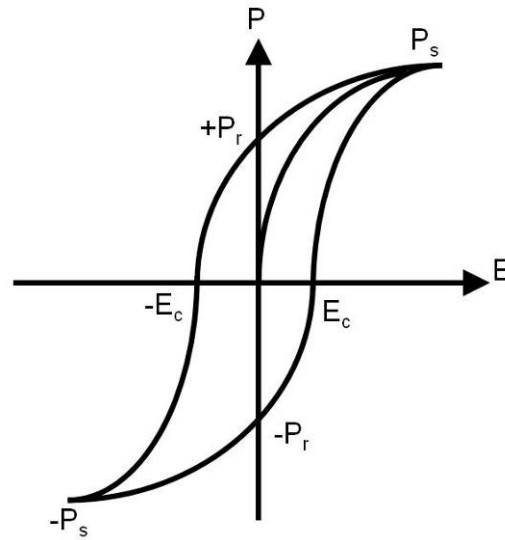


Figure 2.2 Phase diagram for  $\text{PbZr}_{1-x}\text{Ti}_x\text{O}_3$  (Cross and Hardtl, 1984).

An electric field, E-field, applied across the ferroelectric causes domains perpendicular to that field to align. When the E-field reaches certain amplitude the polarisation of the sample will saturate,  $P_s$ , this occurs as the majority of domains have orientated in the field direction, Figure 2.3. On removal of the E-field, the crystal settles into its remnant polarisation,  $P_r$ . The polarisation of the domain can be switched by inverting the applied E-field. The E-field strength required to make the net polarisation zero is called the coercive field,  $E_c$ .



**Figure 2.3** Ferroelectric hysteresis curve, with axis of applied electric field  $E$ , and the polarisation  $P$ .  $\pm E_c$  is the coercive field,  $\pm P_s$  the saturation polarisation and  $\pm P_r$  the remnant polarisation.

Figure 2.4 shows the convention used for polarisation direction and applied field. In this work the bottom of the sample is set as the base electrode and therefore domain polarisation negative,  $C^-$ , and positive,  $C^+$ , is referenced with respect to the top surface.

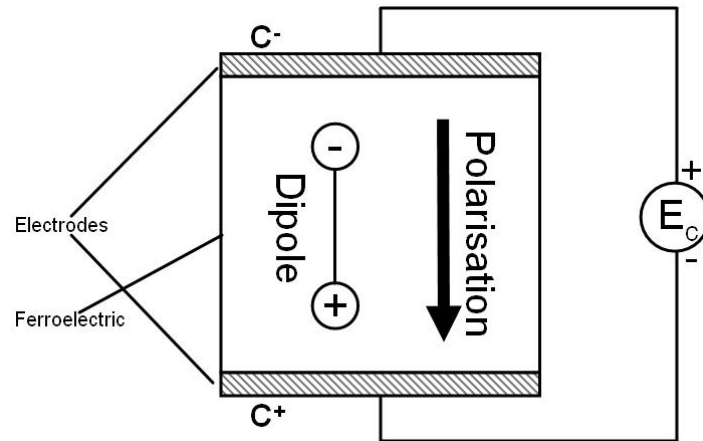


**Figure 2.4** Convention used for signifying polarisation direction and how it relates to the dipole moment and coercive field,  $E_c$ .  $C^-$  is the negative surface and  $C^+$  the positive. By switching  $E_c$  the dipole switches and the polarisation reverses.



## **2.2 PZT Film growth and structure**

The method used for the production of thin film ferroelectrics and the choice of substrate and electrode material impact greatly on film growth and electrical properties (Dunn and Whatmore, 2002). One method that has had much success in PZT processing is sol-gel (Mackenzie and Xu, 1997; Xu, 2001), a wet chemical route that uses colloidal solutions of precursors, the sol, that upon drying produce a gel which is then pyrolysed to form a solid film. The substrate is coated in the sol and pyrolysed to drive off the solvent, leaving an amorphous film. The film is annealed at high temperature which causes it to crystallise into the ferroelectric perovskite structure.

Work undertaken by Shaw *et al.* (2001) and Roy *et al.* (2000) has shown the dependence of film structure on base electrode material and substrate. They used indium tin oxide (ITO) on glass, some seeded with TiO<sub>2</sub> and the others unseeded. The unseeded films grew as a series of 15 µm rosettes Figure 2.5a, whereas the seeded samples gave smaller grains down to 160 nm, Figure 2.5b. The difference in grain size and distribution was due to defects on the electrode surface which controls the number of nucleation points; the seeded layer giving more nucleation possibilities than the unseeded. It was also observed that the films had random crystal orientation across the rosettes. This randomness occurred as the ITO layer was amorphous and thus did not direct the growth of the films. When electrodes of Pt on Si[111] substrates are used, the growth of very fine, 70-100 nm grain size, [111] orientated films is observed (Dunn and Whatmore, 2002), Figure 2.5c. The orientation of the PZT is due to the [111] orientation of the Pt, this is backed up by the fact that a MgO[100] substrate with Pt[100] as the electrode will give a PZT film of predominantly [100] orientation (Lairson *et al.*, 1992) when annealed.

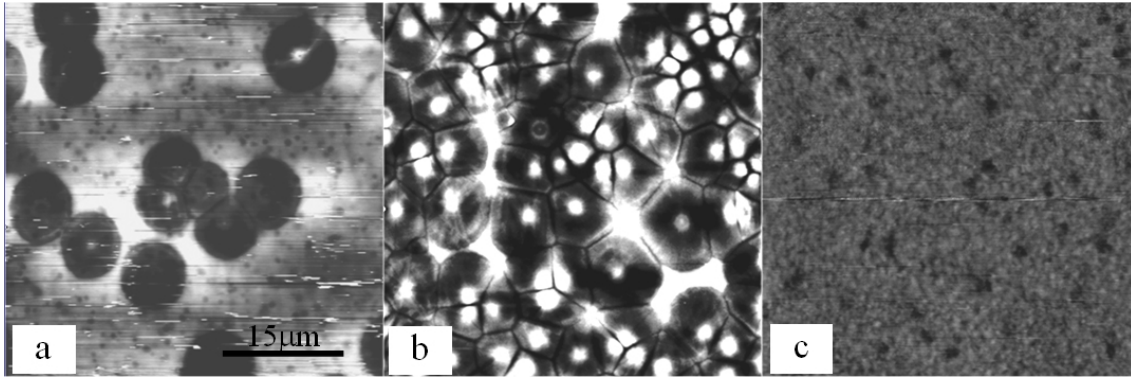


**Figure 2.5** AFM images of PZT(30/70) samples on different substrates, (a) PZT on unseeded ITO/glass has large, 15µm rosettes, (b) PZT on seeded ITO/glass gives a grain structure down to 160nm and (c) the PZT grown on Pt on Si[111] 70-100nm grains which are also columnar, (Jones, 2003).

In crystalline ferroelectrics such as single crystal  $\text{BaTiO}_3$  polar domains are made up of repeating unit cells where, on average, the central B cation is in the same position within adjacent cells (Cross and Hardtl, 1984), Figure 2.6. Ferroelectrics such as PZT are ceramics and are thus made up of crystallites/grains each with its own crystallographic axis orientation. The ferroelectric domains within the PZT film are, therefore, not all orientated in the same direction but are related to the orientation of each crystallite. The surface polarisation in each poled region is therefore the average of the polar vectors within the grains.

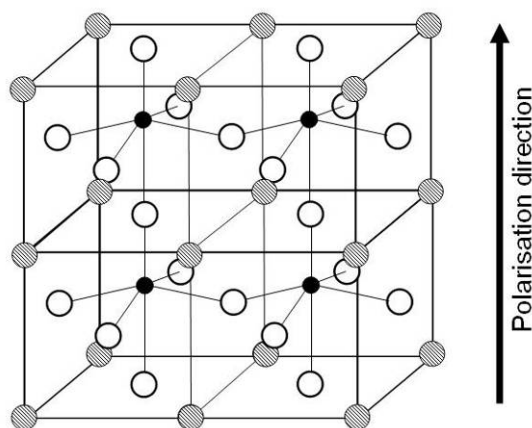


**Figure 2.6** Schematic of 4 unit cells from  $\text{ABO}_3$  ferroelectric, the centre black ion is in the same off-centre position for all cells thus the polarisation direction is as the arrow shows.

### 2.3 Orientation and bulk properties

The relationship between electrical properties and crystal orientation in PZT has been investigated by various groups, Du *et al.* (1997, 1998) for example found that the piezoelectric,  $d_{33}$ , and dielectric,  $\epsilon_{33}$ , constants were related to the orientation of the crystallite. For tetragonal PZT(48/52) the constants varied as in Figure 2.7, here the  $d_{33}$  was greatest in the [001] axis but reduced as the orientation changed, the opposite was true for the  $\epsilon_{33}$  where the [001] was lowest and increased as the angle changed.

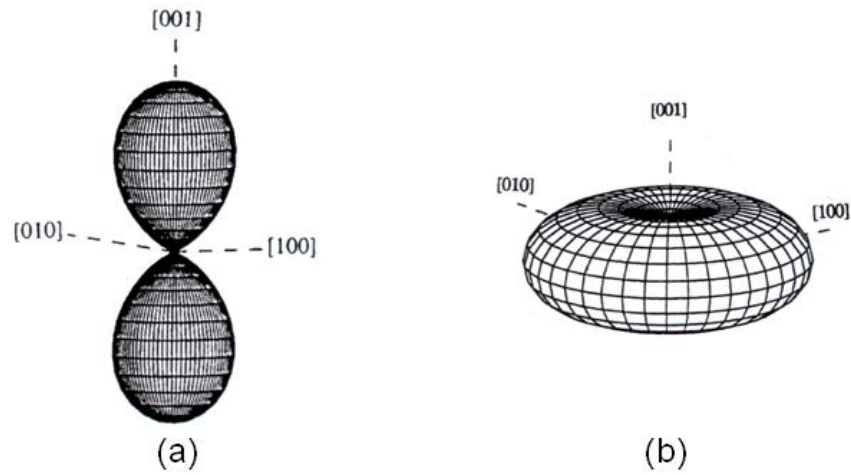


**Figure 2.7 Orientation dependence of (a)  $d_{33}$  and (b)  $\epsilon_{33}$ . The  $d_{33}$  for PZT is at its maximum in the [001] orientation and its drops off as the angle increases (Du *et al.*, 1998). The  $\epsilon_{33}$  is at its minimum in the [001] orientation (Du *et al.*, 1997).**

Kobayashi *et al.* also showed experimentally that for PZT(52/48) the  $P_r$  and  $E_c$  for [111] and [100] orientation differed. For a [111] orientated film they got a  $P_r$  of 21  $\mu\text{C}/\text{cm}^2$  and  $E_c$  of 50 kV/cm and for the [100] they got a  $P_r$  of 14  $\mu\text{C}/\text{cm}^2$  and an  $E_c$  of 29 kV/cm. It would be assumed that as the [100] orientation is perpendicular to the surface it would have the greater  $P_r$  than the [111], this is not true. This discrepancy is explained by Funakubo (2005) who states that film orientation consistency is very important. In [111] oriented films the orientation is highly consistent throughout, due to the epitaxial

growth of the PZT to the Pt[111] electrode, this gives a  $P_r$  of about 56% of the saturation polarisation. PZT[100] should give 100% of the saturation polarisation, but if other orientations are present it is possible that the  $P_r$  is only 38 to 50 % of the saturation polarisation. As an example the [001] orientation, which is in-plane with the film, will not contribute to the out-of-plane polarisation, therefore the ratio of [100] to other orientations will have an effect on the  $P_r$ . This has also been shown by Lee *et al.* (2002) whose work on  $\text{Bi}_{4-x}\text{La}_x\text{Ti}_3\text{O}_{12}$  films has shown the same dependency of  $P_r$  on orientation.

## **2.4 Semiconducting properties**

Various groups have shown that the  $\text{ABO}_3$  ferroelectrics can also be thought of as wide bandgap semiconductors. Pintilie *et al.* (2005) and Boerasu *et al.* (2003) have used current-voltage measurement techniques to study the semiconducting properties of PZT, and Lee *et al.* (2005) has used spectroscopic ellipsometry to analyse the band structure. It has been found that bulk PZT is a p-type material due to an abundance of acceptor-like impurities (Wouters *et al.*, 1995). The effect of these impurities is partly counteracted at the surface by the formation of oxygen vacancies, due to the high temperature annealing (Mihara *et al.*, 1992), that act as donor impurities (Chen *et al.*, 2004). These vacancies can be considered as missing negative charges and therefore represent a positive charge relative to the ideal crystal lattice (Smyth, 1991) this combination means that the free carrier concentration for PZT is very low (Pintilie and Pintilie, 2001; Raymond and Smyth, 1996).

Though they are wide bandgap semiconductors it is important that the polar nature of the ferroelectric is taken into account. Work by Kholkin *et al.* (2001) on the photoelectric effect on electrically biased PZT thin films found that the magnitude and

direction of photocurrent was related to polarisation. Figure 2.8, presents their results for the irradiation of the PZT surface through transparent electrodes with pulsed UV. With the film positively, poled current flow is positive, i.e. the electron migration is out of the film, when negatively poled the electron flow is into the film, the unpoled film has a slight migration into the film which is due to its inherent self polarisation.

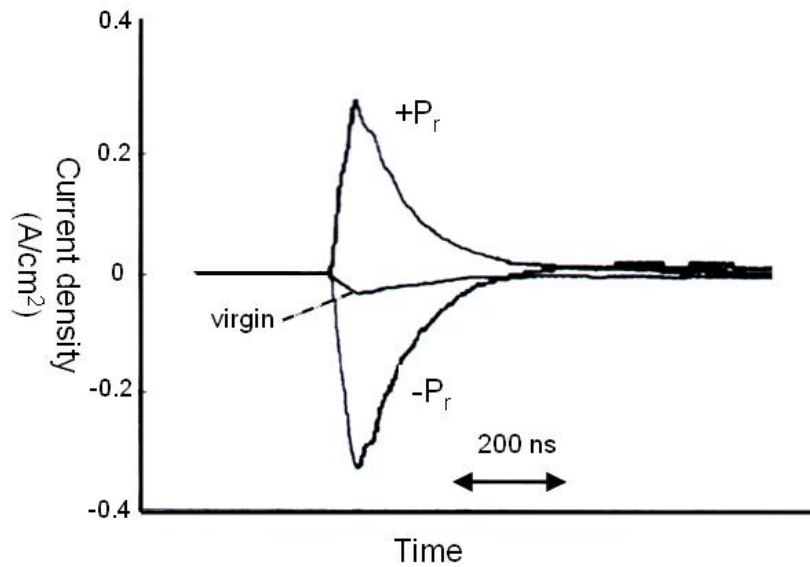


**Figure 2.8 Photocurrent versus time for PZT irradiated with pulsed UV through transparent electrodes. The direction of current flow is dependent on polarisation of film, shown are positive, negative and unpoled films as presented by Kholkin *et al.* (2001).**

From these observations Kholkin puts forward three possible mechanisms for the photocurrent controlling process; the pyroelectric effect, bulk photoelectric effects or effects due to ferroelectric polarisation. They rule out the pyroelectric effect by repeating the experiment with opaque Ni electrodes which strongly absorb UV in the range 300-500 nm, thus blocking light to the surface while allowing heat to flow. No current was measured upon illumination, which means that the observed current was not due to surface heating effects but to a direct interaction with photons. In order to find if the photocurrent direction was due to the bulk photoelectric effect or film polarisation,

they repeated the transparent electrode experiment but with dc bias applied in parallel to the film polarisation. They found that at low bias, 0-13 kV/cm, the photocurrent flow was opposite to the applied bias. Above this, but below  $E_c$ , the photocurrent switched direction and became directly related to the applied bias independent of polar direction, Figure 2.9. From this they concluded that at low bias the film polarisation affected the direction of the photocurrent, but at higher biases, above 13 kV/cm but below the  $E_c$ , the bulk photoelectric effect was dominant.

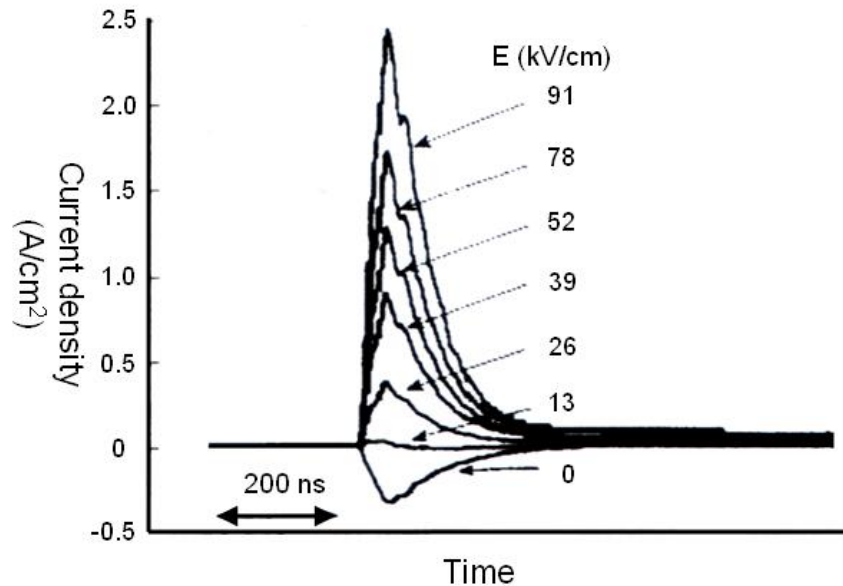


**Figure 2.9** Plot of photocurrent in PZT film during pulsed UV irradiation with applied dc bias to film in same direction as polarisation from Kholkin *et al.* (2001). At low bias , 0 -13 kV/cm, the photocurrent flow is in same direction as when no bias was applied. Above 13 kV/cm, but below  $E_c$ , the photocurrent direction switches and becomes independent of polar direction.

The polarisation dependence of the photocurrent was also observed by Inoue *et al.* (1989) when irradiating 100 $\mu$ m thick lead strontium zirconate titanate, PSZT, with a Xe lamp, Figure 2.10. In Kholkin's plot the current density has the same polarity as the surface being illuminated, in the plot by Inoue the voltage has the opposite polarity. This inversion is due to the convention that current flow is from a higher to a lower

potential where in reality electron flow is from negative to positive, therefore the charge is in fact of the same polarisation in both works.

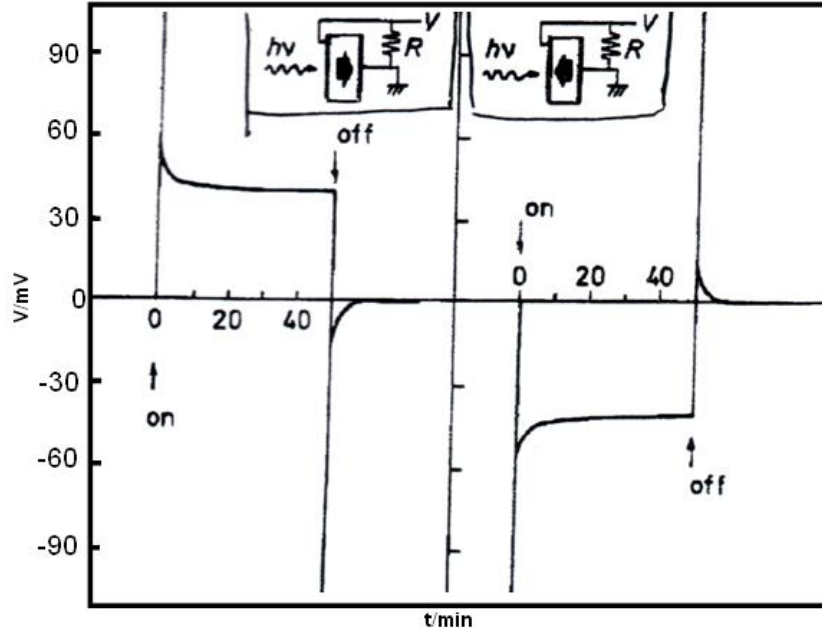


**Figure 2.10 Photovoltage against time for PZT under illumination obtained by Inoue *et al.* (1989). Voltage polarity is dependent on film polarisation.**

A major difference between Kholkin and Inoue is the presence of a peak when the PSZT is first illuminated which does not occur with Kholkin PZT. This peak rapidly drops to a steady state and when the illumination was removed a negative peak occurred. Inoue put these peaks down to the pyroelectric effect due to the surface temperature change upon initial illumination. It is interesting that Kholkin's group did not observe this effect. This could be due to the short duration, 7 ns, of the laser so that the generation of heat was dissipated by the top surface of the electrodes before the PZT experienced any heating effects.

The polarisation dependence of the measured charge can be explained by considering what happens during the absorbance of photons by the ferroelectric. As it is a semiconductor, PZT has an internal energy structure made up of a conduction and

valence band separated by a bandgap. It has been suggested by Silva *et al.* (2005) that the top of the valence band of PZT is made up of the oxygen 2p orbitals, and the bottom of the conduction band by titanium 3d orbitals. When a photon with energy above the bandgap strikes the film there is a chance that it will excite an electron from the valence band into the conduction band leaving a hole behind, these are termed an electron-hole pair (Markvart, 2000), Figure 2.11.

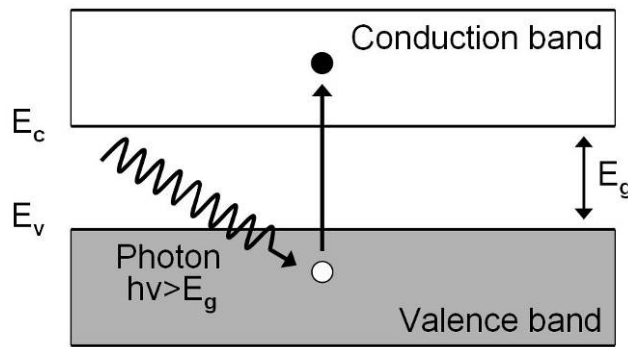


**Figure 2.11** Excitation of electron from valence band into conduction band by super bandgap photon.

Where the bulk of a semiconductor is broken by an interface the atoms that make up the crystal are not fully surrounded by neighbours and therefore have dangling bonds (Fraser, 1986). The electrons within these bonds have energy levels that are different to those within the bulk of the material, giving surface energy states that change the potential within the interface (Fraser, 1986). Also the ferroelectric has a large depolarisation field at the surface, which is energetically unfavourable (Yang *et al.*, 2004). In order for a stable energy state to exist two possible compensation processes can occur, one internal, in the form of a space charge region, SCR, (Bonnell and Kalinin, 2002; Kalinin and Bonnell, 2001; Zhu, 1994), and the other external where charged molecules are absorbed at the external surface forming an electrical double layer.



## **2.5 Energy Band Bending**

The flow of photocurrent opposite to polarisation observed by Kholkin and Inoue are due to the SCR. Kalinin and Bonnell (2001) state that the electrostatic properties of a ferroelectric surface can be represented by two charges. One is the spontaneous polarisation,  $P$ , and the other the surface screening charge which is of opposite polarity,  $-\rho$ . They show that there are four possible scenarios for the charge balance at the surface:

1. Completely unscreened,  $\rho = 0$
2. Partially screened,  $P > -\rho$
3. Completely screened,  $P = -\rho$
4. Over screened  $P < -\rho$

Scenario 1 is highly energetically unfavourable and scenario 4 would happen if an electrical bias were applied across the film such as during domain poling. When there is no field applied and the surface is in air then scenarios 2 and 3 are likely to occur the screening being mainly due to the SCR.

The polarity of the SCR is dependent on the orientation of the ferroelectric domain. In  $C^+$  domains the surface of the film has a positive charge and the region below forms a negative space-charge (Bonnell and Kalinin, 2001). This space-charge induces an internal E-field,  $V$ , which causes bending of the energy bands near the surface, Figure 2.12.

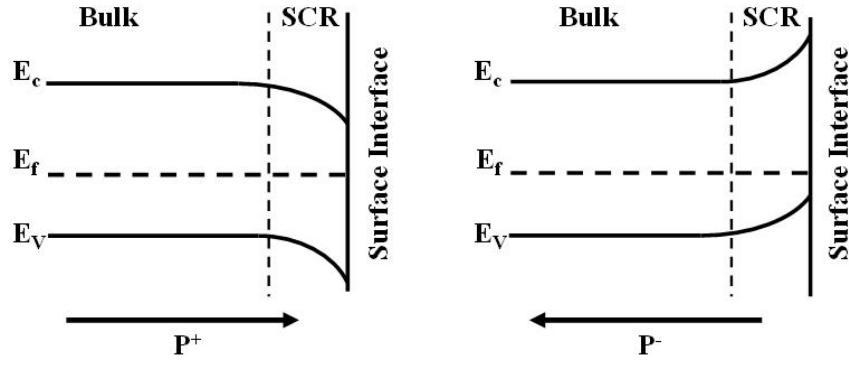


**Figure 2.12 Band bending at ferroelectric surface due to film polarisation and the formation of a space charge region, SCR.**

For a non-polar semiconductor, i.e. non ferroelectric, the potential,  $V$ , within the material can be calculated using the Poisson equation, Equation 2.1 (Blatter and Greuter, 1986b). The equation links  $V(x)$  relative to the distance from the interface and the charge density,  $\rho$ , which is a balance between the electrons,  $e^-$ , and holes,  $h^+$ , and the ionised acceptor,  $N_a^-$ , and donor atoms,  $N_d^+$ , at any particular point within the semiconductor, Equation 2.2.

$$\nabla^2 V = -\frac{\rho}{\epsilon_o \epsilon_r}$$

**Equation 2.1**

$$\rho = q(h^+ + N_d^- - e^- - N_a^+)$$

**Equation 2.2**

If Equation 2.1 is to be applied to ferroelectric semiconductors then account must be taken of the spontaneous polarisation. Maturra (2000) has modified the Poisson equation by including the polarisation, Equation 2.3, where  $\rho$  is the free charge on the surface and  $P$  the ferroelectric spontaneous polarisation.

$$\nabla^2 V = -\frac{1}{\epsilon_o}(\rho - \nabla P)$$

**Equation 2.3**

P is made up of  $P_r$  and a dielectric polarisation proportional to an applied field E as in Equation 2.4, where  $\chi$  is the electric susceptibility of the ferroelectric, i.e. the constant of proportionality for dielectric polarisation to applied field (Feynman *et al.*, 1964).

$$P = P_r + \epsilon_o \chi E$$

**Equation 2.4**

If the dielectric constant  $\epsilon_r = 1 + \chi$  is independent of  $P_r$  and no external field is applied then Equation 2.3 becomes Equation 2.5.

$$\nabla^2 V = -\frac{1}{\epsilon_o \epsilon_r} (\rho - \nabla P_r)$$

**Equation 2.5**

Equation 2.5 is basically the same as for a dielectric within a biased capacitor where there are free surface charges represented by  $\rho$ , and an electrical polarisation within due to the applied field (Feynman *et al.*, 1964), the difference here being that in a ferroelectric the polarisation  $P_r$  exists even without an applied field. Therefore the potential at any point within the ferroelectric is dependent on the  $P_r$  and the charge density. Where there is charge neutrality i.e.  $\rho = 0$ , as in the bulk, the potential is then due to variations in  $P_r$ , if there are no variations then the potential is zero. When  $\rho$  is not zero, such as at interfaces, the potential will differ dependent on position.

It should be noted that in the Maturra paper the results obtained in the plots are theoretical based on the above equations. In his illustrations of the effects of polarisation on the bending of the energy bands he has used  $\epsilon_r$  as low as 10 which in a real ferroelectric such as PZT is unrealistic. This has been done in order to show how the theoretical ferroelectric band bending responds compared to a ‘normal’ non-polar semiconductor as  $\epsilon_r$  changes. What is interesting about his results is that though the

‘normal’ semiconductor band bending is greatly affected by the dielectric constant the ferroelectric does not appear to be so dependent, as can be seen in Figure 2.13.

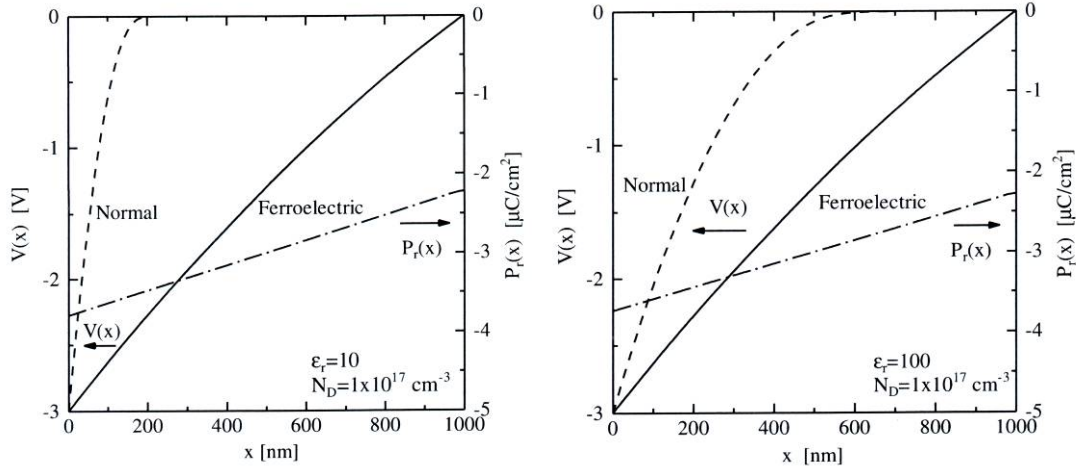


**Figure 2.13** Plots taken from Matsuura (2000) comparing band bending between a ‘normal’ non-polar semiconductor (dashed line) to that of a ferroelectric (solid line) as dielectric constant  $\epsilon_r$  is changed. Left  $\epsilon_r = 10$ , and Right  $\epsilon_r = 100$ .

The reason for this is that  $P_r$  in the SCR is not homogenous due to the field generated by the ionised atoms in this region; this is shown in Figure 2.13 as the dash-dot lines. If Equation 2.5 is reduced to its one dimensional form it becomes Equation 2.6.

$$\frac{d^2V(x)}{dx^2} = -\frac{1}{\epsilon_o\epsilon_r} \left( \rho(x) - \frac{dP_r(x)}{dx} \right)$$

**Equation 2.6**

In Equation 2.6 it is the  $\frac{dP_r(x)}{dx}$  element that has an overriding effect on the width of the

SCR, making the ferroelectric SCR wider than a non ferroelectric semiconductor SCR.

As stated previously the SCR polarity is dependent on the domain polarisation, which affects it just as an applied field would affect a non ferroelectric semiconductor. Figure 2.14 and Figure 2.15 (Fraser, 1986) show what happens to the SCR when a field is applied to a non ferroelectric p-type semiconductor as one side of a capacitor, though this can also be used to explain the SCR in the ferroelectric due to  $P_r$ . In Figure 2.14 an

E-field is applied perpendicular and out of the surface which causes the bands to bend up, the valence band moving closer to the Fermi level. The field causes holes to accumulate at the surface and thus a positive charge to form there. In a ferroelectric this effect is not caused by an external applied field but by an internal field generated by the  $C^-$  polarisation. It should also be noted that the diagrams show the band edges very close to the Fermi level at the surface, this is only for illustrative reasons they are in fact non-degenerate.

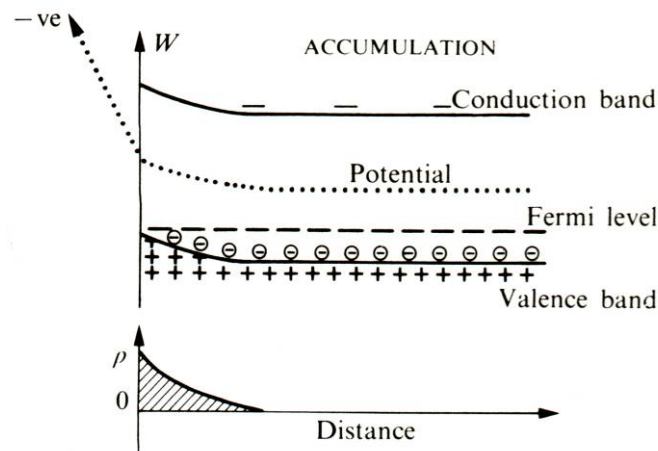


**Figure 2.14 Accumulation of holes at surface of semiconductor due to a field applied out of the surface. The bottom plot shows the charge density moving from the surface into the bulk, the surface charge being due to holes. (From Fraser (1986)).**

In Figure 2.15 the electric field is applied into the surface, the bands bend downwards and the conduction band moves closer to the Fermi level, in effect the surface has now become n-type even if the bulk is still p-type. Now electrons migrate to the surface and form an inversion layer, the same effect is happening in the ferroelectric  $C^+$  domain.

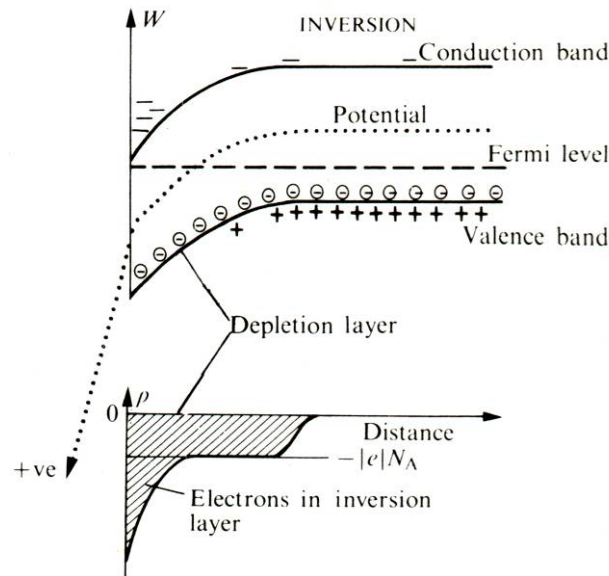


**Figure 2.15** Inversion layer at surface of semiconductor due to a field applied into the surface. The bottom plot shows the charge density moving from the surface into the bulk, the charge being due to migrating electrons. (From Fraser (1986)).

From this it is possible to explain Kholkin's photocurrent results; a photon striking the surface of the ferroelectric excites an electron into the conduction band. If it is excited in the surface SCR of a  $C^+$  domain it migrates to the surface due to the potential difference  $V$ , the hole that is left migrates into the bulk, thus a photocurrent forms. If a bias is applied opposite to the polarisation a point is reached where the band bending due to the  $P_r$  is overcome by the field and the electron hole migration will reverse, as seen after 13 kV/cm.

## 2.6 Grain boundaries

So far only surface interfaces have been considered, there are in fact other forms of interface and in polycrystalline semiconductors and ferroelectrics such as PZT (Bonnell and Kalinin, 2001; Kalinin and Bonnell, 2004; Hagenbeck *et al.*, 1996) grain boundaries play an important role. A grain boundary has been defined by Waser and Hagenbeck (2000) as the plane which separates crystallographically coherent regions. The core of

the boundary contains atoms with a lower coordination number, i.e. the number of surrounding atoms bonded to a central atom, and different bond lengths than the bulk of the grain. As a result electron/hole traps are common in these boundaries (Van de Krol and Tuller, 2002). These traps deplete the grains on either side of their free carriers creating multiple SCRs, forming a double Schottky barrier. This barrier has been modelled by Blatter and Greuter (1986a, 1986b), who show that grain boundaries are electrically active due to the mismatch of the crystallites and the trap states and localised impurity/dopant atoms that exist there.

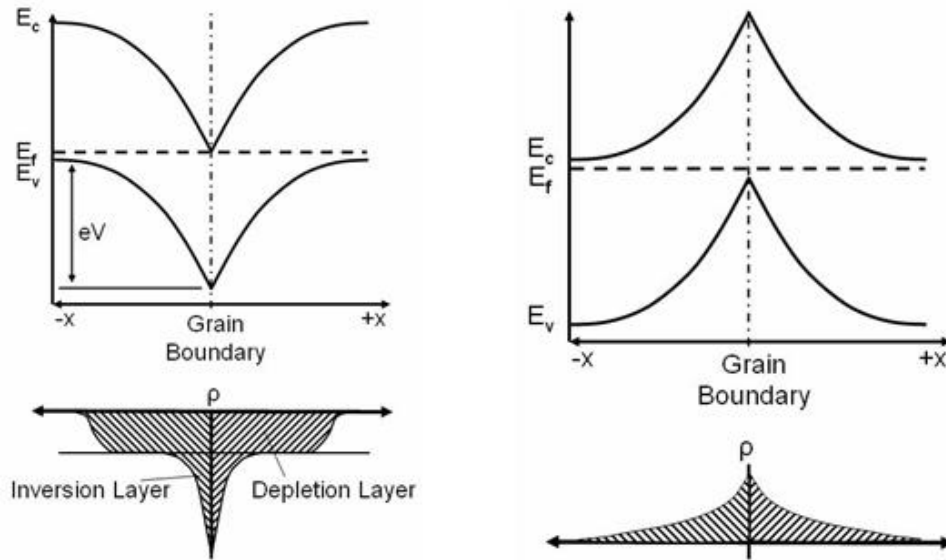


**Figure 2.16 Band bending at grain boundaries.** Top images shows band bending, and lower images shows the charge density,  $\rho$ , moving away from the grain boundary on both sides. The left image shows bending at positively charged grain boundaries, the charge is made up of electrons attracted to the boundary forming a depletion region and then an inversion region. The right hand side show the bending at a negatively charge boundary, the charge here made up of holes.

In Figure 2.16 the left hand side shows the downward band bending that occurs at a positively charged grain boundary. Mobile electrons within the grains near the boundary are attracted to it and form a SCR, consisting of a depletion zone and nearer the centre an inversion region. This is mirrored on both sides of the boundary and a potential

barrier is created to further carrier flow. For a negatively charged grain boundary, right image, the opposite occurs and the bands bend upwards creating a concentration of holes at the boundary. The polarity of the grain boundary core is independent of the ferroelectric polarity of the domains on either side.

The electrical activity at these boundaries has been demonstrated by Kim *et al.* (2007). They looked at the surface potential across a negatively poled PZT[111] sample using Kelvin force and piezoresponse microscopy and found that at grain boundaries the potential was lower than that of the bulk of the grain. They measured the surface potential as a function of time and found that the potential drop started at the boundary and spread into the bulk of the grain over time. They put this down to the surface screening charge migrating to the boundary, the process stopping when the boundary had reached charge neutrality. The SCR described by Blatter *et al.* would explain this process for a negatively charge grain boundary. Kiselev *et al.* (2007) have also shown with their work on La-doped PZT that the piezoelectric response also decreases as the boundary is approached. They explain that this was partially due to the compressive mechanical stress at the boundary and partially to an elemental compositional gradient across the grain.

The impact of grain boundary length was investigated by Lee and Joo (2002). As with Kiselev they showed that there was a decrease in the polar qualities of the ferroelectric as the grain boundary was approached. Lee also showed that the length of the grain boundary also played an important role in the polar properties of the material. They took polarisation and dielectric constant measurements at various locations on a PZT grain, Figure 2.17, A being taken within the grain, B at the boundary between two grains and



curve C at the intersection of 4 grains. Figure 2.18 shows the hysteresis curves and dielectric constant measurements obtained.

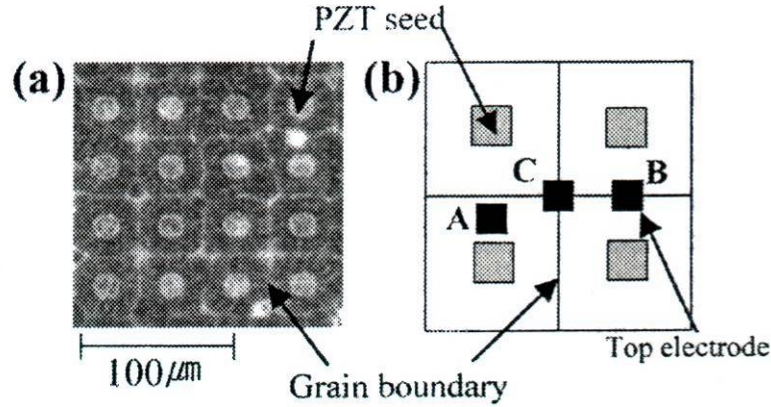


**Figure 2.17** Positions for electrodes used in Lee *et al.* work (Lee and Joo, 2002), A is within the grain, B is at the interface between two grains and C is at the intersection of 4 grains.

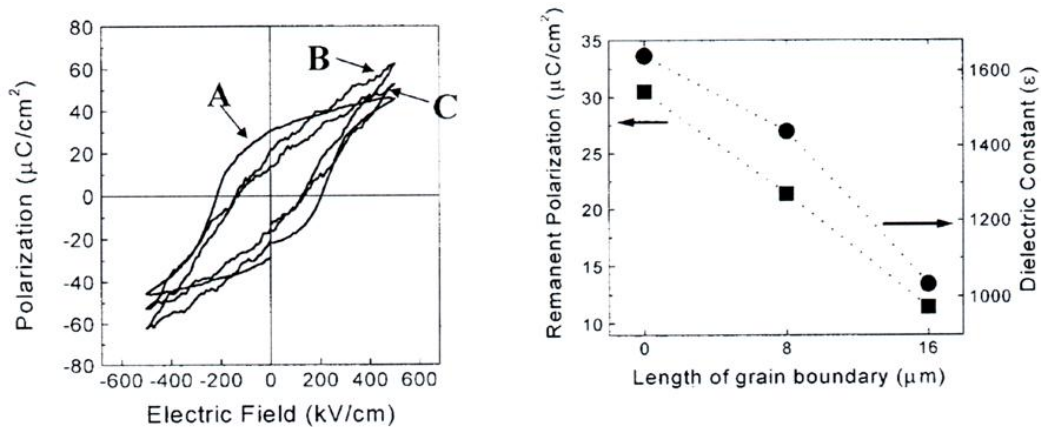


**Figure 2.18** hysteresis curves, left, and dielectric constant measurements, right, obtained by Lee and Joo, (2002) are presented. Curve A was the loop taken within the grain, curve B was taken at the boundary between two grains and curve C was taken at the intersection of 4 grains. In the right hand plot the circles represent to the dielectric constant and the squares  $P_r$ .

In Figure 2.18 the left hand plot shows that the  $P_r$  for position C was three times lower than that for A. It also shows that at location A the coercive field was higher than either B or C. Lee states that the dielectric constant and polarisation properties are mainly influenced by composition, crystallinity and defects within the material. They point out that the composition of the film and electrodes were the same for all measurement

points and therefore the degradation in polarisation was probably due to defects in the film. At point C there are more defects in the measurement area than at point B and therefore there is a greater degradation in the polarisation and dielectric constant. This again agrees with Blatter *et al.* where the effect on the electrical properties of the area surrounding the grain boundary is due to the crystal mismatch at the interface.

As there is a SCR at the grain boundary electrons and holes will react in the same way as that of the surface upon illumination (Card, 1977). Photogenerated charge carriers that form in the SCR will migrate either towards or away from the grain boundary dependent on its orientation. The carriers will migrate to the boundary until the balance between electrons, holes and traps are neutral and there is no more charge distribution.

## **2.7 Electrical Double Layer**

As already stated there are two energy compensation processes occurring at the surface interface of a semiconductor, one internal the other external. The internal process is the bending of the energy bands and the formation of the SCR as discussed in section 2.5. The external process takes the form of an electrical double layer (Yang *et al.*, 2004; Many *et al.*, 1965) where charged species in solution form a complex layer on the interface. Figure 2.19 illustrates the double layer for a  $C^-$  ferroelectric domain surface. Charged species of similar polarity to the surface are repelled while dissimilar species are attracted (Butt *et al.*, 2006). The attracted species form a layer over the surface of the charged region known as the inner Helmholtz plane, IHP, next to this is a second layer made up of oppositely charged species known as the outer Helmholtz plane, OHP, together these are known as the Stern layer. This is then followed by a diffusion layer where the species concentration reduces with distance. The polarity of the planes is inverted for a  $C^+$  domain.

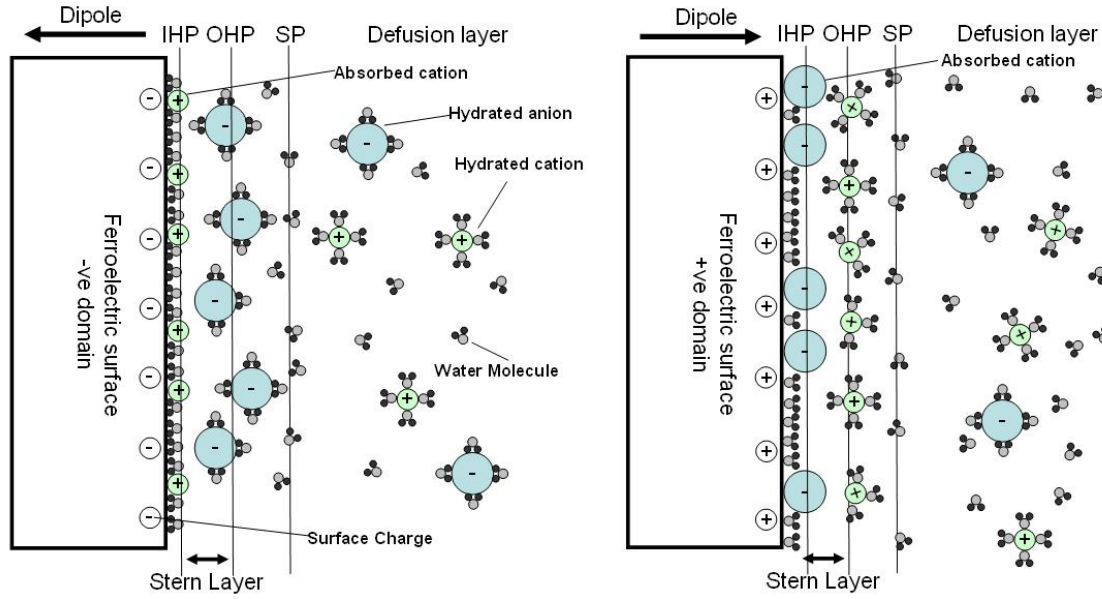


**Figure 2.19** Electrical double layer formed at the surface of a ferroelectric, left is  $C^-$  domain and right is  $C^+$  domain. The inner Helmholtz plane (IHP) is formed of species with a counter charge to the surface, followed by the outer Helmholtz plane (OHP) consisting of species of opposite charge to the IHP, these form the Stern layer. Following the stern layer is a diffusion region where the charged species concentrations reduce with distance form the surface, the region between the diffusion and OHP is a slip plane (SP).

The potential,  $V(x)$ , is a function of the distance,  $x$ , from the ferroelectric surface and is dependent on the charge density,  $\rho$ , at the surface and the molarity of the solution. For the diffuse layer,  $V(x)$  can be found using Equation 2.7 (Mulvaney, 2001).  $C_0$  is the bulk concentration of the ions in solution,  $k_B$  is Boltzmann's constant and  $T$  the absolute temperature.

$$V(x) = V_{surf} e^{-kx} \quad \text{where} \quad k = \sqrt{\frac{2c_0 e^2}{\epsilon \epsilon_0 k_B T}}$$

**Equation 2.7**

This means that the potential decreases exponentially from the ferroelectric surface into solution. The actual decay length is known as the Debye length and is equal to  $k^{-1}$  and dependent of the solution ionic concentration. As the ion concentration at the surface can be very large due to the ions with opposite charge being attached to it the potential

drops rapidly in the Stern layer, then it reduces exponentially to zero in the diffusion layer, as illustrated in Figure 2.20.

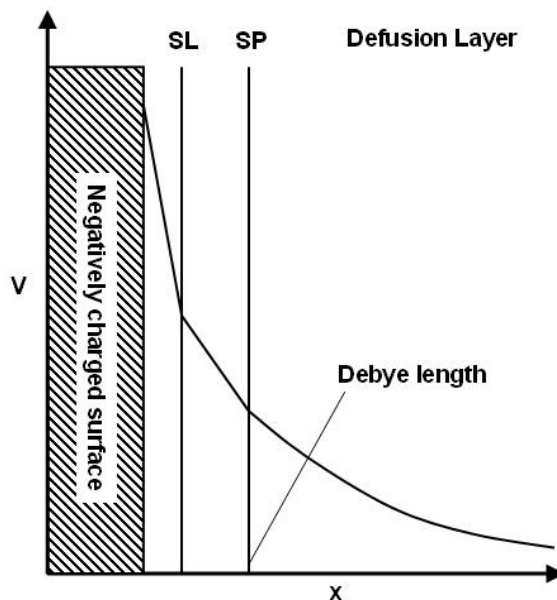


Figure 2.20 Illustrative plot of electrical double layer formed at a negatively charged surface. SL is the end of the stern layer made up of the inner and outer Helmholtz planes. SP is the slip plane between fixed ions at the surface and the diffusion layer. It can be seen that the potential,  $V$ , drops as the distance,  $x$ , increases. It should also be noted that the drop is not linear but has different extinction characteristics depending on which layer it is in.

## 2.8 Photoelectrochemistry at ferroelectric surfaces

Much use has been made of semiconducting materials through the years due to their photocatalytic properties and their ability to reduce and oxidise metals (Tryk *et al.*, 2000; Grätzel, 2001; Abrams and Wilcoxon, 2005). In the late 1920's it was observed that 'titanium white',  $\text{TiO}_2$ , a popular pigment of the time, had an adverse bleaching effect in paints when illuminated (Keidel, 1929). Much research was undertaken in the 1930's into studying this effect, for example Goodeve and Kitchener (1938) in 1938 showed that the bleaching was dependent on the wavelength of light irradiating the surface and found that UV wavelengths gave the greatest bleaching, though the

mechanism was not yet understood. In 1955 Brattain *et al.*, Brattain perhaps better known as co-developer of the transistor (Bardeen 1994), established the mechanism for the photovoltaic effect in semiconductors showing how a SCR affected the electrons and holes during illumination (Garrett and Brattain, 1955) and as Mills and Le Hunte (1997) states ‘the modern era of photoelectrochemistry was born’.

Today semiconductors such as  $\text{TiO}_2$  have been widely used in both bulk and nanoparticle form to break down metallic and organic contaminants in water and soil (Beydoun *et al.*, 1999; Hotsenpiller *et al.*, 1998). Tanaka *et al.* (1986) showed that Pt coated  $\text{TiO}_2$  nanoparticles irradiated with light in solutions containing  $\text{Pb}^{2+}$ ,  $\text{Mn}^{2+}$ ,  $\text{Ti}^+$ , or  $\text{Co}^{2+}$  ions reduced the ionic concentrations of these metals while the  $\text{TiO}_2$  particles changed colour. They found that some of the metals reduced onto the particle surface while others, such as Pb oxidised. The rate of ionic depletion was found to be dependent on where the oxidation potential of these salts is with respect to the bandgap of the semiconductor.

Bulk  $\text{TiO}_2$  was used by Lowekamp *et al.* (1998) to reduce  $\text{Ag}^+$  to  $\text{Ag}^0$  and they found that although the reactivity of the surface was partly dependent on the orientation of the crystal the surface structure also had an impact. From their work they concluded that there were two potential causes for the anisotropic reactivity of the sample, one was the structure and chemistry of the uppermost atomic layers and the other was due to the absorption of light, charge transport and the subsurface charge layer in the bulk. They believed that the surface effects were of greater impact than the bulk. To prove this they showed that even on unreactive bulk orientations Ag deposits could still be seen at out-of-plane faults such as grain boundaries and polish scratches. If the reactivity was purely due to the bulk photo effect then local topographic variations would not affect

the absorption of photons or charge transport to the surface. This effect can therefore be explained by the processes described in 2.6.

TiO<sub>2</sub> though a good photocatalyst does not have the spatial selectivity of reduction and oxidation seen in ferroelectric materials. In 2001 Giocondi and Rohrer (2001a, 2001b, 2001c) undertook photoreduction experiments using BaTiO<sub>3</sub>. They found that Ag salts deposited a metallic layer on C<sup>+</sup> domains and salts containing cations such as Pb left oxide deposits on the C<sup>-</sup> when irradiated with UV. This proved that it was possible to spatially control the reduction/oxidation process using ferroelectric surfaces. They showed that like a semiconductor, photons incident to the ferroelectric surface generated electron/hole pairs that were separated by the field formed by the surface SCR, as shown for the Kholkin work, section 2.4. The electrons excited to the C<sup>+</sup> surface were accepted by the Ag<sup>+</sup> cations in solution which then reduced to metallic Ag<sup>0</sup> and deposited there. They also showed that holes were excited to the surface, as happens in C<sup>-</sup> domains where the Pb<sup>2+</sup> ion oxidised.

This work was taken further by Bonnell and Kalinin (Bonnell and Kalinin, 2002; Kalinin and Bonnell, 2001) who suggested that the preferentially controlled deposition of metals on ferroelectric domains could be used as a method of producing metallic nanoparticles of defined morphology. Using PZT surfaces poled using AFM they successfully deposited metal in predefined patterns, Figure 2.21.

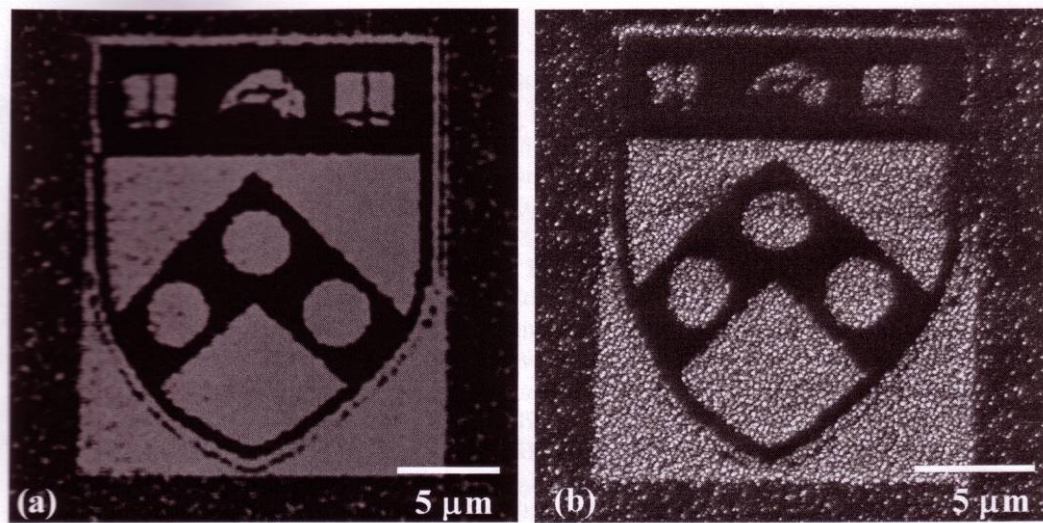


**Figure 2.21** Image (a) PFM image of university of Pennsylvania crest on PZT, (b) Ag reduced onto  $C^+$  domain surface by Bonnell and Kalinin (2002). The metal has grown as an area of independent nanoparticles.

Bonnell points out that this method of directed growth is different to that of local electrostatic attraction where nanostructures are grown from surfaces patterned with a charge. In this process the surface charge is held by the polar domain in the bulk and therefore fixed in its position. Further work showed that it was possible to use other metals in the growth process such as Au and Pd (Kalinin *et al.*, 2002), Rh, Pt (Kalinin *et al.*, 2004) and Co, Ni, and Fe (Lei *et al.*, 2005).

As can be seen in Figure 2.21, the metal grows as clusters across the surface of the  $C^+$  domains. Hanson *et al.* (2006) have discovered that when single crystal lithium niobate,  $\text{LiNbO}_3$ , was used instead of PZT the metal clusters form not across the surface but at the boundaries between domains, Figure 2.22. They explain this difference as being due to the relative surface charge carrier levels for the two materials. When PZT films are made they are annealed at high temperature and a high concentration of oxygen vacancies can occur at the surface, estimated at around  $10^{14} \text{ cm}^{-2}$  (Scott, 2000), for  $\text{LiNbO}_3$  they estimate that this is in the order of  $10^{12} \text{ cm}^{-2}$ . The high surface charge



density at the PZT surface causes greater band bending and therefore is a significant contributor to the internal surface screening charge. They state that the relatively low number of carriers for the  $\text{LiNbO}_3$  means that the major contributor to the compensation process is external screening due to absorption of charged particles rather than band bending. This means that the internal SCR is relatively weak and the electron/hole generation is inefficient when compared to the recombination processes that take place. By using the method described by Kalinin and Bonnell (2001) to measure local potential on ferroelectric surfaces using an AFM Hanson found that the surface potential peaked in the vicinity of  $180^\circ$  boundaries, Figure 2.23. Therefore when photoexcited electron/holes are generated near this region they separate and metal deposits there.

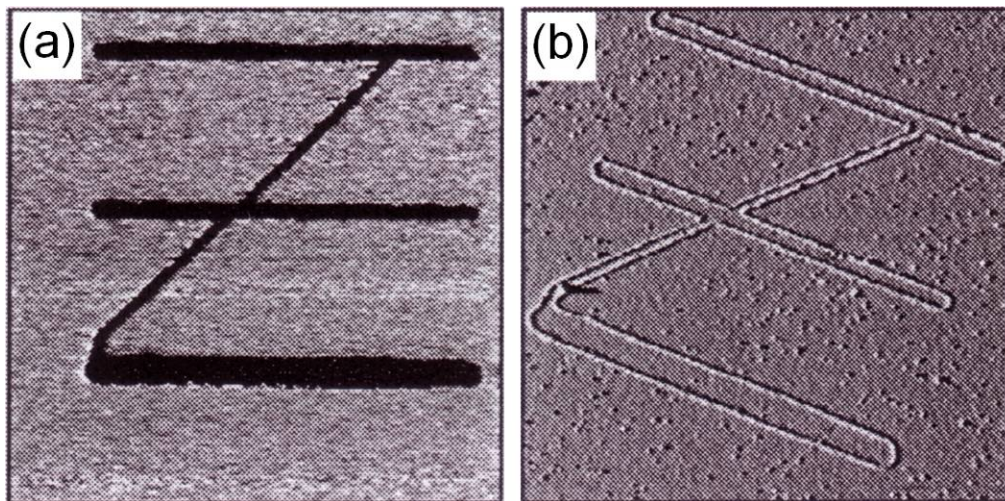


**Figure 2.22 (a) PFM image of Z shaped  $C^+$  domains on Single crystal  $\text{LiNbO}_3$ , (b) Ag wires deposited at domain boundaries (Hanson *et al.*, 2006).**



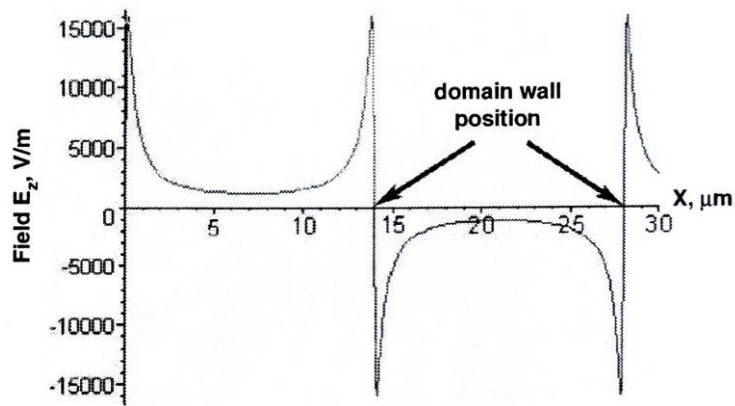


**Figure 2.23** Calculated potential at surface of lithium niobate (Hanson *et al.*, 2006), the potential peaks at the domain boundaries and reduces as the centre of the domains is approached.

In the work by Kalinin *et al.* the energy required to cause Ag to deposit onto the surface of their PZT samples was 4.5 eV (Kalinin *et al.*, 2004) or higher. This is 1.1 eV higher than the bandgap of 3.4 eV put forward by Scott (1999) and Pandey *et al.* (2005). This discrepancy between the energy levels maybe explained by studying the density of states (DoS) of the valence band. Silva *et al.* (2005) put forward a theoretical model that shows the estimated DoS for PZT, Figure 2.24. It can be seen in the plot that there is a low concentration of states just below the bandgap. However, further into the valence band the number of available states and associated electrons increases. The quantity of generated charge carriers is controlled by a number of factors. Two of which are the number of electrons excited in the conduction band by photons and the rate of recombination of electrons and holes (Grätzel, 2001). If the rate of carrier generation is lower than that of recombination then the carriers are very likely to cancel each other out before any Ag deposition can occur on the surface of the PZT. If on the other hand the photons have enough energy they can excite electrons deeper in the valence band thus making more electrons available for surface reduction. It should be noted that in Figure 2.24 that the bandgap is given as 3.03 eV as opposed to the 3.4 eV put forward

by Scott *et al.* This variation can be explained by the fact different PZT samples were used by each group, the variation in composition, Zr and Ti ratios and other variables in film manufacture will affect the bandgap width.

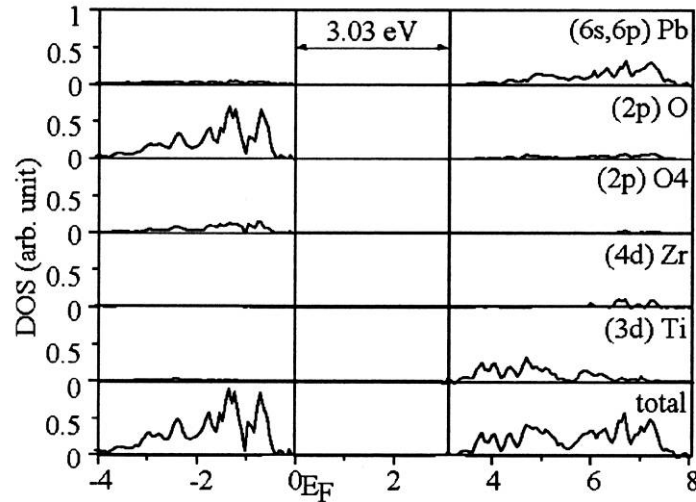


**Figure 2.24** Plot of the Density of states for PZT as modelled by Silva *et al.* (2005). Each row represents the states provided by each of the elements within the PZT film. The bottom row shows the total DOS from all elements, the left hand side of the plot is the valence band. It can be seen that the DoS in the valence band is greater at points deeper into the band than near the edge of the bandgap. A photon of higher energy than the bandgap is required to generate electron hole pairs in any sufficient quantity.

## 2.9 Objectives

Though there has been much work undertaken into the photochemical processes that occur at ferroelectrics surfaces it is clear from the literature that there are still many areas that need study. Film structure for example has been investigated with respect to its effects on ferroelectric properties but the reactivity of interfaces, particularly grain boundaries, in a photochemical reaction has had only limited enquiry. The underlying internal processes of charge carrier excitation and migration at these points must be understood in order to fully appreciate metal growth mechanisms at the ferroelectric surface.

Exterior to the ferroelectric the effects of ionic charge and reduction potential relative to band structure also need to be considered. It has been shown in the literature that these parameters are highly relevant to non-ferroelectric semiconductor photochemistry (Pleskov,1986). The reduction potential position in particular is of importance as it dictates whether metal reduction occurs on the surface or the semiconductor decomposes; the same knowledge is required for ferroelectrics. The existence of a stern layer has also not yet been incorporated into the model of metal nucleation and growth at the ferroelectric surface. The work presented here addresses these areas.

## 3 Methodology

### 3.1 Samples Used

The PZT samples were manufactured using the sol-gel fabrication method, section 3.2.2, and were of three substrate types:

- Glass/ITO, from this point on known as GI1 (Roy *et al.*, 2000), coated with PZT (30,70) at 210 nm thickness, which formed rosette-like perovskite structures surrounded by a pyrochlore phase, Figure 3.1.
- Si[111]/SiO<sub>2</sub>/Ti/Pt (Dunn and Whatmore, 2002), from this point on known as PZT[111], coated in PZT (30,70) at 70 nm thickness and forming grains of around 70-100 nm with a random domain orientation, Figure 3.2. The crystal orientation for this film was [111].
- MgO[100]/Pt (Tuttle *et al.*, 1993), from this point on known as PZT[100], coated with PZT (30,70) at 70 nm thickness, which formed grains similar to the PZT[111] of around 70-100 nm with a random domain orientation, Figure 3.2. The crystal orientation for this film was [100].

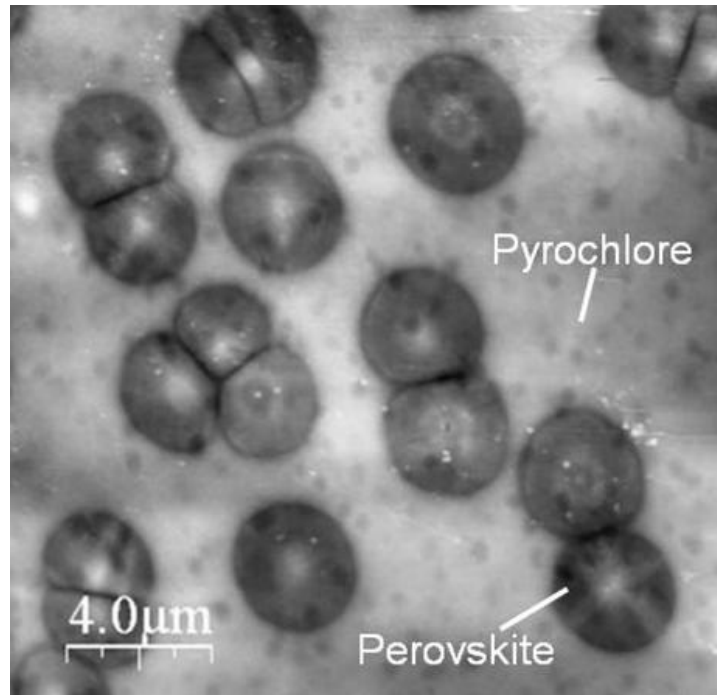


**Figure 3.1 AFM image of GI1 sample consisting of individual perovskite rosettes (Dark circles) surrounded by pyrochlore phase.**

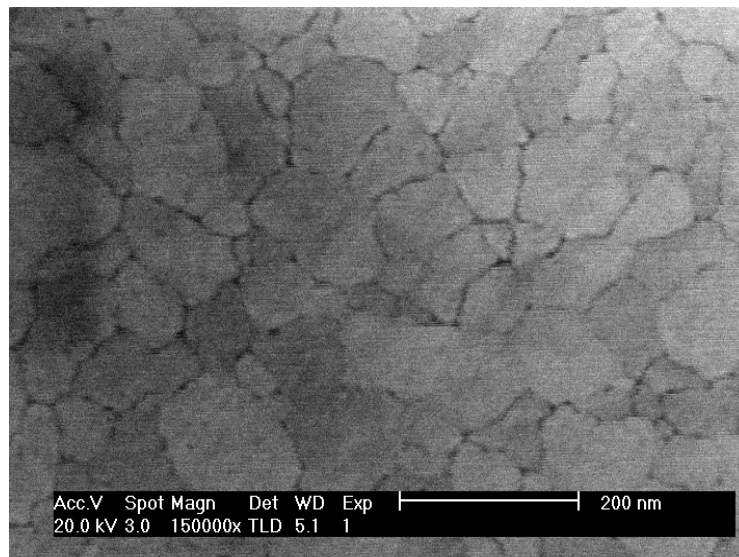


**Figure 3.2 SEM of grain structure of 70nm thick PZT on PZT[111], grain size varies from 100 nm down. The 70 nm thick PZT[100] sample was of a similar structure.**

## **3.2 PZT Film Preparation**

### **3.2.1 Pt Deposition**

100 nm thick Pt base electrodes were sputtered onto the Si and MgO substrates using two methods dependent on the substrate type. The Si substrate was sputtered using a Nordico sputterer at room temperature giving a Pt[111] base electrode with a Ti adhesion layer. The MgO[100] substrates were sputtered using the Balzer sputterer, the substrate being heated to 590 °C, and the plasma energy being set at 300 watts giving a Pt[100] film, with no requirement for an adhesion layer.

### **3.2.2 PZT Deposition**

Ready prepared PZT 30/70 sols (TDK) (Huang *et al.*, 1998) were used to fabricate the films. The platinised substrates were placed into a Cookson G3-8 spin coater and the PZT sol dripped onto its surface through a Whatman 0.2 µm filter using a syringe. The variables for the spin coater are tabulated in Table 3.1. Once spinning was complete the sample was transferred to a hotplate and pyrolysed at 220 °C for 2 minutes before being annealed at 560 °C for 5 minutes.

**Table 3.1 Settings for Cookson G3-8 spin coater used to deposit PZT films.**

Spin Speed	3000 RPM
Ramp up time	0 sec
Ramp down time	0 sec
Spin time	30 sec

The prepared samples were examined using a Siemens D5005 X-ray Diffractometer (XRD) to characterise the film structure.

## **3.3 Reference marks on samples**

In order to locate regions on some of the PZT samples the pattern presented in Figure 3.3 was etched into the surface using an FEI Strata 200xP Focused Ion Beam milling

machine. A line was scribed across the sample using a diamond scribe as a large visual marker and the reference pattern was milled below it. The settings used are shown in Table 3.2.

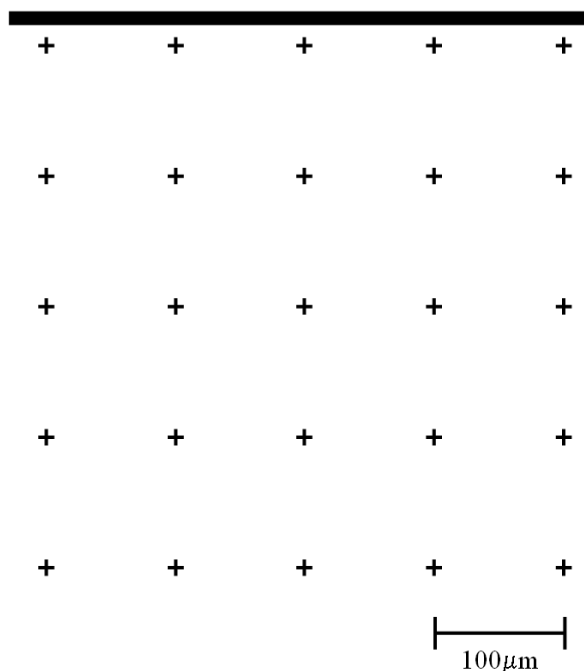


**Figure 3.3. Reference pattern FIB milled into surface of samples.**

**Table 3.2 Settings used for FIB of reference marks onto samples.**

Beam Current	2.7 nA
Beam Energy	30 keV
Dwell Time	0.5 ms
Period per scan	7.5 mins

### **3.4 Metal Salts and solutions**

#### **3.4.1 Metal salts**

Various metal salts were used as 0.01 M solutions, the quantities used are tabulated in Table 3.3, these were dissolved in 10 ml deionised water.

**Table 3.3 Metal salts used in experimentation**

Name	Formula	Quantity $\times 10^{-3}$ ( $\pm 3 \times 10^{-3}$ g)
Silver(I) nitrate	AgNO <sub>3</sub> (Sigma-Aldrich, 99.99%)	17
Tin(II) chloride	SnCl <sub>2</sub> (Aldrich, 98.00%)	19
Iron(II) chloride tetrahydrate	FeCl <sub>2</sub> ·4H <sub>2</sub> O (Across, 99.00%)	20
Chromium(III) nitrate nonahydrate	Cr(NO <sub>3</sub> ) <sub>3</sub> ·9H <sub>2</sub> O (Aldrich, 99.99%)	40
Manganese(II) nitrate hydrate	Mn(NO <sub>3</sub> ) <sub>2</sub> H <sub>2</sub> O (Aldrich, 98.00%)	20
Aluminium(III) chloride	AlCl <sub>3</sub> (Sigma-Aldrich, 99.00%)	14
Zinc(II) chloride	ZnCl <sub>2</sub> (Sigma-Aldrich, 98.00%)	14
Zinc(II) nitrate	Zn(NO <sub>3</sub> ) <sub>2</sub> (Sigma-Aldrich, 98.00%)	30
Copper(II) chloride	CuCl <sub>2</sub> (Aldrich, 99.99%)	13

### 3.4.2 Tollens Reagent

The reagent precursors were prepared as follows; a 0.25 M AgNO<sub>3</sub> solution was made by dissolving  $0.339 \pm 3 \times 10^{-3}$  grams of AgNO<sub>3</sub> in  $8 \times 10^{-3} \pm 0.2 \times 10^{-3}$  litres of H<sub>2</sub>O. A second solution of 3 M NaOH was produced by dissolving  $0.240 \pm 3 \times 10^{-3}$  grams of NaOH (Aldrich 99.99%) into  $2 \times 10^{-3}$  litres of H<sub>2</sub>O. Finally a 6M solution of NH<sub>4</sub>OH was prepared by mixing  $2.1 \pm 5 \times 10^{-3}$  grams of NH<sub>4</sub>OH (Aldrich 99.99%) into  $10 \times 10^{-3} \pm 0.2 \times 10^{-3}$  litres of H<sub>2</sub>O.

One drop of the NaOH solution was added to the AgNO<sub>3</sub> solution and a brown precipitate formed. The NH<sub>4</sub>OH solution was added dropwise to the precipitated solution until it turned clear. The beaker containing the solution was agitated during the addition of NH<sub>4</sub>OH. The finished Tollens reagent was used within 1 hour of production.

### 3.5 AFM poling

The poling of the samples was done using a DI Dimension 3000 Atomic Force Microscope (AFM). A modified cantilever holder, Figure 3.5, was used in order to avoid damaging the AFM when poling voltages over  $\pm 12$  V were used. The setup is shown in Figure 3.4. The PZT[111] and PZT[100] samples were poled using 14 V which equates to  $200 \text{ kVmm}^{-1}$  across the 70 nm film. A series of squares were poled



into the PZT as in Figure 3.6. To create  $C^+$  domains the sample base electrode was connected to the positive terminal of the PSU and the AFM tip to the negative, for  $C^-$  poling the terminals were reversed. The GI1 samples were left unpoled.

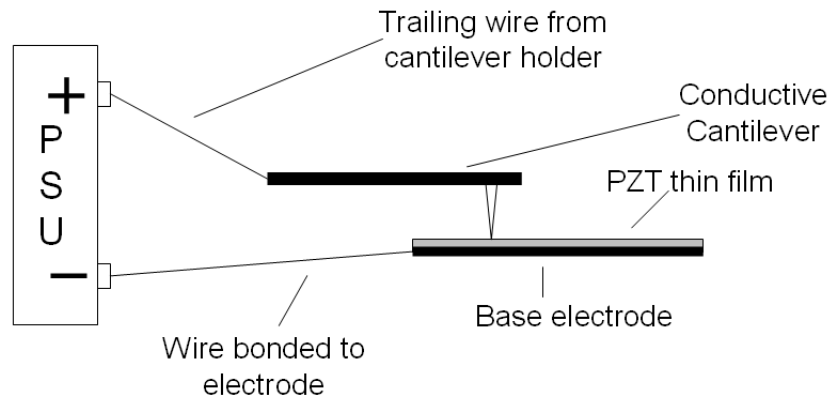


**Figure 3.4.** AFM configuration for poling PZT thin films. This setup will pole a  $C^-$  domain, for a  $C^+$  domain the wires to the PSU are switched.

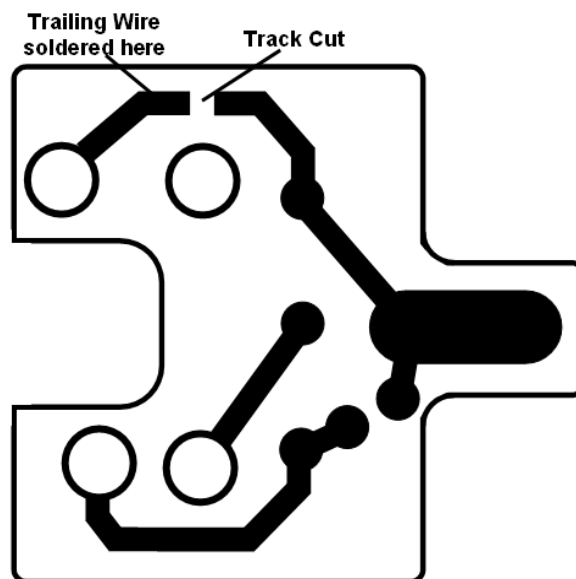


**Figure 3.5.** Schematic of modified cantilever holder viewed from the top. The track at the top of the holder is cut and a trailing wire soldered to the track connected to the pin on the top left.

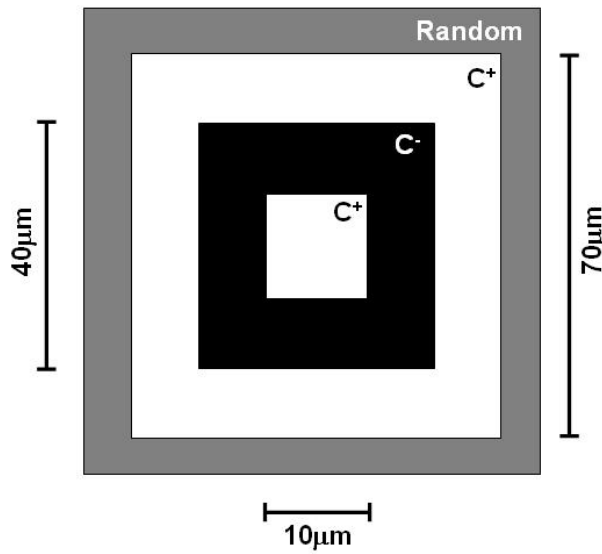


Figure 3.6. Poled pattern on PZT surface showing  $C^+$  and  $C^-$  domains, outside of the poled area the domains are random as grown, shown by the gray surround.

### 3.6 PFM Characterisation

The initial polar domain characterisation of the samples was carried out using the DI Dimension 3000 AFM in piezoresponse force (PFM) mode (Jones, 2003). The AFM was connected as Figure 3.7. The sample being held onto the AFM platen by a magnet and its base electrode connected to the ground of the signal generator coaxial cable. The signal generator output was set to 18 kHz at 2.5  $V_{pk-pk}$ . In order to avoid running the tip bias signals though the AFM a cantilever holder was modified to accept a direct connection to the tip, Figure 3.5.

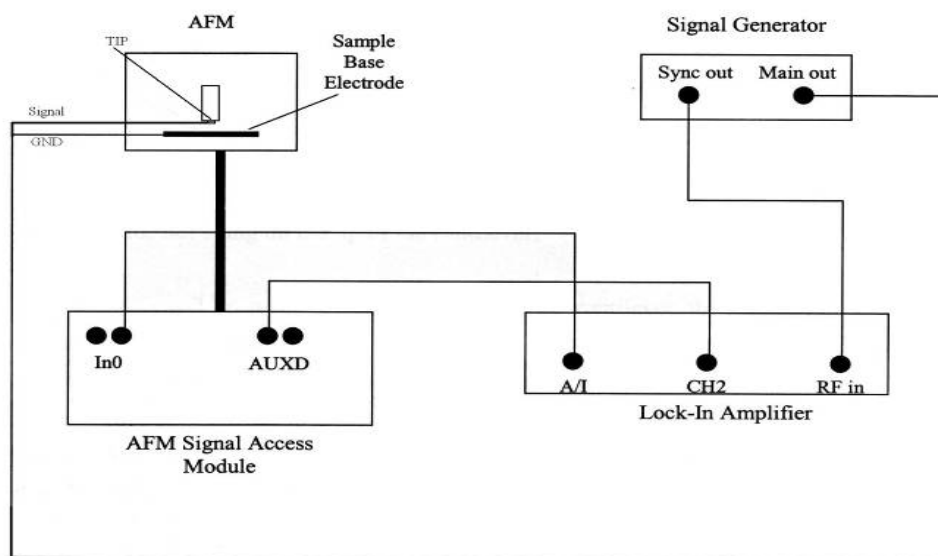


Figure 3.7. Set up of Atomic force microscope in piezoresponse mode, for polar domain characterisation.

### 3.7 Spectral characterisation

#### 3.7.1 Transmittance spectra of salts

Each 0.01M salt solution was made using the process described in 3.4.1, and poured into a quartz cuvette, which was placed into a Perkin-Elmer UV/Vis Lambda 7 Spectrophotometer. A wavelength sweep was undertaken from 3 - 5.5 eV (400 nm to 225 nm); the output from the scans was then analysed for UV absorption by the solution.

#### 3.7.2 Transmittance spectra of Ag films

Tollens Reagent was produced as described in 3.4.2 and 2 ml placed onto a quartz slide, to this a drop ( $\approx 25 \mu\text{l}$ ) of 2 M glucose solution was added and left for 30 minutes allowing a silver film to form. The slide was then rinsed with deionised water and blow dried with nitrogen. The slide was placed into the spectrophotometer and a sweep from 2.5 to 6 eV (496 to 207 nm) carried out.

## **3.8 UV Exposure Unit**

### **3.8.1 Enclosure and cooling**

A UV exposure unit was built to irradiate the experimental samples. The unit consisted of a Honle UVASPOT<sup>®</sup> UV lamp unit mounted on a custom built chamber, Figure 3.8. The front sliding door and the shutter were arranged such that the two could not be opened at the same time. This interlock avoided the possibility of accidental exposure of the operator to high energy UV radiation. Within the chamber a TEC Peltier device mounted on a PC microprocessor heatsink and fan, was fitted to control sample temperature. Two electric fans were mounted at the back of the unit to circulate air inside the chamber.



**Figure 3.8 UV irradiation chamber.**

### **3.8.2 UV lamps**

Two lamps were used for in this work both manufactured by Honle, the first contained Hg gas, H-lamp, the output of which went to 200 nm, Figure 3.9. The second lamp was an Fe doped Hg bulb, F-lamp, the spectrum of which can be seen in Figure 3.10. The intensity incident at the sample surfaces during exposure was measured as an average of 21 mW.

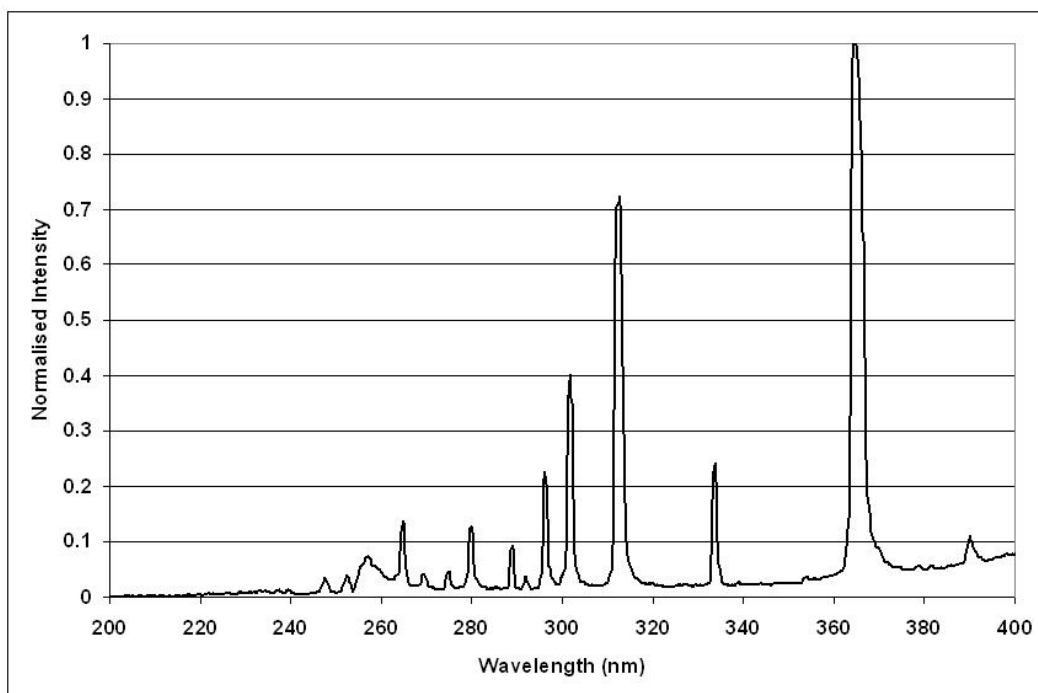


**Figure 3.9. Normalised intensities for Honle Hg UV lamp (H-lamp) used in irradiation experiments.**

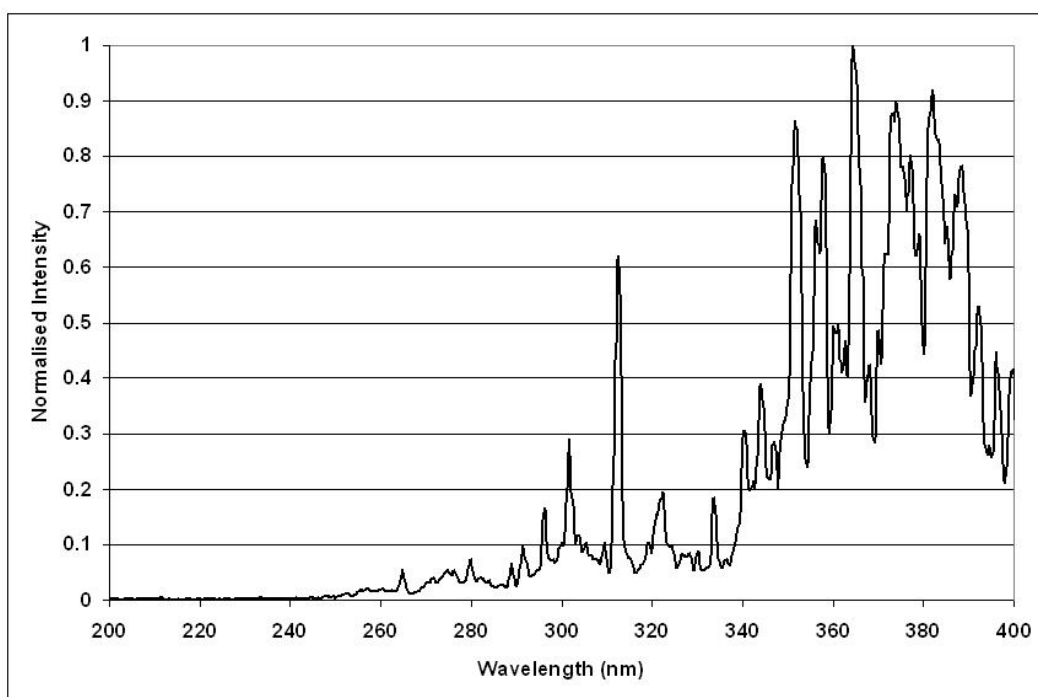


**Figure 3.10. Normalised intensities for Honle Fe doped Hg UV lamp (F-lamp) used in irradiation experiments.**

### 3.9 Irradiation experiments

#### 3.9.1 Stainless steel chamber preliminary tests

A stainless steel block with a tapered hole was manufactured to hold the Ag salt solution, Figure 3.11. The bottom of the block was sealed with a silicone rubber sheet. The block was placed onto the PZT[111] sample and filled with the  $\text{AgNO}_3$  solution, section 3.4.1, a quartz cover slide was placed on top. The assembly was placed into the UV exposure unit on the Peltier cooler and exposed to UV light for 20 minutes using the H-lamp. It was removed from the chamber and the steel block separated from the sample which was then washed with deionised water and blow dried with nitrogen. Characterisation of the irradiated surface was undertaken using SEM.

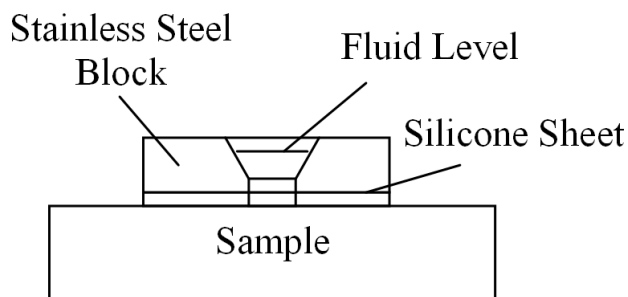


Figure 3.11. Stainless steel block mounted onto sample as fluid holding chamber.

#### 3.9.2 GI PZT Samples

The GI samples were placed into a beaker and immersed in  $\text{AgNO}_3$  solution, section 3.4.1, placed directly onto their surfaces. The sample was then placed into the UV exposure unit, on the Peltier cooler plate. The samples were exposed using the H-lamp for 30 seconds and then removed, washed using deionised water and dried with compressed air. The surface was then imaged using SEM and stored for subsequent analysis.

### **3.9.3 PZT[111] Samples**

The poled PZT[111] sample was placed into a beaker and immersed in the salt solution required for each experiment, section 3.4.1. The sample was then placed into the UV exposure unit for 10 mins, removed washed with deionised water, dried with nitrogen and imaged with SEM, the sequence was then repeated for 20 and 30 mins. The resultant images were stored for subsequent analysis.

### **3.9.4 PZT[100] Samples**

The PZT[100] sample was placed into a beaker and the required salt solution, section 3.4.1, poured on to cover its surface. The beaker was placed into the UV exposure unit, on the Peltier cooler plate, and irradiated for 20 minutes using the H-lamp. After irradiation the sample was removed and washed with deionised water then blow dried with nitrogen ready for analysis. Characterisation of the PZT surface after irradiation was undertaken using SEM, the results stored for subsequent analysis. The process of irradiation and characterisation was repeated using the F-lamp.

### **3.9.5 Monochromatic UV Wavelength experiments**

The experimental rig was as in Figure 3.12. The light from the UV box was transmitted via an Ocean Optics 84-UV-25 collimating lens and QP600-2-SR/BX optic fibre (fibre 1). The output of the fibre was connected to an Edmund Optics Mini-Chromo monochromator. The Monochromator output was fed via a second optic fibre (fibre 2) to an attachment that allowed the light output to be positioned over the PZT sample, as in Figure 3.13.

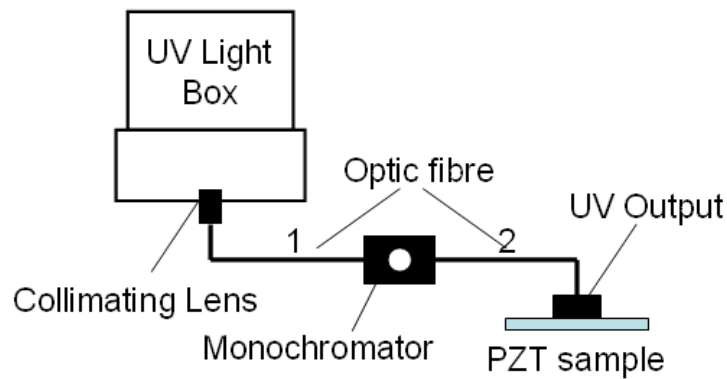


**Figure 3.12. Setup of wavelength test equipment.**

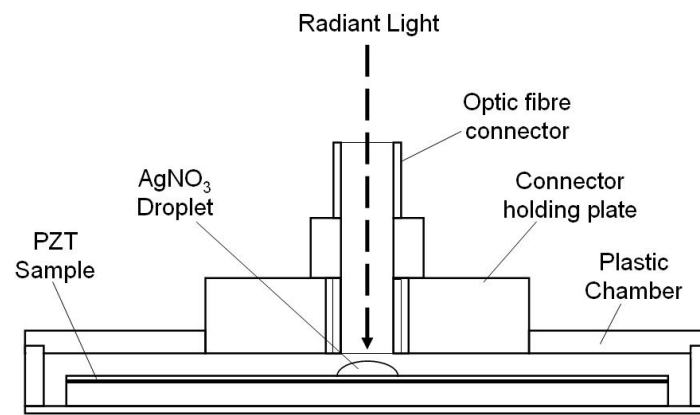


**Figure 3.13. End attachment to position output fibre over PZT sample.**

The spectral output of fibre 1 was measured using an Ocean Optics USB2000-UV-VIS Spectrometer. The fibre was then connected to the end attachment, Figure 3.13, and used to irradiate a poled PZT[111] sample in  $\text{AgNO}_3$  solution, 3.4.1, for 4 hours. Fibre 1 was removed from the end attachment and connected to the input of the monochromator. Fibre 2 was attached to the spectrometer and the desired output wavelength selected. Fibre 2 was connected to the end attachment and a new sample in  $\text{AgNO}_3$  was irradiated, this was repeated for PZT[111] and PZT[100] samples. The irradiated samples were examined under SEM and the images analysed using ImageJ v3.0 analysis program.



## 4 Film structure and metal reduction

### 4.1 Ag wire formation

The preliminary irradiation work was undertaken using a stainless steel chamber machined as in section 3.9.1. The samples were placed at the bottom of the chamber and the reservoir filled with salt solution before being irradiated. It was found that instead of clusters on the PZT surface the Ag had formed wires of varying width and length Figure 4.1.

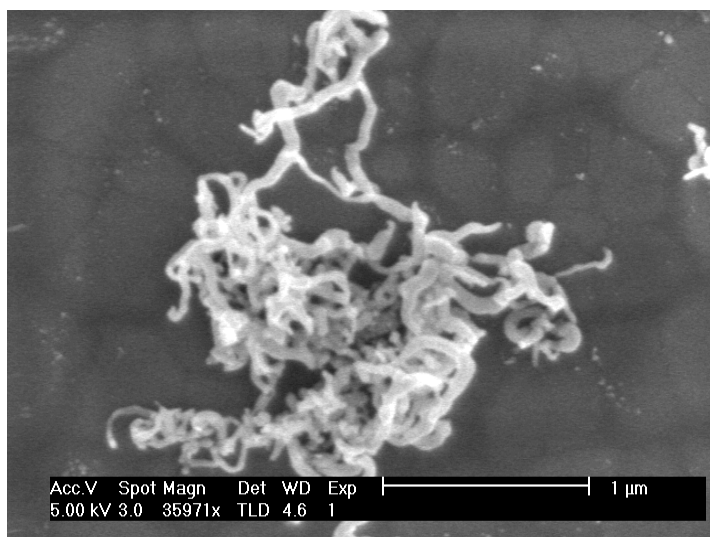


**Figure 4.1** Ag wires formed in steel chamber during UV irradiation. It is believed they grew on step defects on the chamber walls and then fell to the surface of the PZT.

The wire growth is believed to be due to the Ag growing at defects on the stainless steel walls of the chamber which then fell to the surface of the PZT. The steel used in the chamber was made up of three main elements Fe, C and Cr. The work function of Fe and Cr are the same at 4.5 eV, the UV source used was capable of giving this energy. The growth of the Ag wires was thus due to the photoelectric effect where electrons were photoexcited in the metal which then reduced the  $\text{Ag}^+$  ions from solution. The experiment was repeated with a PZT free glass substrate and the same result was

observed, proving that the wire growth was not related to the REDOX reaction at the PZT surface. The process in effect removed the  $\text{Ag}^+$  cations from solution before there was time for a noticeable reaction of the PZT surface. Once the chamber was changed to glass, particle growth was found to occur on the PZT with no Ag wires. These results show that material selection for the chamber was critical and that metal contact with the salt solution should be avoided, the rest of the work was undertaken using a PZT or glass container.

#### **4.2 Metal growth on PZT [111]**

The PZT[111] samples immersed in 0.01 M  $\text{AgNO}_3$  solution and irradiated using the H-lamp for 20 minutes revealed Ag metal cluster growth on the  $\text{C}^+$  domains, and very little growth on the  $\text{C}^-$  as shown in Figure 4.2. The preferential deposition on the  $\text{C}^+$  domains has already been ascribed to the bending of the energy bands within the surface of the PZT and the migration of electrons to the  $\text{C}^+$  domain surface reducing the  $\text{Ag}^+$  cations to metallic  $\text{Ag}^0$ , and presented in section 2.5. This effect has been observed by Kalinin *et al* (2002) and other groups and can therefore be used as a starting point in the following discussion.

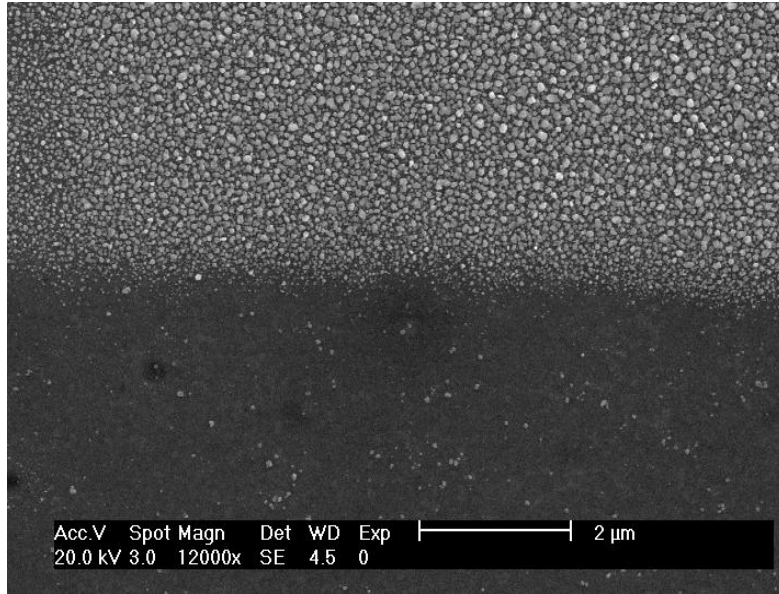


**Figure 4.2 Preferential deposition of Ag clusters across the surface of a  $C^+$  domain of PZT[111] 30/70 thin film after 20 minutes.**

The wide scale nucleation of metal clusters on the  $C^+$  domains is caused by surface crystallographic variations, due to vacancies or dopant impurities, across the film surface (Hanson *et al.*, 2006). For PZT these variations are caused mainly by oxygen vacancies formed during high temperature annealing of the film, the clusters nucleate at these points and then grow outwards as photoexcited electrons migrate to the surface of the  $C^+$  domains and reduce the  $Ag^+$  cations from solution. The clusters grow in both the in-plane x and y and out-of-plane z directions due to mobile electrons photoexcited in the PZT around the bottom edge of the cluster flowing through the silver, these free electrons then reduce  $Ag^+$  ions at the cluster surface as it grows, Figure 4.3.

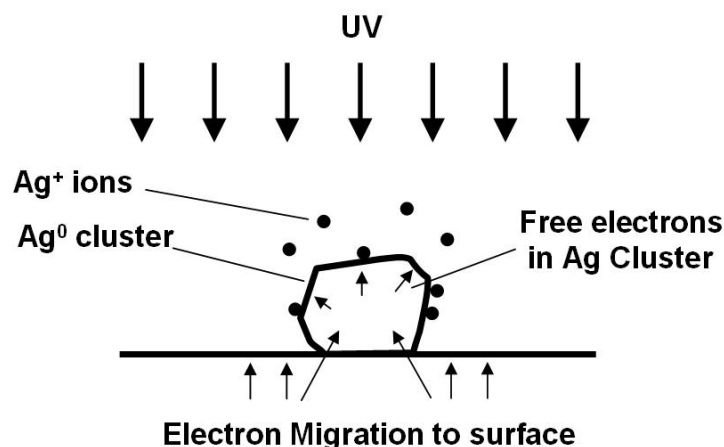


**Figure 4.3** Single cluster on C<sup>+</sup> PZT domain. Electrons photoexcited in PZT film migrate to the surface of a C<sup>+</sup> domain. Where a cluster is growing the electrons near the edge migrate into it. These free electrons can then reduce the Ag<sup>+</sup> ions from solution to Ag<sup>0</sup> on the cluster surface, thus it grows both sideways and outwards.

The Ag grows across the C<sup>+</sup> domain not as a continuous smooth sheet but a rough film of clusters. This growth is partly explained by the process just discussed, but the full process includes the growth retardation mechanism that controls final cluster size. In order to study this a 2 nm thick Ag film was grown onto quartz glass, section 3.7.2, and its transmittance spectra measured using a photospectrometer, the output of which can be seen in Figure 4.4.

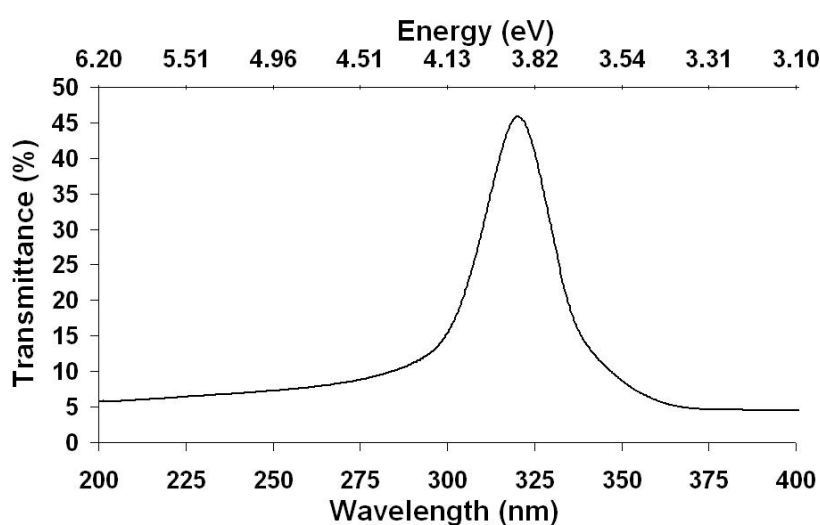


**Figure 4.4** Transmittance spectra for light through ca 2 nm Ag film. Up to 95 % of the UV above 4.5 eV is blocked.

The plot shows a transmission peak at about 3.9 eV which drops off at both higher and lower energies. It can be seen that 90 % of photons with energy above 4.1 eV, the minimum energy required to excite electrons to the conduction band, are blocked by the Ag film. Therefore cluster growth retardation is due to the Ag clusters shadowing the PZT surface as they grow, when the cluster edges meet electron migration stops and thus cluster growth also stops, Figure 4.5. This means that the final size of the clusters is controlled by the space between neighbouring nucleation points

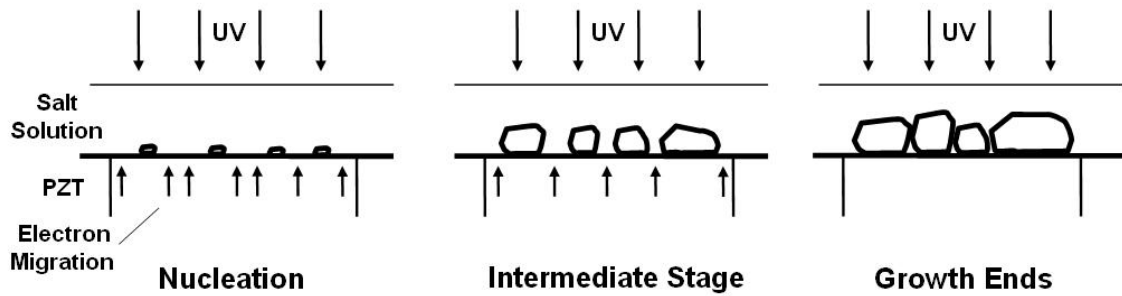


**Figure 4.5** Ag cluster growth retardation mechanism, clusters nucleate and grow as electrons migrate to the surface due to UV irradiation. As the clusters grow they shade the surface from the light until their edges meet and the surface is totally masked, which causes electron migration to stop.

### 4.3 Growth at grain boundaries

The PZT[111] film discussed in section 4.2 was a homogenous sample with columnar grains in the range of 70 to 100 nm (Dunn and Whatmore, 2002). The structure was such that cluster growth occurred across the  $C^+$  domains of the film. If, however, the film consisted of large grains with a rougher surface and long grain boundaries such as the GI1 sample then the metal cluster growth varied greatly across the surface as will be shown here. Figure 4.6 presents a perovskite rosette surrounded by a non-ferroelectric pyrochlore phase. It can be seen that after 1 minute of irradiation clusters have grown within the perovskite phase on  $C^+$  domains but not on the pyrochlore. The lack of

growth on this phase is due to the fact that as stated by Lee *et al.* (2005) the pyrochlore has a wider bandgap than the perovskite phase, indeed the photon energy required to generate electron-hole pairs in the pyrochlore are blocked by the  $\text{AgNO}_3$  solution which absorbs 95-100 % of energy at *ca* 4.9 eV upwards, Figure 4.7. Therefore the photoactivity of the pyrochlore surface will be inhibited through a lack of available photons.

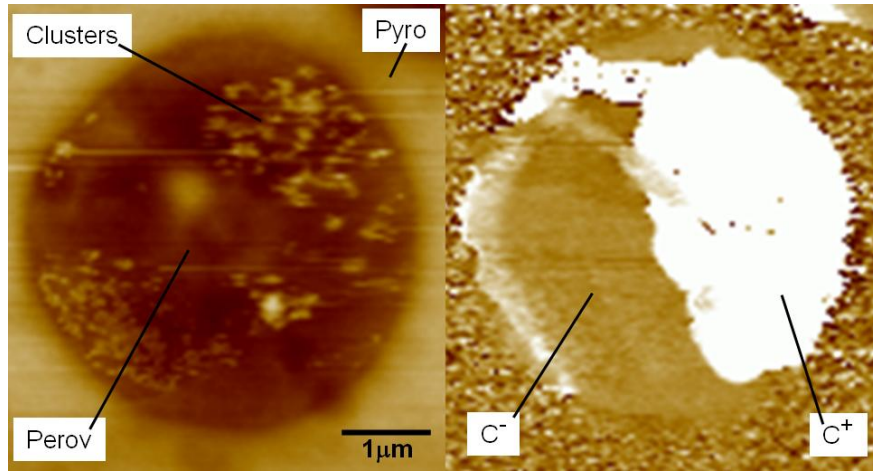


**Figure 4.6** AFM (left) and PFM (right) images of single perovskite rosette surrounded by pyrochlore phase on GI1 film after 2 minute UV irradiation. The Ag clusters are mainly on the  $\text{C}^+$  domain, white area in PFM image, within the rosette and no clusters have formed in the pyrochlore phase.

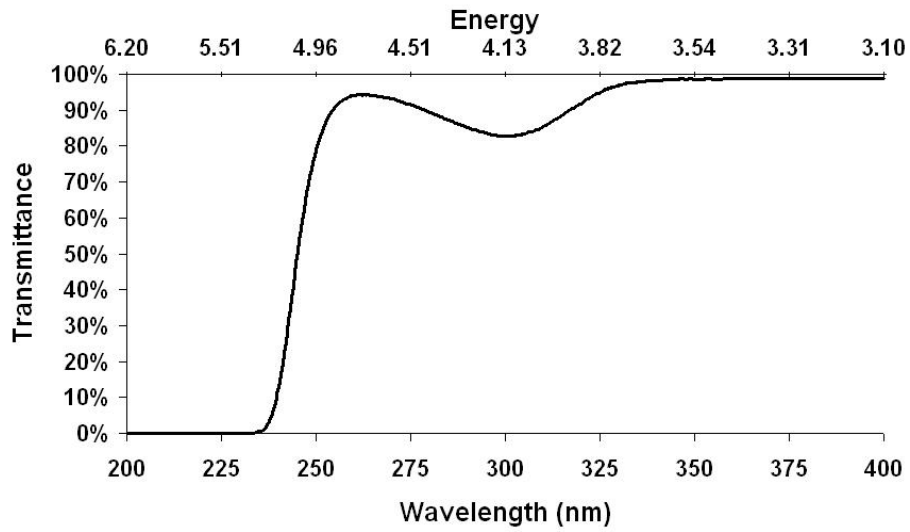


**Figure 4.7** Transmittance of 0.01 M  $\text{AgNO}_3$  solution, photons with energy lower than 4.9 eV can pass with little absorption, but energies above this are strongly blocked by the solution. This means that 5 eV is the maximum photon energy incident to the surface of the PZT during irradiation.

In Figure 4.8 two adjacent rosettes on the GI1 film can be seen after 45 second of illumination in  $\text{AgNO}_3$  solution along with its associated PFM image showing the orientation of the polar domains.

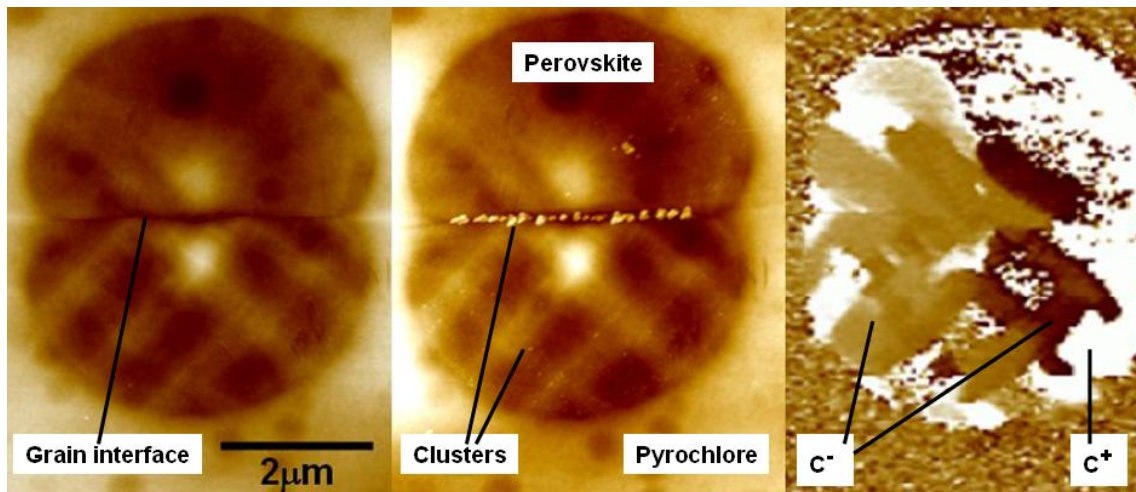


**Figure 4.8** AFM images of GI1 sample before (left) and after (middle) 45 seconds of UV exposure in  $\text{AgNO}_3$  solution. Large Ag clusters have grown at the grain boundary between the two connecting rosettes, there are also some smaller clusters on some areas of the  $\text{C}^+$  domains. On the right is the piezoresponse force image of the same area, showing  $\text{C}^+$ , and  $\text{C}^-$  polarisation.

The most striking features of the left image in Figure 4.8 are the clusters that have grown at the interface between the two rosettes. These clusters are much larger, average diameter *ca* 150 nm, than those that have grown on the  $C^+$  domains elsewhere on the rosettes which average *ca* 40 nm. It is possible to approximate the ratio of electrons excited to the surface at the grain boundary to that on a  $C^+$  domain within the rosette. If the effective diameter of an Ag atom is taken as 0.288 nm, the clusters are assumed to be hemispherical and the reduction of an  $Ag^+$  cation requires one electron then the ratio of electrons excited in each region can be estimated. The 150 nm clusters therefore consist of *ca*  $7 \times 10^7$  atoms and the 40 nm clusters *ca*  $1.35 \times 10^6$  atoms. As each  $Ag^+$  ion requires one electron to reduce it to metallic  $Ag^0$  the ratio of electrons released between the grain boundary and the  $C^+$  domains can be calculated and is found to be *ca* 51:1. Therefore the clusters at the grain boundaries are growing around 51 times faster than on the  $C^+$  domains. This effect can also be seen in Figure 4.9 where a line fault occurs across the surface of the rosette the Ag has grown preferentially along it.

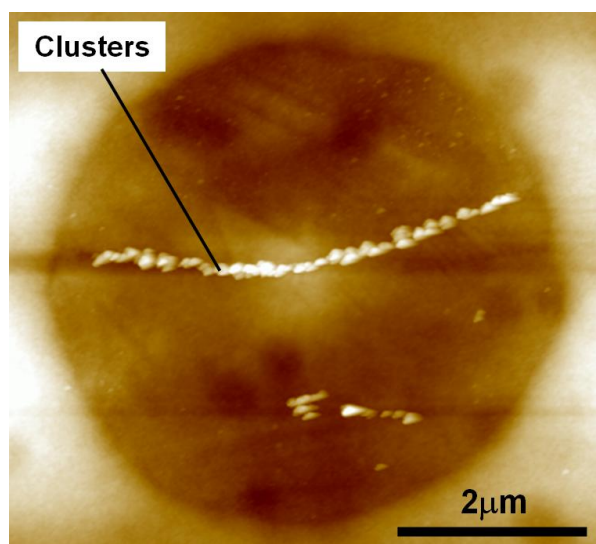


**Figure 4.9** AFM image of Ag growth on a line defect in the grain structure of a single rosette after 45 seconds exposure.



An important feature to notice in Figure 4.8 is that the interface clusters have grown irrespective of the underlying polar domains as can be seen by comparing the right hand PFM image. This would appear somewhat at odds with the currently accepted theory of metal growth based on band bending and the transport of electrons to the surface of  $C^+$  domains due to the SCR as seen for the PZT[111] films. A closer analysis in fact shows that the same process of electron migration due to a SCR is responsible for the growth at the interface but on a greater scale. The increased rate of growth at the grain boundary and line fault can be explained by examining the energy band structure at these points. As stated in section 2.6 an internal field occurs at the semiconductor grain boundary interfaces due to the lattice mismatch of adjacent grains. If the core of the boundary is positively charged as in Figure 4.10 then during illumination electrons excited in the body of the grain near the boundary migrate to the boundary core. This is not conduction as the electrons are not crossing the boundaries but migrating to either side due to the SCR running down the interface. This gives an increased flux of electrons available for the reduction of cations at the surface of that boundary.

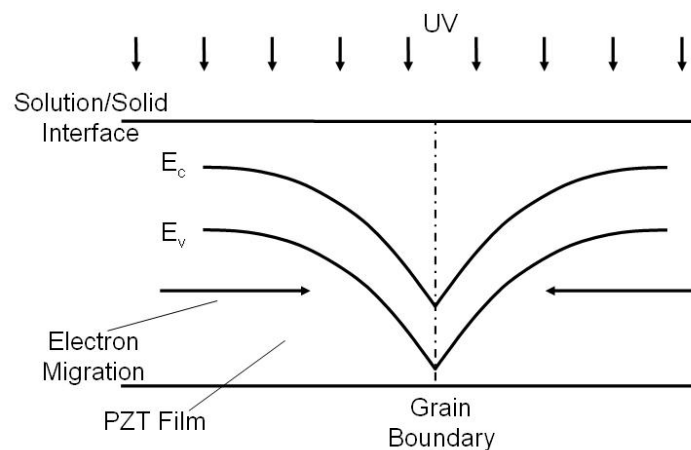


**Figure 4.10 Migration of electrons in the PZT to grain boundaries during irradiation. The internal electric field due to the lattice mismatch at the core causes downward band bending at the grain boundary and thus electrons migration to it.**

#### 4.4 Boundary effect ranking

From the work using the GI1 samples it is possible to condense the types of boundary that exist on the film to 4 types. Two are related to the physical structure of the film, these are the interphase boundary, where the perovskite and pyrochlore phases meet and the grain boundary where the edges of the rosettes meet each other. The other two boundaries are the domain boundary, where ferroelectric domains of different orientation meet, and the surface state effects or domain polarization. These can be seen diagrammatically in Figure 4.11.

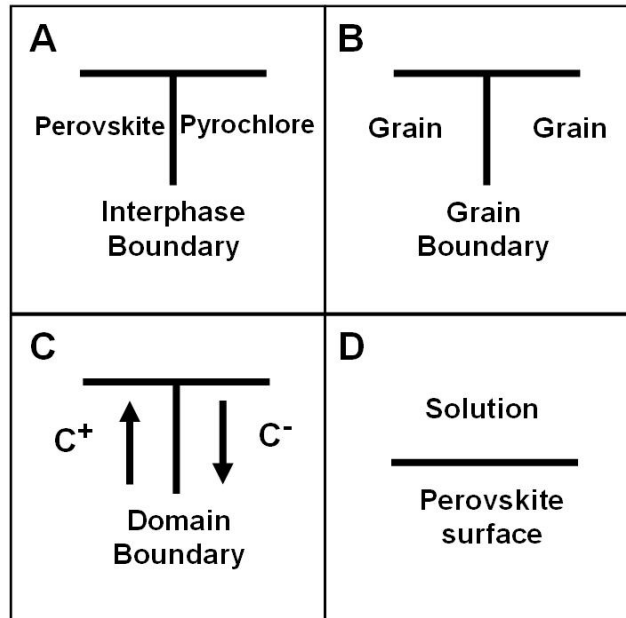


**Figure 4.11** The four types of boundary found on the GI1 PZT sample, A) interphase boundaries where the perovskite and pyrochlore phases meet , B) grain boundaries where the edges of the rosettes meet, C) domain boundaries where polar domains meet, and D) surface state effects and domain polarization.

These boundaries can be ranked according to their effects on the rate of cluster growth, Table 4.1.

**Table 4.1 Ranking of boundary types with respect to Ag cluster growth rate on PZT films.**

<b>Rank</b>	<b>Type</b>
<b>1</b>	Grain Boundaries
<b>2</b>	Positive Domains
<b>3</b>	Domain Boundaries
<b>4</b>	Interphase Boundaries

As shown in Figure 4.8 the most rapid growth is seen at the grain boundaries and defects in the surface because of the greater availability of electrons due to the fields generated by the defects around the core. The second highest rate of growth is found on surfaces with a  $C^+$  polarisation, Figure 4.2. The growth here is due to the migration of electrons as a result of the subsurface SCR. It has been shown by Hanson *et al.* (Hanson *et al.*, 2006), section 2.8, that there is preferential growth of metal at domain boundaries on crystals such as  $LiNbO_3$  but this is not the case for PZT. The crystallographic defect structure at the PZT surface, i.e. the vacancy/dopant density, has such a great effect that domain boundaries are not a major contributor to cluster growth, see Figure 4.2, thus they are third in the ranking. Finally the interphase boundary is fourth as there is no observable preferential deposition at these points, as can be seen in Figure 4.6.

These results show that the preferential deposition of metal onto the surface of PZT using UV irradiation is dependent not only on its ferroelectric properties but also its structure. The deposition rate at the grain boundaries is greater than that due to the polar domains; therefore films such as the GI1 samples would be unsuitable for use as templates in the creation of nanoparticles of defined shape. Though not of use in the creation of shaped nanoparticles, the high rate of ion reduction at these boundaries does mean that it could be used in applications such as the removal of metal contaminants from water.

#### 4.5 Crystallographic orientation and metal deposition

Unlike the PZT[111] sample where there was a definite demarcation between the growth of Ag on the  $C^+$  domain and none on the  $C^-$ , the PZT[100] film showed deposition on both when irradiation with the H-lamp, though the clusters on the  $C^+$  domains were larger, *ca* 118 nm, than those on the  $C^-$ , *ca* 56 nm, Figure 4.12. This is the first time that  $C^-$  domain growth has been observed.

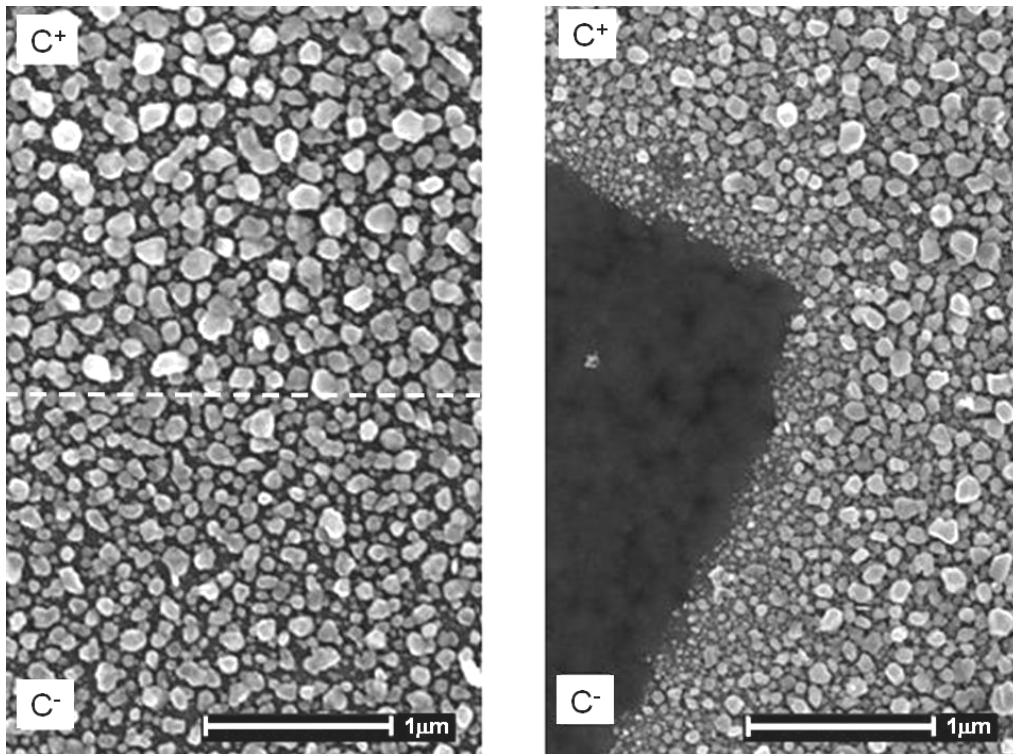


**Figure 4.12** Silver deposition on the surface of PZT(30/70) after 20 minutes exposure to the H-lamp. Left, PZT[100] with highly [100] orientated structure has cluster growth across both domains, the dashed line showing the interface between the  $C^+$  and  $C^-$  domains. Right, PZT[111] with highly [111] crystallographic orientation displays definite demarcation between  $C^+$  domains where clusters have grown and the  $C^-$  where there is no growth.

The two PZT films used here were manufactured using the same methodology with the same sol, the only difference was the majority crystallographic orientation of the crystallites in the ceramic. It is known that the surface charge for the two orientations is

different, section 2.3, therefore the variation in deposition between the PZT[111] and PZT[100] films could be related to these differences in surface charge.

At the surface of the ferroelectric the charge,  $\rho_s$ , magnitude and polarity is defined by the balance between the fixed charges,  $\rho_t$ , due to surface states and the charge generated by the underlying domain polarisation,  $\rho_p$ , Equation 4.1.

$$\rho_s = \pm|\rho_t| \pm |\rho_p|$$

**Equation 4.1**

The sign of  $\rho_p$  is dependent on the orientation of the ferroelectric domain whereas  $\rho_t$  is dependent on the type of surface trap state and independent of domain polarisation. For PZT the majority of surface states are caused by oxygen vacancies (Mihara *et al.*, 1992). These vacancies make the surface n-type, i.e.  $\rho_t$  is positive, independent of the polarisation of the ferroelectric domain. As already shown in section 2.4 PZT is a wide bandgap semiconductor which in the bulk is p-type, thus the majority carriers are positive holes. In a  $C^+$  domain where the dipole points towards the surface, i.e.  $+P_r$ ,  $\rho_p$  is positive and so a hole depletion region forms causing the energy bands to bend downwards as the positive charge carriers are repelled into the bulk and inversion occurs. In a  $C^-$  domain where the dipole points away from the surface  $\rho_p$  is negative, if  $\rho_p$  is greater than  $\rho_t$  it will generate a negative  $\rho_s$  though of lesser magnitude than on the positive domain. The negative surface charge causes an accumulation of holes below the surface and thus upward band bending occurs. The degree of energy band bending in the ferroelectric is thus dependent on the spontaneous polarisation and the free charge carriers in the film and any variation will affect the width of the SCR. Equation 4.2 illustrates this, where  $w$  is the width of the SCR and the denominator is the

charge density within the bulk due to holes,  $h^+$ , electrons,  $e^-$ , acceptors,  $N_A^+$ , and donors,  $N_D^-$ , with  $q$  being the elementary charge.

$$w = \frac{\rho_s}{q(h^+ + N_D^- - e^- - N_A^+)}$$

**Equation 4.2**

Equation 4.2 shows that if  $\rho_s$  is reduced, i.e. if the  $P_r$  is lowered, or the number of free carriers in the film increases as happens during photoexcitation, so the space charge width decreases. This effect explains the difference in deposition of Ag on the PZT[100] and PZT[111]  $C^-$  domains. The  $P_r$  of [100] orientated PZT is around 60 % of that for [111] (Kobayashi *et al.*, 2005), *ca* 14  $\mu\text{C cm}^{-1}$  and *ca* 21  $\mu\text{C cm}^{-1}$  respectively. This means that the PZT[100] will have a narrower SCR than the PZT[111] samples, assuming the charge carriers are equal for both, as illustrated in Figure 4.13.

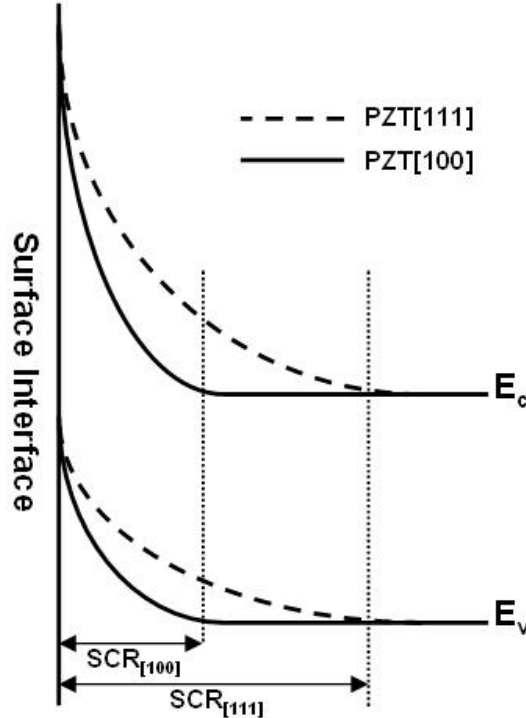


**Figure 4.13** Comparative diagram of energy band bending at  $C^-$  domain surface of PZT[111] and PZT[100]. The space charge regions are such that  $\text{SCR}_{[111]} > \text{SCR}_{[100]}$  due to the greater curvature of the PZT[100] band bending.

In  $C^+$  domains where there is no barrier to the migration of electrons to the surface during UV irradiation, due to downward band bending, this variation in the SCR width does not have a great impact. In  $C^-$  domains, however, this is not the case, the greater width of the SCR in the PZT[111] samples reduces the probability of electrons tunnelling to the surface. In the PZT[100] with its reduced width the chances of an electron migrating to the surface are greatly enhanced. In fact due to the penetrability,  $T$ , of the potential barrier being an exponential function (French and Taylor, 1998), Equation 4.3, a small change in the space charge width can lead to a significant increase in an electrons ability to tunnel to the surface during illumination.

$$T \approx e^{-2\alpha w} \quad \text{where} \quad \alpha = \frac{1}{\hbar} \sqrt{2mE}$$

**Equation 4.3**

In Equation 4.3  $w$  is the width of the SCR,  $m$  is the mass of the particle moving through the barrier and  $E$  is the barrier height. As already shown the width of the SCR can be changed by a variation in the surface charge of the ferroelectric. Because PZT is a p-type material Equation 4.2 can be reduced to Equation 4.4.

$$w = \frac{\rho_s}{qN_A}$$

**Equation 4.4**

The difference in the SCR width,  $\Delta w$ , between PZT in its [111] and [100] orientation is therefore given by Equation 4.5

$$\Delta w = w_{[111]} - w_{[100]} = \frac{\rho_{s[111]} - \rho_{s[100]}}{qN_A}$$

**Equation 4.5**

If the surface charge values given by Kobayashi *et al.* (2005) for PZT of 21  $\mu\text{C}/\text{cm}^2$  for [111] and 14  $\mu\text{C}/\text{cm}^2$  for [100] are used, then the surface charge difference is -7

$\mu\text{C}/\text{cm}^2$ , also if the density of ionised acceptors  $N_A$  is taken as  $10^{20} \text{ cm}^{-3}$  as presented by Pintilie and Alexe (2005) then  $\Delta w = 4.4 \text{ nm}$ .  $\Delta w$  can be substituted into Equation 4.3 so that the ratio between  $T_{[111]}$  and  $T_{[100]}$  can be calculated as in Equation 4.6.

$$\frac{T_{[100]}}{T_{[111]}} = e^{2\alpha\Delta w}$$

**Equation 4.6**

If the barrier height,  $E$ , is taken as  $1 \text{ eV}$  (Scott *et al.*, 1999) then the ratio of penetrability is  $[100] = 3.39 \times 10^{19} \times [111]$ , i.e. in a  $C^-$  domain on  $[100]$  orientated PZT the probability of silver reduction is  $10^{19}$  times higher than that for  $[111]$ .

#### **4.6 Effect of illumination on band bending and Ag deposition**

As there is no noticeable deposition of Ag on the  $C^-$  domains of the PZT $[111]$ , even at higher photon energies, it is useful to study the PZT $[100]$  samples to gain a better understanding of the effects of photon energy and flux on surface metal growth. In order to study these effects two UV sources of different spectral signatures were used to irradiate the PZT $[100]$  surface while it was immersed in the  $0.01 \text{ M AgNO}_3$  solution. The sources used were the H-lamp and the F-lamp, the spectra of which can be found in Figure 3.9 and Figure 3.10 respectively. The resulting deposition can be seen in Figure 4.14 where Ag clusters have grown across both domains for the H-lamp but only on the  $C^+$  domains when the F-lamp is used.



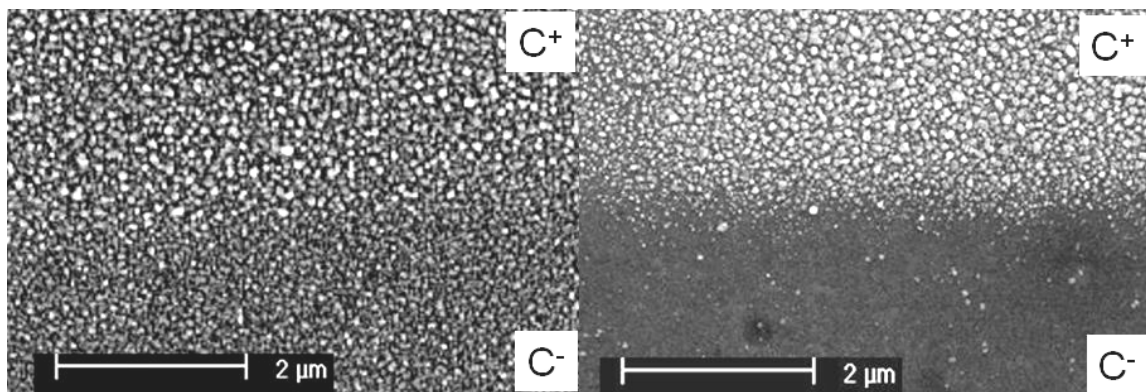


**Figure 4.14** Ag deposition on PZT[100] sample after 20 minutes UV irradiation. Left, H-lamp illumination gives growth across both  $C^+$  and  $C^-$  domains. Right, F-lamp illumination gives deposition on  $C^+$  domain only.

Figure 3.9 and Figure 3.10 show the spectral intensity plots for the two light sources in a normalised form, the maximum photon energy being that which impinges on the PZT surface before being absorbed by the metal salt solutions. For  $\text{AgNO}_3$  solution the greatest absorption occurs at *ca* 5 eV and upwards as shown in Figure 4.4. Dividing the H-lamp spectra by the F-lamp gives the ratio of intensity between the two sources, as shown in Figure 4.15 below. This plot shows that above 4.59 eV the H-lamp has a greater intensity and thus gives a greater flux of photons than the F-lamp.

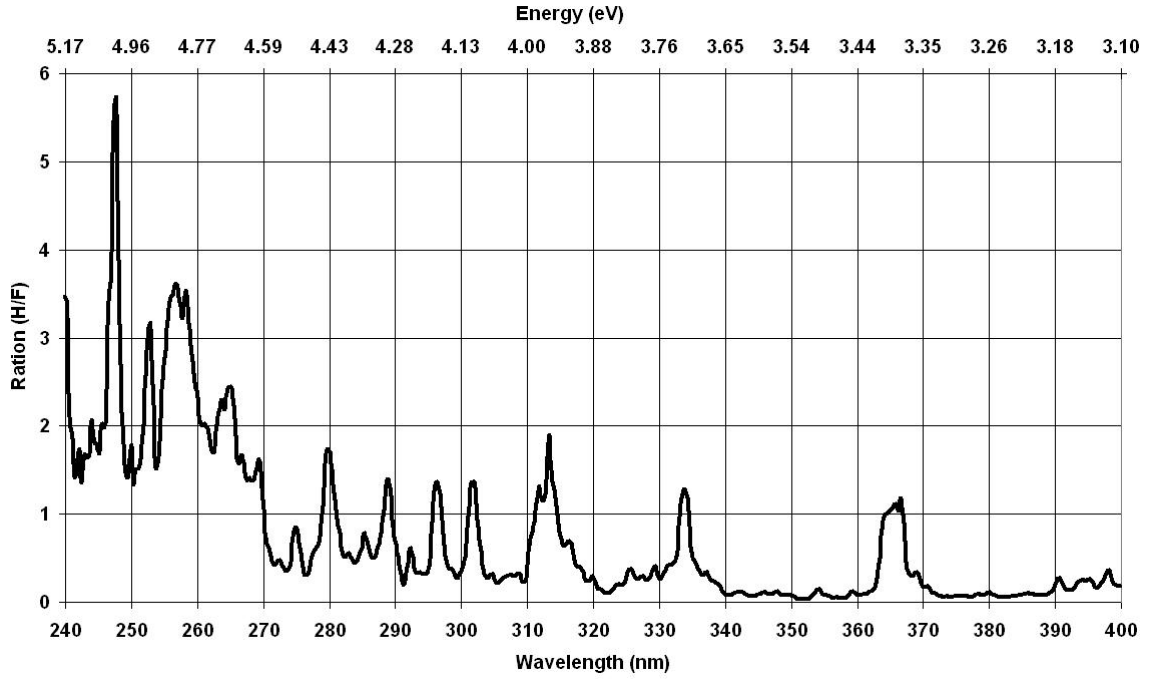


**Figure 4.15 Plot of ratio of intensity between H-lamp and F-lamp versus wavelength.**

As shown throughout this work when the PZT surface is illuminated by UV light, electron-hole pairs are generated in the film. These charge carriers can, dependent on polarisation, migrate to the surface or the bulk or they can recombine and decay to the ground state. The mean time between a photoexcited charge carrier being generated and its final recombination is known as its free lifetime,  $\tau$ . The additional free electrons and holes generated by incident photons is given by Equation 4.7 and Equation 4.8 (Bube, 1967).

$$g\tau_n = \Delta n$$

**Equation 4.7**

$$g\tau_p = \Delta p$$

**Equation 4.8**

Here  $g$  is the generation rate in number of electron/hole pair per unit volume per second, and  $n$  and  $p$  are the electrons and holes, respectively. The rate of change of electrons and holes is given by Equation 4.9 and Equation 4.10 (Jenkins, 1995).

$$\frac{dn}{dt} = g_n - \frac{n}{\tau_n}$$

**Equation 4.9**

$$\frac{dp}{dt} = g_p - \frac{p}{\tau_p}$$

**Equation 4.10**

By increasing the flux of incident photons there is an increase in  $g$  which in turn exceeds the recombination rate, this means that carriers will accumulate faster than they can recombine. Those photoexcited electrons that migrate to the surface can react with ions in solution and thus take part in a photochemical reaction. The rate at which a chemical reaction can occur at the surface is limited by various factors such as the chemical kinetics and local ionic concentrations. As more carriers are excited to the surface those that do not take part in a surface reaction will accumulate, this in turn leads to an alteration in the structure of the energy bands at the surface.

In a  $C^-$  domain a barrier to electrons is present and so no reduction of metallic ions is expected in these domains. As discussed in section 4.5 the PZT[100] film has a relatively narrow SCR. If the number of photogenerated electrons in the film increases due to the processes above the width will decrease and an increased probability of electron tunnelling results. Figure 4.16 is a representation of how the bands bend and thus the SCR alters as photon flux increases. It can be seen that the amount of bending that occurs increases with flux, therefore with (a) and (d) there is a less bending of the energy bands and thus a wider SCR, in the  $C^-$  domain the width is enough to stop electrons tunnelling to the surface and no metal reduction occurs there. As the flux increases so the bending becomes steeper, in (b) and (e) the SCR has reduced, and so in (e) there is an increased chance of electrons tunnelling to the surface. Finally in (c) and

(f) the bands have a very steep curve and thus the SCR is greatly reduced, in (f) the width is now low enough for a high probability of electron tunnelling and thus increased metal reduction.

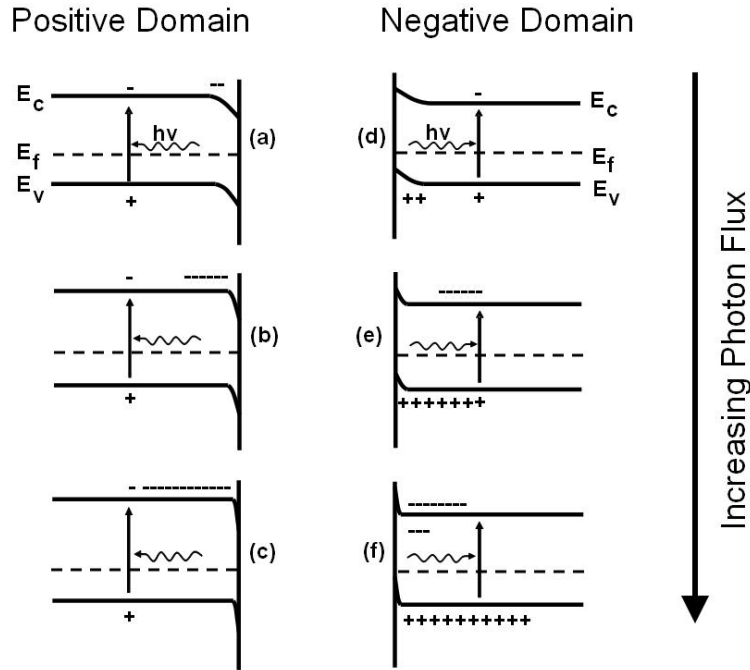


**Figure 4.16** Band diagrams for PZT immersed in  $\text{AgNO}_3$  solution. As photon flux increase so the steepness of the band bending increases, this in turn leads to a narrower SCR.

The work presented in this chapter has shown that the reduction of metal ions such as  $\text{Ag}^+$  at the PZT surface is greatly influenced by film structure. It has shown that at defects such as grain boundaries  $\text{Ag}^0$  clusters grow 51 times faster than elsewhere on the film. Also it has shown that the orientation of the film has to be taken into account when considering the metal growth mechanism. On  $[111]$  oriented films  $\text{Ag}^+$  only reduces on  $\text{C}^+$  domains whereas, if given enough flux, the  $[100]$  film will also show growth on the  $\text{C}^-$  domains as well. This variation is explained by the difference in width of the space charge region for each film due to the different surface charge magnitudes for each orientation. As the  $[100]$  film has a narrower space charge region than the  $[111]$

orientation electrons have a higher chance of tunnelling through the C<sup>-</sup> domain and thus reducing Ag<sup>+</sup> cations.

## 5 Photon energy dependence of metal reduction

It was shown in the previous chapter that an increase in photon flux, when considered with film orientation, [111] and [100], affects the growth characteristics of Ag clusters on the PZT surface. Here the discussion is focused on the effect of photon energy at constant flux on cluster growth. The use of monochromatic, bandwidth 5nm, as opposed to wideband UV, bandwidth >200 nm, allows for the interactions at the PZT surface/solution interface to be studied as a function of wavelength thus enabling an analysis of the growth characteristics of Ag clusters from AgNO<sub>3</sub> solution linked to a particular energy.

### 5.1 *Ag<sup>0</sup> Cluster size and density*

The resulting deposition across the surface of the PZT showed that an increase in photon energy led to an increase in Ag<sup>0</sup> cluster cross sectional area for both the [111] and [100] orientated PZT films. Deposition started on the [111] oriented samples at 4 eV and the [100] at 4.4 eV. Figure 5.1 and Figure 5.2 show the C<sup>+</sup> domains for the [111] and [100] samples, respectively.

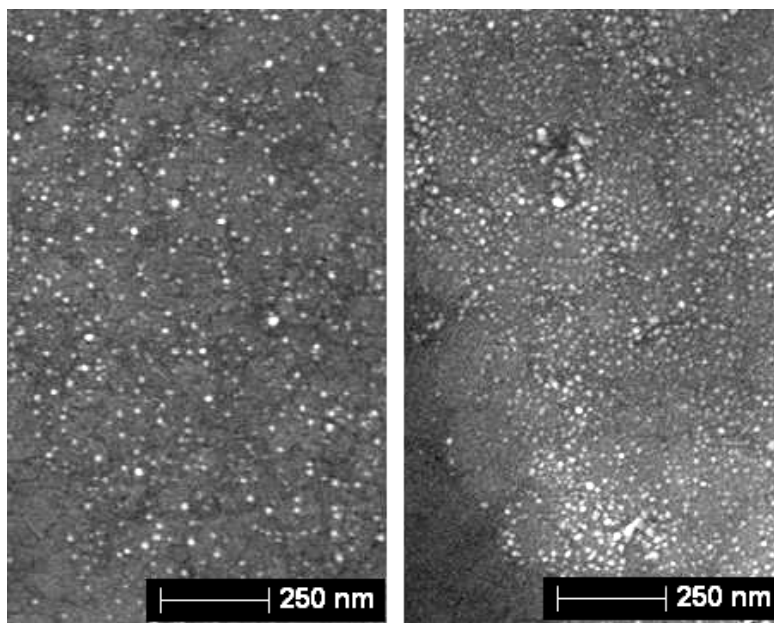


**Figure 5.1**  $C^+$  domain on [111] orientated PZT 30/70, after irradiation with 4.1 eV (Left) and 5 eV (Right) UV.

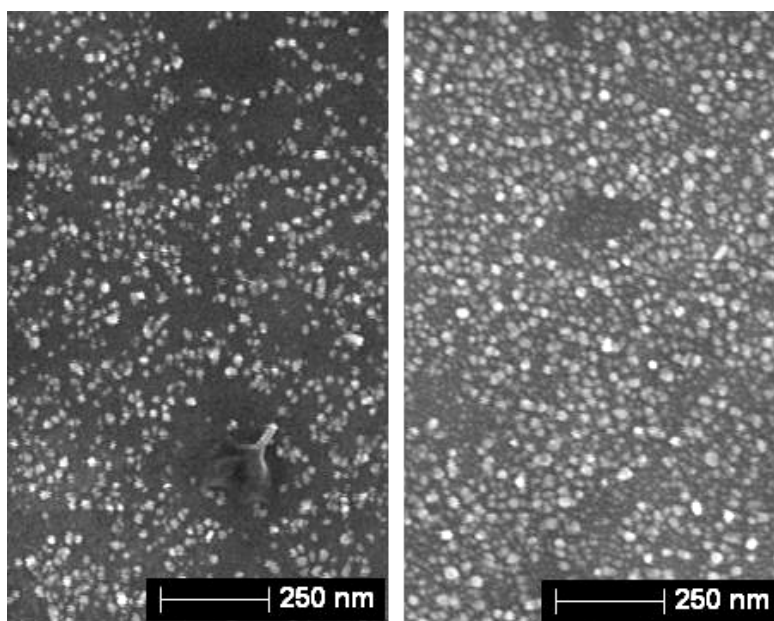


**Figure 5.2**  $C^+$  domain on [100] orientated PZT 30/70, after irradiation with 4.4 eV (left) and 5.0 eV (Right) UV.

The average  $Ag^0$  cluster cross sectional area for both film orientations is plotted in Figure 5.3 for a range of photon energies. It can be seen that both orientations follow a similar trend, as photon energy increases so there is a linear increase in cluster size. This linearity stops at ca 4.8 eV where there is an increased size to energy ratio. Deposition

did not occur above 5.06 eV, which was the cut off point for UV transmission through the AgNO<sub>3</sub> solution Figure 4.7.

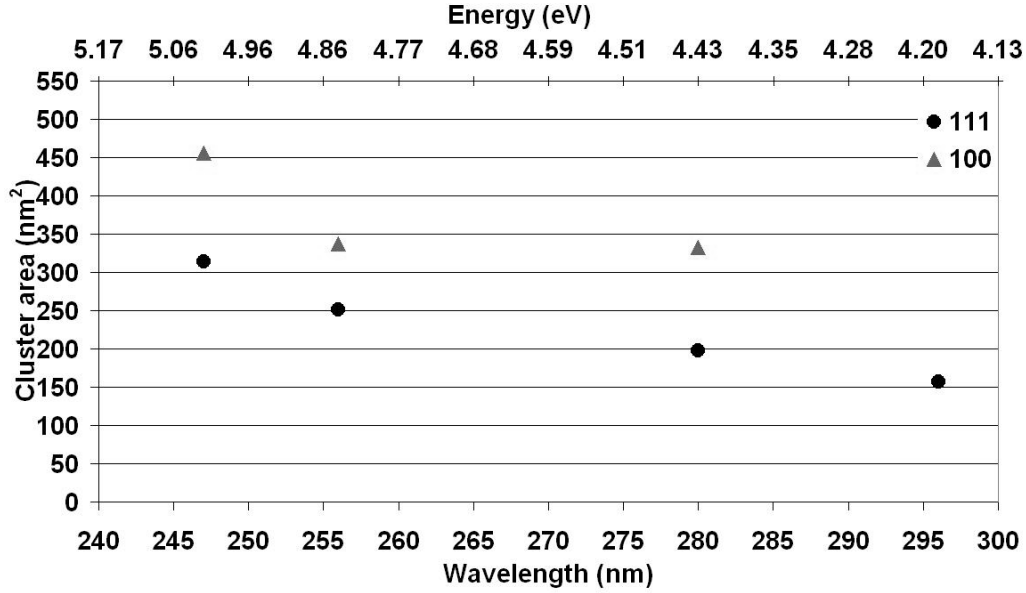


Figure 5.3 Ag cluster size v photon wavelength and energy for the [111] and [100] samples.

It is interesting to note that the Ag<sup>0</sup> cluster density for both samples also seems to be linked to increasing photon energy. This is at odds with the results obtained by Dunn and Sharp (2008) who showed that the final surface density of the clusters is directly related to the initial number of nucleation points on the PZT surface, i.e. the nucleation density does not significantly increase over time during irradiation. Figure 5.4 shows this apparent increase in density, as with the cluster cross sectional area there is an increase in cluster numbers per unit area to increasing energy.



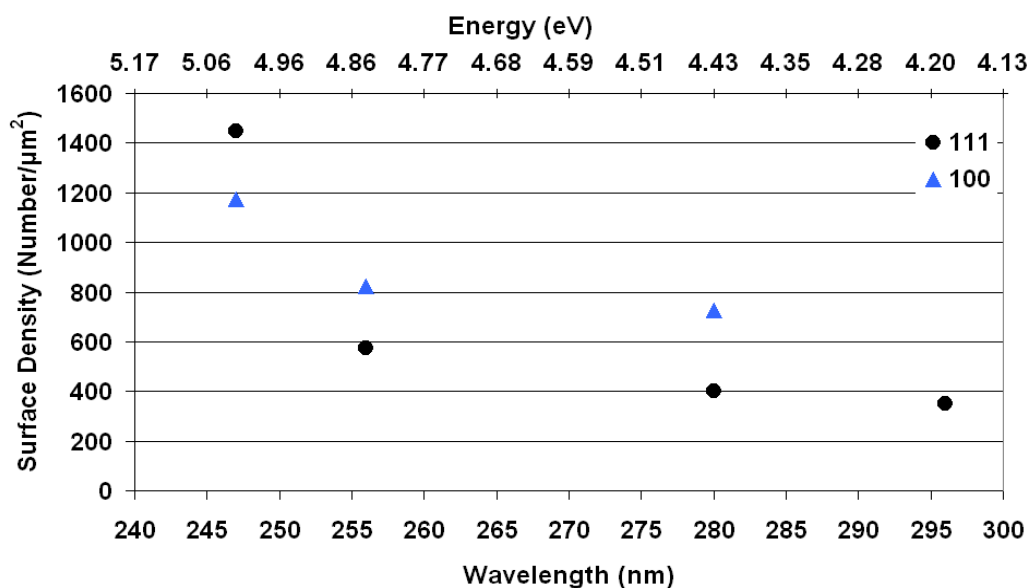


Figure 5.4 Apparent change in Ag cluster density on C<sup>+</sup> domains verses photon energy.

Indeed Lei *et al.* (2004) in their work on Ag<sup>0</sup> metal growth on PZT also show a variation in cluster density over increasing irradiation time, Figure 5.5.

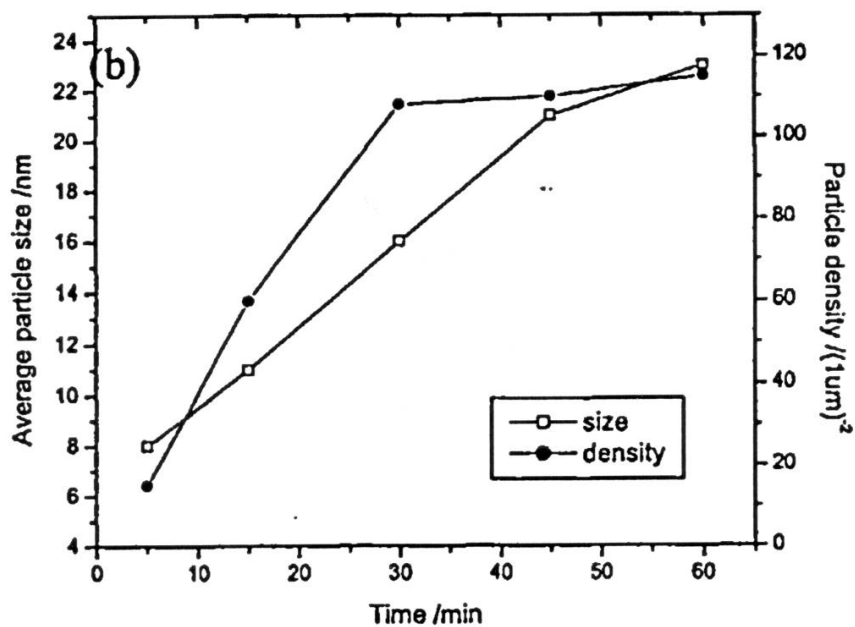


Figure 5.5 According to work by Lei *et al.* (2004) the surface density of the Ag clusters increased with irradiation time.

This mismatch in results can be explained by the measurement techniques used by the various groups. Lei *et al.* used an AFM to image the post exposed PZT samples. This method can have a certain amount of uncertainty when studying clusters that are close together, of the same order of size and are in their early nucleation stages. Also if morphological variations in the surface of the PZT are combined with these factors uncertainty can result, a fact that is stated in Lei's work. The images obtained by Dunn and Sharp used ultra high resolution SEM, a method that though not able to give height information can be used to demarcate clusters from surface morphology when the clusters are still in early stage nucleation. It seems likely that the increase in density seen in Figure 5.4 and Figure 5.5 is not due to new nucleation points forming during irradiation at increasing energy or time but points that formed at initial illumination that are growing at a lesser rate than those around them, thus only becoming visible in our images at a later point.

## **5.2 Grain boundaries and the Stern layer**

In order to understand the mechanism of nucleation point formation and cluster growth it is necessary to consider the processes occurring at the PZT surface/solution interface. It has been shown in section 4.3 that with the GI1, large grained PZT on ITO, samples the main  $\text{Ag}^0$  deposition occurred at the grain boundaries, with a growth ratio of 51 to 1 compared to other areas of the film. This preferential deposition also occurred on the finer grained PZT[111] samples where a majority of the observed clusters were at grain boundaries (Dunn and Sharp, 2008) though at a smaller scale. This means that with respect to the reduction of cations the grain boundaries are the most photoactive areas on the PZT surface for the reasons given in section 4.3.

As discussed in section 2.7 the interface between the PZT and a salt solution is covered by a stern layer, which is made up of the inner and outer Helmholtz planes, and a diffusion region. These external ionic layers are in fact one side of the energy reduction process that takes place at the ferroelectric surface interface, the other being the bending of the energy bands and migration of carriers internal to the interface. If the surface is only partially screened by the internal process the external surface potential that forms is counteracted by these outer ionic layers. As PZT has a high quantity of surface defects, estimated at  $10^{14} \text{ cm}^{-2}$  (Scott, 2000), which are partially compensated by free carriers most of the energy compensation takes place due to internal band bending, though this does not fully screen the surface and so a Stern layer still forms. Interestingly single crystal materials such as barium titanate and lithium niobate have few free carriers and thus the main compensation mechanism is the stern layer formation (Hanson *et al.*, 2006).

Equation 2.5 in section 2.5, repeated here in Equation 5.1 shows that the surface potential of a ferroelectric is linked to both the surface charge,  $\rho$ , which is a balance between positive and negative charge carriers and acceptors/donors, Equation 2.2, and the remnant polarisation,  $P_r$ .

$$\nabla^2 V = -\frac{1}{\epsilon_o \epsilon_r} (\rho - \nabla P_r)$$

**Equation 5.1**

From Equation 5.1 it can be seen that under equilibrium conditions, i.e. no irradiation, the  $C^+$  domain has  $P_r > \rho$  so that the surface charge does not fully neutralise the remnant polarisation, the surface potential,  $V$ , will be positive. Therefore on this surface the inner Helmholtz plane will consist of strongly attracted counterions of opposite polarity, here negative anions. Thus with the PZT immersed in  $\text{AgNO}_3$  solution the domain has a

layer of desolvated nitrate ions and polarised water molecules across it, Figure 5.6 (A). This layer, which is *ca* 0.189 nm thick (the radius of the nitrate ion (Ariza and Otero, 2007)), acts as a barrier between the PZT  $C^+$  surface and the  $Ag^+$  cations in the outer Helmholtz and diffusion regions. If there is an interruption to the inner Helmholtz plane, i.e. a disturbance to the anion layer, it is possible that a nucleation site will occur as the cations have access the PZT surface as illustrated in Figure 5.6 below. This disturbance can occur where there is a variation in surface morphology which affects the surface potential.

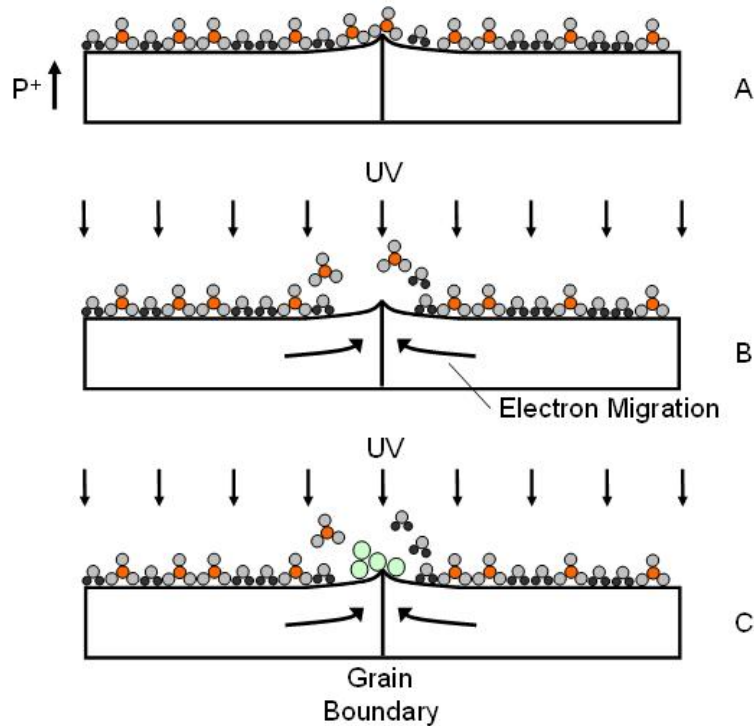


**Figure 5.6 Stern layer disturbance due to a PZT surface anomaly and cluster nucleation. (A) Under equilibrium conditions, i.e. no photoexcitation, the inner Helmholtz layer, consisting of  $NO_3^-$  anions, acts as a barrier to the  $Ag^+$  cations. (B) Upon UV illumination migrating photoexcited electrons cause a change in the local surface potential of the anomaly. (C)  $Ag^+$  cations are attracted to the anomaly surface and reduce forming the initial nucleation point.**

In Figure 5.6 (A) the inner Helmholtz plane consisting of negative nitrate anions covers the surface of the  $C^+$  domain stopping the positive  $Ag^+$  cations from reaching the PZT

surface. Upon illumination with super bandgap UV (B) photoexcited electrons migrate to the surface due to the  $C^+$  domain polarisation and to particular areas due to the electric fields generated by surface anomalies such as grain boundaries and defects. At the surface of these anomalies the migrating electrons accumulate and cause a localised change in the surface potential, i.e.  $P_r < p$  and the potential becomes negative, thus repelling the adsorbed nitrate anions. The negative surface potential also acts to attract the  $Ag^+$  ions from the outer Helmholtz plane and diffusion region (C) which then accept the electrons from the PZT and reduce to their metallic form on the surface.

The growth of individual clusters on the surface can be explained by the fact that, as well as the surface charge, the morphology and stoichiometry of the grain boundary has an effect on the surface potential (Kim *et al.*, 2007; Hagenbeck, 2001). As the morphology, both in and out of plane, of the grain boundary varies along its length so does the potential as illustrated in Figure 5.7.

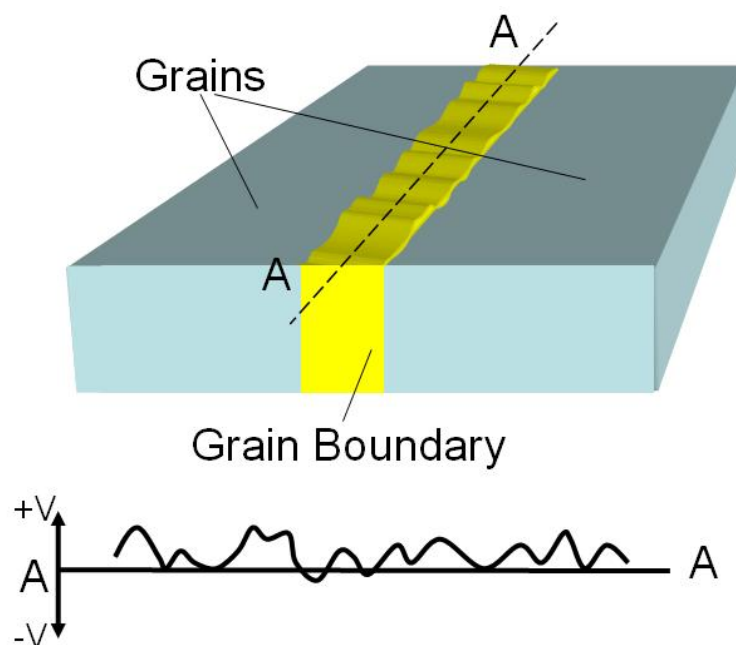


**Figure 5.7** Simplified illustration of surface potential along a grain boundary. The variations in stoichiometry and surface morphology of the grain boundary (Top) affect the surface potential along its axis A-A (Bottom).

During illumination as electrons migrate to the boundary they move to the point of highest potential, i.e. the peaks in surface potential, along the axis of the grain boundary or other surface defects. At lower photon energy there are fewer electrons available due to the DoS of the material. As these electrons move to the highest potential, the lower potential areas do not vary in surface charge and so no nucleation occurs there. The local accumulation of charge in the higher potential regions causes the disturbance in the inner Helmholtz layer as described above and nucleation occurs. As the photon energy increases more electrons are available to migrate to the boundary, these have the effect of countering the local potential high points along the surface and as more carriers are excited they accumulate.

Once the nucleation point has formed the cluster will continue to grow as photoexcited electrons migrate to it. Electrons that pass to the forming cluster move into it and distribute around its outer surface giving the cluster a negative surface potential, Figure 4.3, and attracting more  $\text{Ag}^+$  cations from solution. The cluster continues to grow outwards disrupting the Stern layer on the PZT surface adjacent to it, allowing more migrating electrons to enter until it has reached a point where the PZT surface is sufficiently shadowed and migration and thus growth stops. If left to grow to saturation across the PZT surface the final cluster size is dependent on the free space around, as it will grow to fill this area, and its individual rate of growth. If the cluster is not allowed to grow to its full extent, i.e. the irradiation is stopped before surface saturation is reached, as can be seen particularly in Figure 5.2 for the lower photon energy, the final size is then dependent on time of irradiation and the flux of photoexcited electrons to the surface due to the incident photons.

There is in fact a spread of cluster sizes across the surface due to the variation in surface potential across it. As an example, Figure 5.8 shows how cluster sizes can vary across the PZT surface when it is irradiated by wideband UV, though not the same irradiation technique as used in the rest of this section it gives an idea of the variation that occurs across clusters.

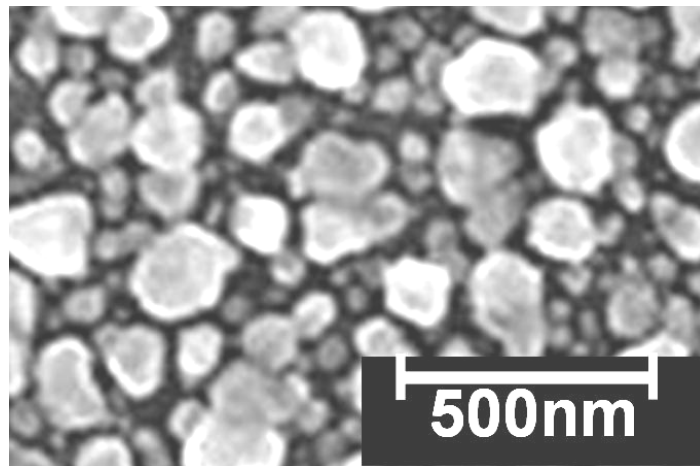


**Figure 5.8** PZT surface after 30 minute irradiation with H-lamp wideband UV, it can be seen that the clusters vary in size.

The variation in cluster size is dependent on the nature of the initial nucleation point, some will have a greater influence on the region around them, either by their size or structure. This means that some of the nucleation points will have the opportunity of grabbing more electrons from the surrounding area and thus these will grow as larger clusters.

The DoS for the PZT and the recombination rate of the photoexcited charge carriers all play a role in the rate of cluster growth. Once the impinging photons have energy over the bandgap they excite the electrons into the conduction band and photoreduction of the Ag can begin. The DoS near the band edge is relatively low, as shown in Figure 2.24, and so the supply of electrons is limited. This leads to a slower growth in the Ag

clusters as the ratio of carrier recombination to excitation is low. As the photon energy increases so electrons from deeper in the valence band are excited and so more migrate to the surface, the ratio of excited carriers to those recombining is higher and thus the rate of cluster growth is increased. The steady increase in cluster growth up to 4.8 eV shows that the DoS does not greatly increase below this energy, once this threshold is exceeded there is an increase in available energy states in the DOS thus increasing the number of available carriers. These results thus confirm the general shape of the plot by Silva *et al.* (2005) if not giving quantitative information about it.

Again it is interesting to contrast the above results to those of Lei *et al.* (2004), as shown in Figure 5.9. Initially the same trend is observed for lower energy photons, i.e. the cluster size and surface density increase with increasing energy. The results start to diverge when higher energy photons are used. In this work both cluster size and density continue to increase with energy until the cut off point at 5.1 eV, due to AgNO<sub>3</sub> solution absorbance, where no deposition occurs. In Lei's work the cluster size and density experience a decrease between 4.1 and 4.7 eV at which point it starts to increase again. Lei gives no explanation for this effect, though differences in experimental set-up could possibly affect results there is not enough data to form a theory.



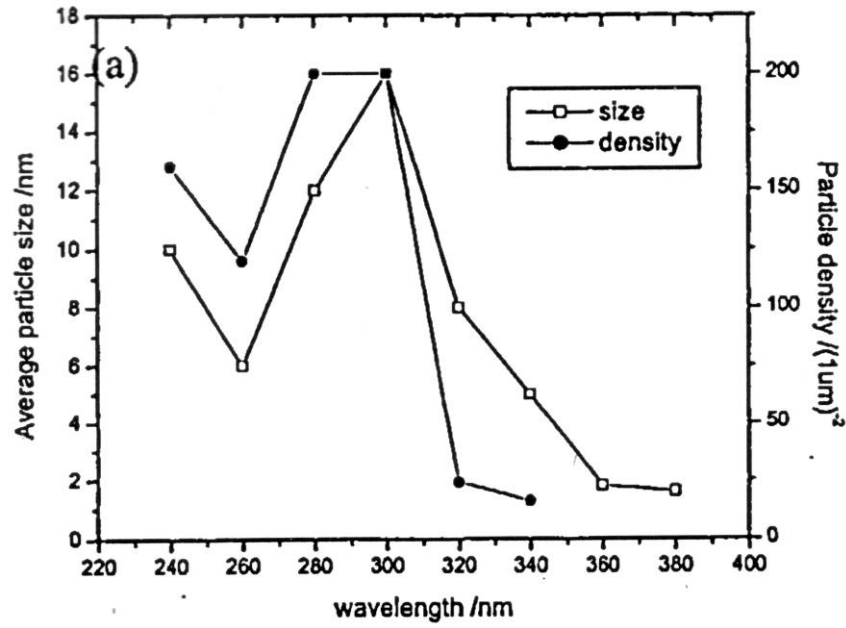


Figure 5.9 Wavelength dependence of silver deposition on PZT as presented by Lei *et al.* (2004).

This chapter has shown the effect of photon energy on the growth of  $\text{Ag}^0$  on the surface of PZT. It has illustrated how the Stern layer that forms on the solid/salt solution interface must be breached in order for initial cluster nucleation. The process of electron migration in  $\text{C}^+$  domains due to variations in the surface potential along grain boundaries were shown to be the areas where nucleation occurred and that it is the migration of electrons to the surface at these points that cause the Stern layer breach.

## 6 Reduction potential and band structure

The work presented so far has concentrated on the reduction of Ag onto PZT surfaces in order to study the effects of the physical film structure on deposition. In this chapter the REDOX reactions taking place at the surface and the position of metal salt reduction potential with regard to the band structure of the films will be discussed. In particular salts were selected for their cation reduction potential position with respect to the bandgap and bottom of the conduction band of the [111] orientated PZT.

### 6.1 Salt selection

It is known that the reduction potential position of ions in an electrolyte solution relative to a semiconductor's bandgap will affect how a REDOX reaction will occur between the ions and semiconductor surface (Zhu, 1994). A knowledge of the reduction potentials gives a means of finding which metal salts will reduce on or oxidise on a ferroelectric surface, it can also be used as a method of estimating the approximate location of the bottom of the conduction band at the surface of the PZT by studying the surface effects due to different salts. Scott (1999) has given the electron affinity,  $\chi$ , which is the bottom of the conduction band, for PZT as  $3.5 \pm 0.2$  eV and Pandey *et al.* (2005) as 3.4 eV. The band bending for PZT has also been given by Scott as  $0.5 \pm 0.1$  eV, though as shown in section 4.5 on the effects of orientation, it is shown bending is actually dependent on the orientation of the films used. It can be seen in Table 6.1 and Figure 6.1 that the salts chosen for this work were selected for their positions relative to the conduction band given by Scott. In selecting these salts it made it possible to both find the position of the conduction band at the PZT surface experimentally and also to

study the effects of salts with cation reduction potentials both inside and out of the bandgap.

**Table 6.1 Standard reduction potentials for metal salts used (Atkins, 2006)**

(Standard temperature and pressure)

Formula	Cation	SRP (V)
AgNO <sub>3</sub>	Ag <sup>+</sup>	+0.79
CuCl <sub>2</sub>	Cu <sup>2+</sup>	+0.34
SnCl <sub>2</sub>	Sn <sup>2+</sup>	-0.14
FeCl <sub>2</sub>	Fe <sup>2+</sup>	-0.44
ZnCl <sub>2</sub>	Zn <sup>2+</sup>	-0.76
Zn(NO <sub>3</sub> ) <sub>2</sub>	Zn <sup>2+</sup>	-0.76
Mn(NO <sub>3</sub> ) <sub>2</sub>	Mn <sup>2+</sup>	-1.18
AlCl <sub>3</sub>	Al <sup>3+</sup>	-1.66

From the experimental work it was found that three possible surface reactions could take place dependent on the cation's position relative to the bandgap and whether the salt was a nitrate or chloride. These scenarios are listed below;

1. Nitrate or chloride salts with cation reduction potentials within the bandgap showed metal deposition on C<sup>+</sup> domains and no effects on the C<sup>-</sup> domains.
2. Nitrate salts with cation reduction potentials above the conduction band showed no surface effects either on the C<sup>+</sup> or C<sup>-</sup> domains.
3. Chloride salts with cation reduction potentials above the conduction band caused decomposition of the C<sup>-</sup> domain while the C<sup>+</sup> remained unaffected.

These scenarios are discussed in the following sections.

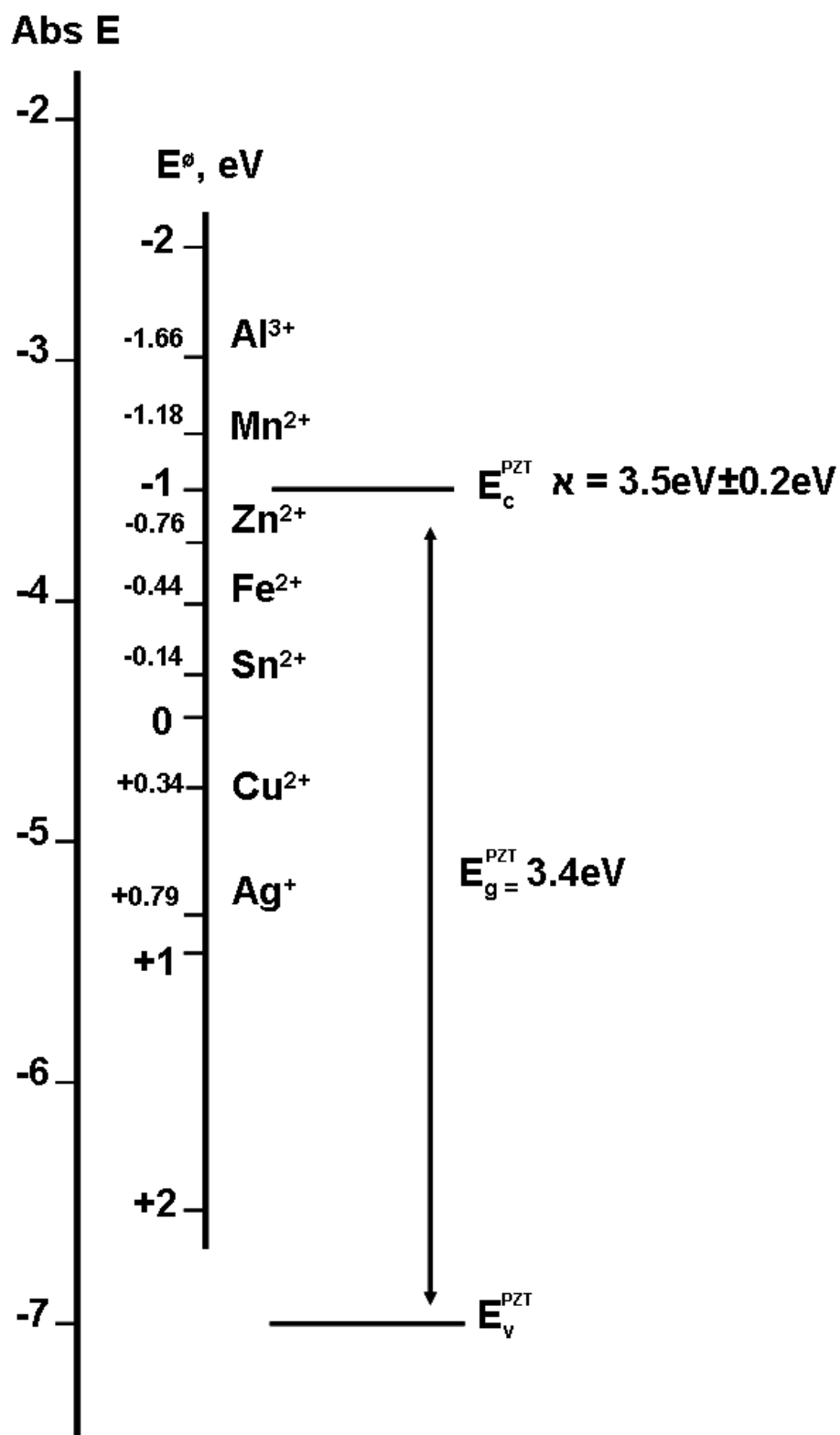
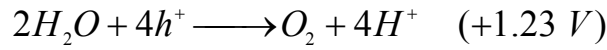


Figure 6.1 Standard hydrogen potential,  $E^{\circ}$ , against absolute energy (Trasatti, 1986) displaying reduction potentials of the salts used with respect to the PZT band edges. PZT band edge values taken from Scott (1999).

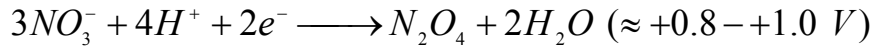
## 6.2 Salts within PZT bandgap

As seen in previous chapters, scenario 1 occurs when the  $\text{Ag}^+$  cation in  $\text{AgNO}_3$  reduce to metallic  $\text{Ag}^0$  on the  $\text{C}^+$  domains of the PZT during UV illumination on PZT[111] films. The reduction potential for  $\text{Ag}^+$  is +0.79 eV which, as shown in Figure 6.1, is well within the bandgap for PZT. Photoexcited electrons in the film can therefore drop from the conduction band to the  $\text{Ag}^+$  cation at the PZT surface and reduce it. On the  $\text{C}^-$  domains where holes are migrating to the surface it is believed that the breakdown of water occurs, Equation 6.1.

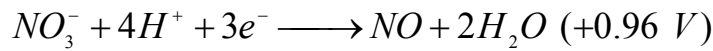


**Equation 6.1**

Two other reactions involving the nitrate ions shown in Equation 6.2 and Equation 6.3 could also occur on the  $\text{C}^+$  domains in competition with the  $\text{Ag}^+$  reduction. The rates of which are dependent on the kinetics of the various reactions, which in turn are dependent on the concentration of each species at the PZT surface and order of preference of the individual reactions, i.e. which is more favourable.



**Equation 6.2**



**Equation 6.3**

The process taking place in Equation 6.1 will release 4 electrons into the  $\text{C}^-$  domain, the processes shown in Equation 6.2 and Equation 6.3 require 2 and 3 electrons respectively, which means that there will be from 1 to 2 electrons available for the reduction of  $\text{Ag}^+$  on the  $\text{C}^+$  domain.

As with the  $\text{AgNO}_3$  when the  $\text{SnCl}_2$  solution was used, the cation of which is also within the bandgap of the PZT, metallic Sn was found to reduce onto the  $\text{C}^+$  domain as shown in Figure 6.2.

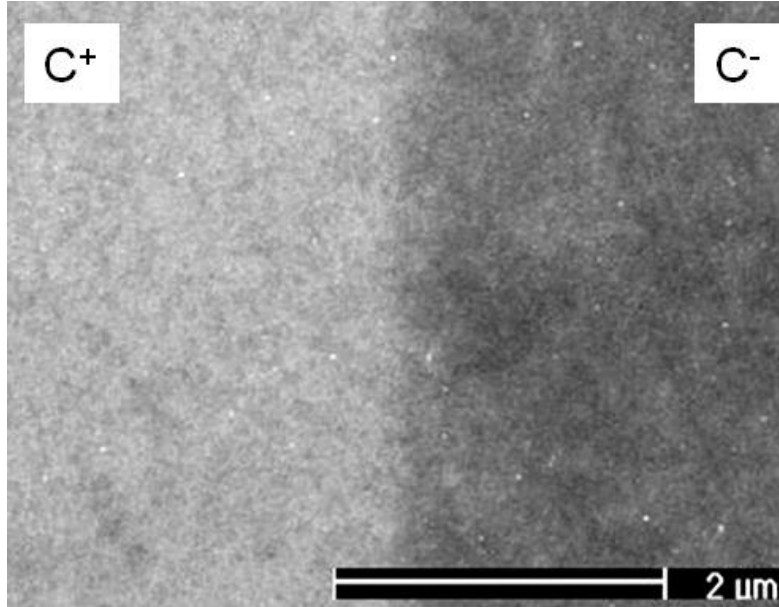


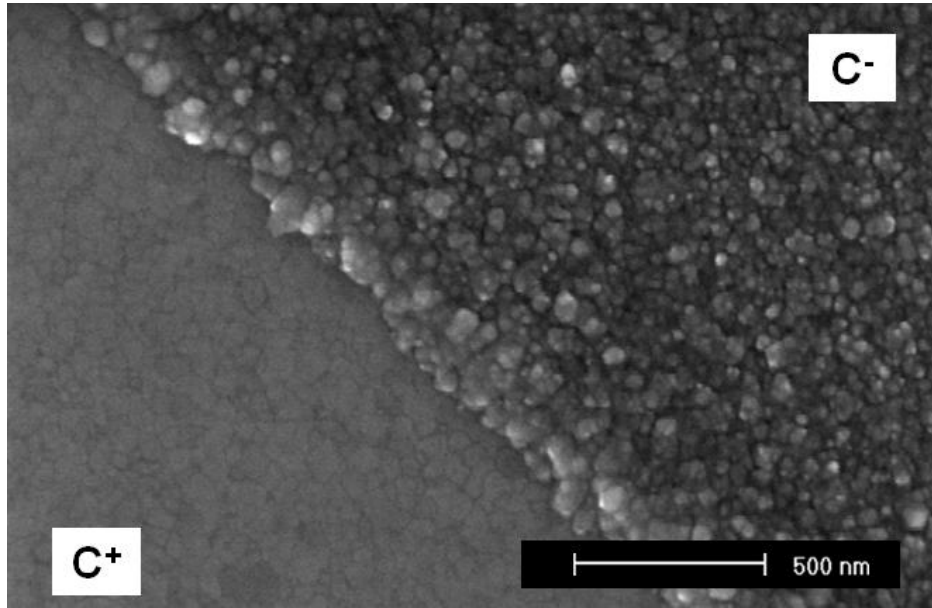
**Figure 6.2**  $\text{Sn}^0$  reduced onto the  $\text{C}^+$  domains on PZT[111] film after irradiation with the H-lamp.

Again, due to its position within the bandgap, the same electron to ion exchange process takes place as previously described for  $\text{AgNO}_3$ . It should be noted that the  $\text{Sn}^{2+}$  has reduced on the  $\text{C}^+$  domain as a fine layer where individual clusters are too small to be seen, as opposed to the Ag which has grown as visible clusters on the surface. The cause of this variation is not fully understood but could be partly due to the competitive processes stated above for the  $\text{NO}_3^-$  and  $\text{Ag}^+$  ions on the  $\text{C}^+$  domains.

### ***6.3 Chlorides and nitrates with cation reduction potential above conduction band***

For metal salts with cation reduction potentials above the conduction band different effects were observed depending on whether the salt was a chloride or a nitrate. For chloride salts scenario 3 occurred where there was no deposition of metal on the  $\text{C}^+$

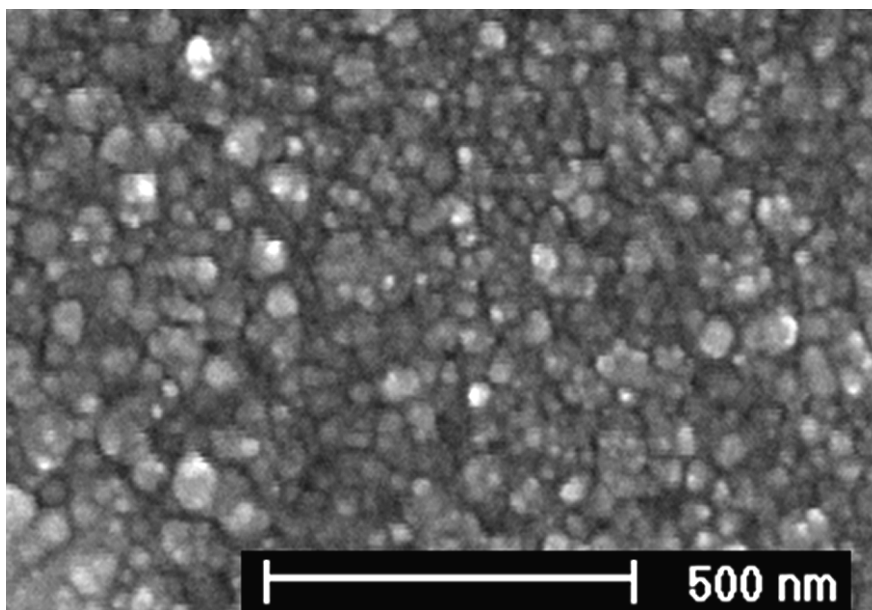
domain but the  $C^-$  domain was decomposed as was found when  $AlCl_3$  solution was used. Figure 6.3 shows the result for  $AlCl_3$  solution.



**Figure 6.3 SEM image of PZT where the  $C^-$  domain shows signs of photocorrosion by the  $FeCl_2$  solution.**

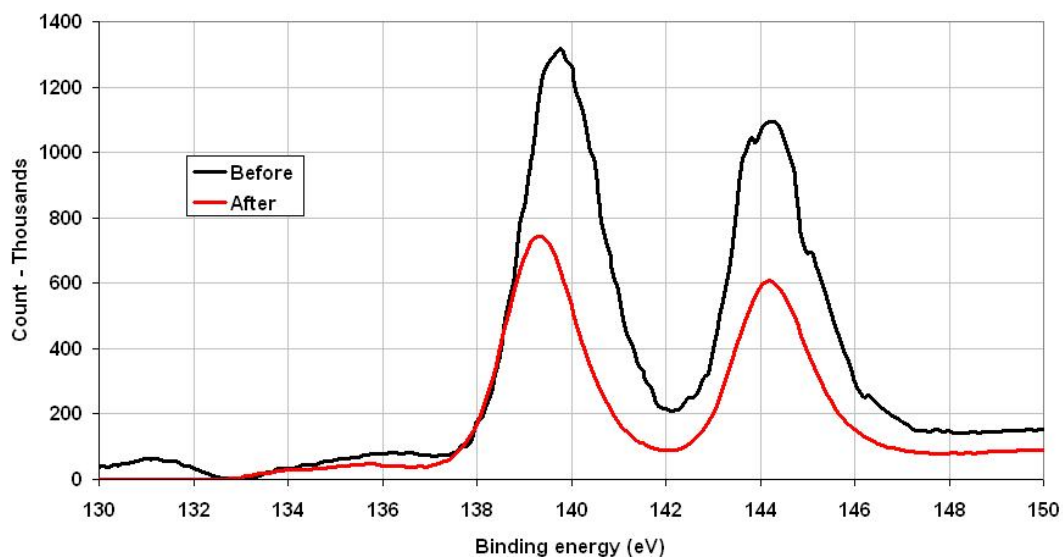
Here the  $Al^{3+}$  cation reduction potential sit well above the conduction band for the PZT as can be seen in Figure 6.1. This means that electrons excited into the conduction band in  $C^+$  domains during irradiation will not reduce them to their metallic forms. Also due to their trivalent and divalent natures the cations are strongly repelled from the  $C^+$  domain, though they are attracted to the  $C^-$  where they displace the  $H_2O$  molecules due to their higher charge and strongly adhere to it (Dunn *et al.*, 2004). On the  $C^-$  domain as electrons do not migrate to the surface no reduction of the cations occurs.

Figure 6.4 shows an enlarged image of the corrosion that has taken place on the  $C^-$  domain due to the  $AlCl_3$  solution. The major loss of material can be seen to have occurred around the edges of the grain boundaries giving the surface a granular texture.



**Figure 6.4** High magnification SEM image of PZT[111] C domain showing photocorrosion by  $\text{FeCl}_2$  solution.

An XPS of the domain before and after irradiation, Figure 6.5, shows that Pb is the main material of loss in this decomposition process, while there is very little change in the Ti and Zr content.



**Figure 6.5** XPS results for Pb in PZT[111] sample before and after UV irradiation in 0.01M  $\text{AlCl}_3$  solution. It shows that there is a reduction in Pb content after irradiation has taken place.



A variation of this effect was observed when the  $\text{FeCl}_2$  solution was used, as it was found that for some samples the  $\text{C}^-$  domains decomposed, Figure 6.6, while others showed metal deposition on the  $\text{C}^+$ , Figure 6.7.

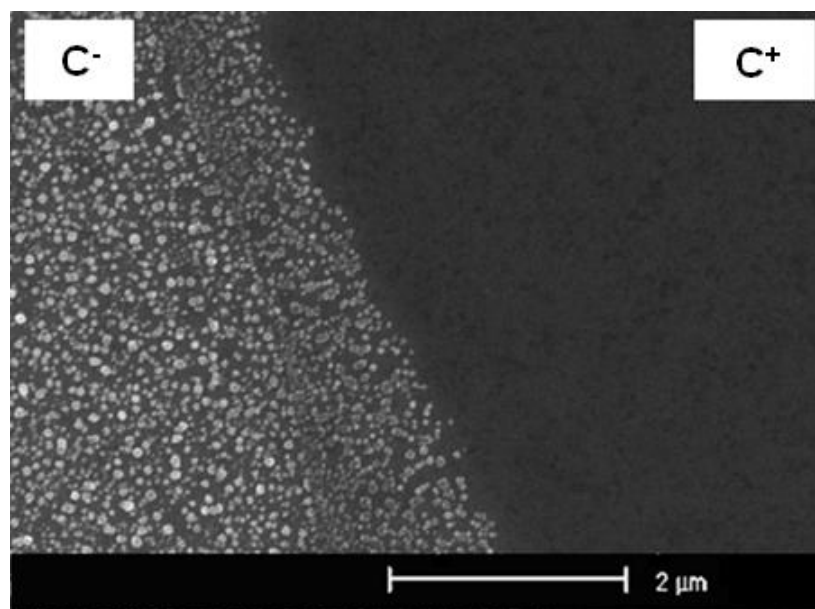


**Figure 6.6 SEM image of PZT where the  $\text{C}^-$  domain shows signs of photocorrosion by  $\text{FeCl}_2$  solution.**

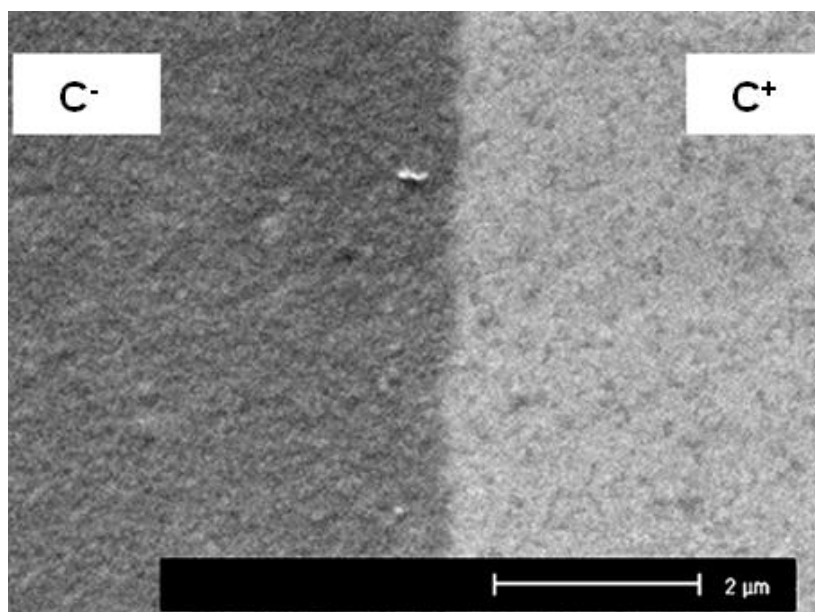


**Figure 6.7 SEM image of Fe deposited on  $\text{C}^+$  domain from  $\text{FeCl}_2$  solution.**

Figure 6.1 shows that according to the band structure as stated by Scott, the  $\text{Fe}^{2+}$  ion sits just below the conduction band and therefore should reduce onto  $\text{C}^+$  domains. The samples were made using the same sol and equipment, therefore the difference between the samples must be due to a variation in the processing stages. For example, though the hotplate temperature was monitored during the pyrolysing and annealing steps of film synthesis there can be a temperature variation across its surface. If the samples are placed at different locations on the hotplate they will be subject to slight variations in temperature, even across one sample wafer. This suggests that slight differences in film processing can have an impact on the band structure of the PZT, perhaps through the surface defect structure due to oxygen vacancies, trap states and surface charge. If this is taken into account then the fact that some of the samples give  $\text{C}^+$  domain reduction while others have decomposition on the  $\text{C}^-$  can be explained by the positions of the energy bands at the surface being at different levels for the samples. If the  $\text{Fe}^{2+}$  ion is just at the cusp of this uncertainty zone, Figure 6.8, then the variation would give the above results.

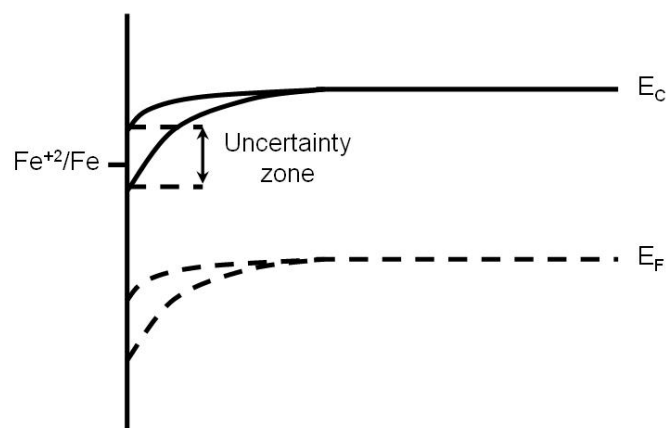


**Figure 6.8** Location of the reduction potential of  $\text{Fe}^{2+}$  with respect to the conduction band in PZT showing an uncertainty region in the location of the conduction band edge at the surface. The actual position of this edge with respect to the  $\text{Fe}^{2+}$  ion will result in either metal reduction, band above ion, or corrosion, band below ion.

It is possible to use the reduction potentials of both the  $\text{Sn}^{2+}$  and  $\text{Fe}^{2+}$  cations and look at the resultant surface effects after irradiation to say that the conduction band at the PZT[111] surface after band bending occurs in a range between 4.06 eV and 4.36 eV from vacuum. This is slightly different to Scott's values of  $3.5 \text{ eV} + 0.5 \text{ eV} = 4 \text{ eV}$  (Conduction band absolute position + Band bending) though as already shown in the previous chapter on film stoichiometry, and in this section the processing characteristics can have an impact on the band structure of the films. It is interesting to note that when nitrate forms of the salts with reduction potentials above the conduction band were used, such as  $\text{Zn}(\text{NO}_3)_2$ , no deposition was observed on the  $\text{C}^+$  domains and no decomposition occurred on the  $\text{C}^-$ .

As seen above, chloride salts with cation reduction potentials within the bandgap,  $\text{SnCl}_2$ , give metal deposition on  $\text{C}^+$  domains and no observable degradation of the  $\text{C}^-$ , Figure 6.2. This means that when the chlorides are used the reduction of the cation onto the  $\text{C}^+$  domain is protecting the  $\text{C}^-$  from degradation i.e. there is an interaction between the migration of electrons to the positive surface and holes to the negative. This interaction is the REDOX cycle where the charge carriers in each domain and the ions in solution each complete one half of the reaction. It has also been seen, Figure 6.3, that if the cation reduction potential is above the conduction band  $\text{C}^-$  domain corrosion occurs, this is due to REDOX cycle changes where the ions of the solid surface itself take part in the reaction.

The decomposition of  $\text{C}^-$  domains is due to the following reasons. The migration of holes to the surface in  $\text{C}^-$  domains during irradiation causes a weakening of the surface bonds (Pleskov and Gurevich, 1986). For PZT the valence band where the holes are formed is made up of the oxygen 2p bonds (Silva *et al.*, 2005), therefore the bonds most

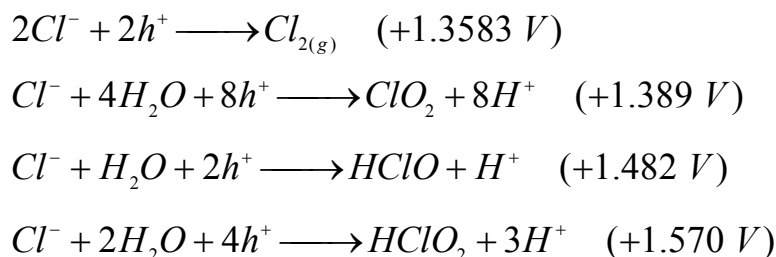
influenced by hole migration are the oxygen 2p. It has been suggested that PZT can be thought of as being made up of three separate compounds, PbO, ZrO<sub>2</sub> and TiO<sub>2</sub> (Zheng *et al.*, 2004). This may possibly be true for amorphous PZT but cannot be if in the perovskite form as each of the ions is actually part of a greater polycrystalline structure. This means that the displacement of ions from the surface during photodecomposition is related to the relative bond strength of each species in the crystal lattice. A qualitative ranking for the relative bond strengths can be made by studying the electronegativities of the ions. For the components in PZT O, Pb, Ti and Zr the electronegativities are 3.44, 2.33, 1.54 and 1.33 respectively. Of these the greatest difference is between the O and Ti, Zr ions, meaning that the strongest bonds belong to the Ti-O<sub>n</sub> and Zr-O<sub>n</sub> bonds and the weakest is the Pb-O<sub>n</sub> bonds. Also as Pb is volatile it is used in excess in the sol during film production in order to keep stoichiometric balance. This excess Pb tends to migrate to grain boundaries during the high temperature annealing stage of the process, and so these areas tend to have a greater amount of PbO<sub>n</sub> in them (Huang *et al.*, 1998). This explains why there is greater decomposition found around the grain boundaries in the C<sup>-</sup> domains, Figure 6.4.

While the description above explains why Pb is preferentially removed from the PZT surface rather than Ti or Zr, it does not show why chloride salts cause decomposition of the film and nitrates do not. In order to do this it is necessary to understand that chloride and nitrate ions in solution have different electrochemical properties and that they both have reduction potentials within bandgap of PZT.

For nitrate salts with cations that are above the conduction band, such as the Zn(NO<sub>3</sub>)<sub>2</sub>, it is possible that the nitrate anion is reduced on the C<sup>+</sup> domain by the photoexcited electrons as in Equation 6.2 and Equation 6.3 both reactions of which will compete

dependent on process kinetics. The other half of the REDOX cycle would then involve the oxidation of H<sub>2</sub>O on the C<sup>-</sup> domain and the release of H<sup>+</sup>, Equation 6.1, which takes part in the nitrate reduction.

Chlorine ions, due to their reduction potential position, will only take part in oxidation reactions on the C<sup>-</sup> domain, the possible reactions being shown in Equation 6.4.



**Equation 6.4**

But as the oxidation of H<sub>2</sub>O is more favourable, Equation 6.1, these reactions are probably not responsible for the decomposition of the C<sup>-</sup> domains. It is therefore hypothesised that the actual process of decomposition involves a solution mobile intermediate species, R. The nature of this species is unclear at present but would be formed on the C<sup>+</sup> domain and thus uses the photoexcited electrons and is one half of the REDOX reaction cycle. The PbO<sub>n</sub> bonds in the surface of the C<sup>-</sup> domain weakened by the photogeneration of holes form Pb<sup>n+</sup> ions which are susceptible to bonding with R in solution. The Pb<sup>n+</sup> ions then form PbCl<sub>2</sub> and go into suspension. This process also explains the protection of the C<sup>-</sup> domain when cation reduction potentials are within the bandgap, such as SnCl<sub>2</sub>, as the intermediate species would form a metallic layer which adheres to the C<sup>+</sup> domain and so does not interact with C<sup>-</sup> domain.

## **6.4 Oxidation on negative domains**

Along with the three scenarios described above there was a fourth that was observed when Mn(NO<sub>3</sub>)<sub>2</sub> and MnCl<sub>2</sub> salts were used. As the Mn cation is above the conduction

band, it cannot be reduced onto the  $C^+$  domains. Therefore if scenarios 2 and 3 were applied it would be expected that the Mn salts would either decompose the  $C^-$  domains when in the chloride form or have no surface effects when in the nitrate form. In fact neither of these were observed and instead a highly porous layer formed on the  $C^-$  domains Figure 6.9. EDX shows that this layer is in fact an oxide of Mn.

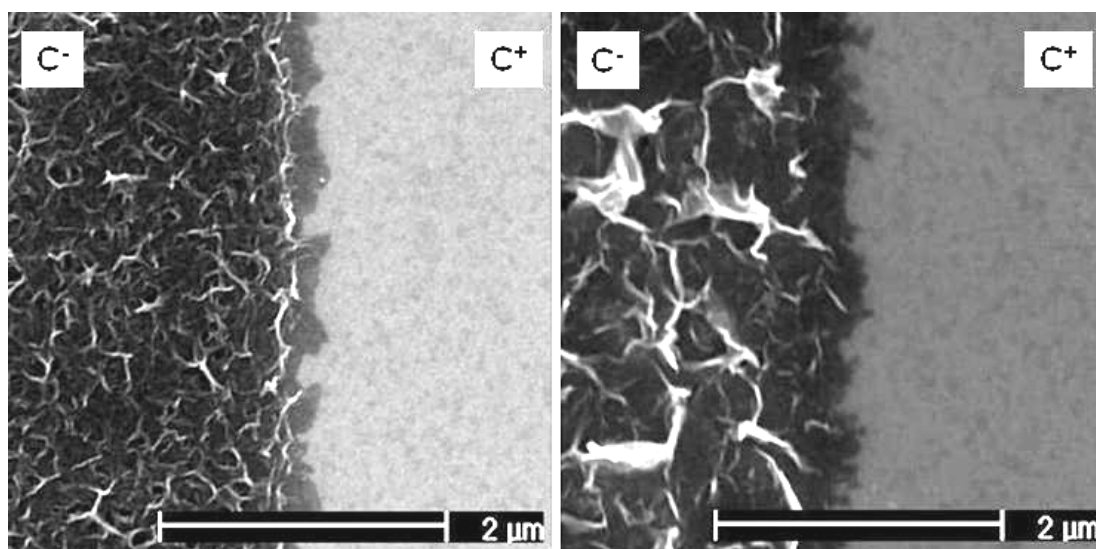


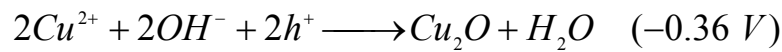
**Figure 6.9 SEM image of Mn oxide on  $C^-$  domains of PZT[111] samples using (Left)  $Mn(NO_3)_2$  salts and (Right)  $MnCl_2$  salts.**

The exact reason for the oxidation of the  $Mn^{2+}$  cation on the  $C^-$  domain is not understood but could be due to the fact that its oxidation potential is +1.23 V which is within the bandgap of the PZT. Holes from the  $C^-$  domain can thus interact with the cation, the exact oxidation state of the deposited film is unknown at present.

At the  $C^+$  domain surface the anions  $Cl^-$  or  $NO_3^-$  will reduce in competition with the  $H_2O$ . This could explain why the oxide films for the two Mn salts have a different structure, as the  $Cl^-/H_2O$  and  $NO_3^-/H_2O$  processes will compete at different rates due to the relative chemical kinetics. This oxidation process has also been observed by various

groups with Pb on BaTiO<sub>3</sub> (Giocondi *et al.*, 2003) and TiO<sub>2</sub> (Tanaka *et al.*, 1986; Torres and Cervera, 1992).

Another interesting result was obtained for CuCl<sub>2</sub> where reduction of the Cu<sup>2+</sup> cation was observed, Figure 6.10. This reaction is shown in Equation 6.5. The growth was on the C<sup>-</sup> domain but differed structurally, where as the Mn had grown into a porous sponge like structure the Cu had a granular texture. Also noticeable across the whole of the PZT surface, C<sup>+</sup> and C<sup>-</sup> domains were clusters that EDX showed to be Cu. It is probable that these formed in solution during irradiation and upon reaching a certain size adhered to the PZT surface by electrostatic attraction.



Equation 6.5

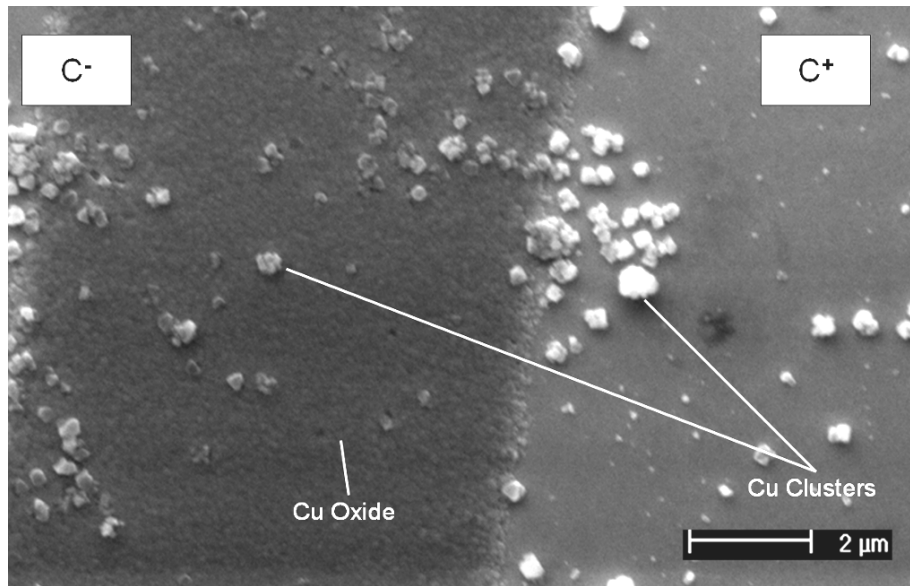


**Figure 6.10** Cu oxide formed on C<sup>-</sup> domain from CuCl<sub>2</sub> solution, larger objects are Cu clusters across most of the surface.

This chapter has developed the link between the cation reduction potential of a salt and its relative position to the conduction band of PZT. It has shown that for a metal ion to reduce onto the C<sup>+</sup> domain it must have a reduction potential within the bandgap, if it is above then either oxidation of the ion or decomposition of the PZT C<sup>-</sup> domain can

occur. The oxidation of ions or decomposition of the  $C^-$  domain were shown to be dependent on whether the salt is a chloride or nitrate, the chloride form causing decomposition and the nitrate causing oxidation. The reduction/decomposition process was used to locate the position of the bottom of the conduction band at the PZT surface. The ability of  $FeCl_2$  to decompose some PZT samples and not others meant that it sat very close to the conduction band, this level being found to be between 4.06 eV and 4.36 eV from vacuum.



## **7 Conclusions and Future work**

### **7.1 Conclusions**

This work has shown that there are many complex interactions taking place between the surface interface of a ferroelectric and a metal salt solution under ultraviolet irradiation. It has been found that factors such as surface morphology and production methodology of the PZT film and the characteristics of the irradiating photons all have a significant effect on these interactions.

The work has confirmed that, as with previous studies, it is possible to grow metals such as silver onto the positive domains of a ferroelectric such as PZT, but that this deposition is in fact greatly influenced by film structure. It was found that the majority of metal cluster growth occurred at grain boundaries with a 51:1 growth rate compared to the grain itself. It was also shown that if [100] oriented PZT was used rather than [111] the metal clusters could also form on negative domains given enough photon energy and flux. This variation was explained by the alteration of the bending of the energy bands at the PZT surface and the effect of surface charge magnitude for each orientation, and how this affected the depth of the space charge region that forms at the interface. The [100] film having a narrower space charge region than the [111] had a higher probability of electron tunnelling to the surface of the negative domains and thus allowed cluster growth at these points.

The energy and flux of photons incident to the surface of the film was observed to play a part in the rate of cluster growth across the PZT surface. Increasing photon energy directly led to an increase in cluster size which was explained using the density of states of the PZT and the number of excited charge carriers generated and their migration to surface potential peaks. As photons of greater energy interacted with the film so

electrons deeper in the energy bands were excited. Lower energy photons, above the band gap, excited fewer carriers as there were fewer available for excitation, deeper in to the energy bands the density of states increased and more carriers were available for excitation. The greater flux of carriers to the surface then directly affected the cluster growth rate.

The link between the reduction potential of the cation in the salt solutions and the position of the bandgap and bottom of the conduction band for the PZT were developed. It was shown that for a metal to reduce onto the  $C^+$  domains its reduction potential needed to be within the bandgap of the material. It was also found that if the cation reduction potential was above the bottom of the conduction band then either oxidation of the cation onto the negative domain or decomposition of the negative domain occurred. These two effects were shown to depend on the type of anion in the salt, chlorine was found to cause decomposition whereas with nitrates the cation was found to oxidise. These effects were linked to the movement of electrons to the  $C^+$  domain and thus reduction of the cation and the migration of holes to the  $C^-$  giving oxidation of the cation. When decomposition occurred the migration of holes to the  $C^-$  domain was also believed to weaken the bonds of the lead ions which lead to corrosion with chlorine.

## **7.2 Future work**

The work that has been undertaken here has shown the complex nature of the interactions taking place at the PZT salt solution interface. It has also revealed other areas that would benefit from further investigation and allow an even greater understanding of these interactions, these include:

- Photocurrent and photoexcited electron yield. This would indicate the number of carriers that can be generated in the PZT film and also the conversion efficiency during photon electron excitation. From this information it would be possible to estimate the overall efficiency of photon to metal ion reduction.
- Flat band potential measurements. It is important to have an accurate measurement of the flat band potential of the PZT film as it allows for a better idea of the amount of band bending that is occurring at the PZT surface. It can also be used to confirm if the surface of the PZT is acting as either a p- or n-type semiconductor.
- Further in-depth study of the PZT surface defect structure. This would involve creating films with different densities of surface defects such as oxygen vacancies. This would in turn give a better understanding of how the defects affect metal growth rate and final size.
- PZT doping tests to see what effect doping of the PZT would have on the rate of cluster growth and morphology.

## 8 REFERENCES

- Abrams, B. L. and Wilcoxon, J. P. (2005), "Nanosize semiconductors for photooxidation", *Critical Reviews in Solid State and Materials Sciences*, vol. 30, pp. 153-182.
- Ariza, M. J. and Otero, T. F. (2007), "Nitrate and chloride transport through a smart membrane", *Journal of Membrane Science*, vol. 290, no. 1-2, pp. 241-249.
- Atkins, P. and de Paula, J. (2006), 7.8 Standard potential., *Physical Chemistry*, 8th ed. Oxford: Oxford university press pp. 222-223.
- Azzazy, H. M. E., Mansour, M. M. H. and Kazmierczak, S. C. (2006), "Nanodiagnosics: A new frontier for clinical laboratory medicine", *Clinical Chemistry*, vol. 52, no. 7, pp. 1238-1246.
- Bardeen, J., ( 1994), *A Biographical Memoir of Walter houser Brattain 1902—1987*, National Academy of Sciences.
- Bertoni, C., Gallardo, D., Dunn, S., Gaponik, N. and Eychmüller, A. (2007), "Fabrication and characterization of red-emitting electroluminescent devices based on thiol-stabilized semiconductor nanocrystals", *Applied Physics Letters*, vol. 90, no. 3. pp. 034107-034110
- Beydoun, D., Amal, R., Low, G. and McEvoy, S. (1999), "Role of nanoparticles in photocatalysis", *Journal of Nanoparticle Research*, vol. 1, pp. 439-458.
- Blatter, G. and Greuter, F. (1986a), "Carrier transport through grain boundaries in semiconductors", *Physical Review B*, vol. 33, no. 6, pp. 3952-3966.
- Blatter, G. and Greuter, F. (1986b), "Electrical breakdown at semiconductor grain boundaries", *Physical Review B*, vol. 34, no. 12, pp. 8555-8572.
- Boerasu, I., Pintilie, L., Pereira, M., Vasilevskiy, M. I. and Gomes, J. M. (2003), "Competition between ferroelectric and semiconductor properties in  $\text{Pb}(\text{Zr}_{0.65}\text{Ti}_{0.35})\text{O}_3$  thin films deposited by sol-gel", *Journal of Applied Physics*, vol. 93, no. 8, pp. 4776-4783.
- Bonnell, D. A. and Kalinin, S. V. (2002), "Local polarization, charge compensation and chemical interactions on ferroelectric surfaces: a route towards new nanostructures", *Ferroelectric thin films X*, Vol. 688, Boston, MA, Materials Research Society, pp. 317-328.
- Bonnell, D. A. and Kalinin, S. V. (2001), "Local potential at atomically abrupt oxide grain boundaries by scanning probe microscopy", *Solid State Phenomena*, vol. 80-81, pp. 33-44.
- Bube, R. H. (1967), "Photoconductivity processes", in *Photoconductivity in solids*, 2nd ed, Wiley and Sons Inc, , pp. 56-59.

- Butt, H. J., Graf, K. and Michael, K. (2006), *Physics and Chemistry of Interfaces*, Wiley-VCH.
- Byrne, J. A., Davidson, A., Dunlop, P. S. M. and Eggins, B. R. (2002), "Water treatment using nano-crystalline TiO<sub>2</sub> electrodes", *Journal of Photochemistry and Photobiology A: Chemistry*, vol. 148, no. 1-3, pp. 365-374.
- Card, H. C. (1977), "Electronic processes at grain boundaries in polycrystalline semiconductors under optical illumination", *IEEE Transactions on Electronic Devices*, vol. 24, no. 4, pp. 397-402.
- Chen, D. and Ray, A. (2001), "Removal of toxic metal ions from wastewater by semiconductor photocatalysis", *Chemical Engineering Science*, vol. 56, pp. 1561-1570.
- Chen, X., Lu, W. and Shen, S. C. (2004), "First-principles study of photoconductivity in BaTiO<sub>3</sub> with oxygen vacancies", *Solid State Communications*, vol. 130, no. 10, pp. 641-645.
- Cross, L. E. and Hardtl, K. H. (1984), "Ferroelectrics", in Grayson, M. (ed.) *Encyclopaedia of glass, ceramics, and cement*, 1st ed, Wiley, New York, pp. 409-439.
- Du, X. -, Belegundu, U. and Uchino, K. (1997), "Crystal orientation dependence of piezoelectric properties in lead zirconate titanate: Theoretical expectation for thin films", *Japanese Journal of Applied Physics, Part 1*, vol. 36, no. 9 A, pp. 5580-5587.
- Du, X. -, Zheng, J., Belegundu, U. and Uchino, K. (1998), "Crystal orientation dependence of piezoelectric properties of lead zirconate titanate near the morphotropic phase boundary", *Applied Physics Letters*, vol. 72, no. 19, pp. 2421-2423.
- Dunn, S., Cullen, D., Estefania, A. G., Bertoni, B., Carter, R., Howorth, D. and Whatmore, R. W. (2004), "Using the surface spontaneous depolarization field of ferroelectrics to direct the assembly of virus particles", *Applied Physics Letters*, vol. 85, no. 16, pp. 3537-3539.
- Dunn, S. and Sharp, S. (2008), "Photochemical growth of silver nanoparticles on semiconductor surfaces – initial nucleation stage", Awaiting publication in *Nanotechnology*.
- Dunn, S. and Whatmore, R. W. (2002), "Substrate effects on domain structures of PZT 30/70 sol-gel films via PiezoAFM", *Journal of the European Ceramic Society*, vol. 22, no. 6, pp. 825-833.
- Feynman, R. P., Leighton, R. B. and Sands, M. (1964), "Dielectrics", in *Feynman Lectures on Physics*, Addison Wesley, , pp. 10-3-10-5.

- Fraser, D. A. (1986), "Surfaces and interfaces", in *The Physics of Semiconductor Devices*, Clarendon Press, Oxford.
- French, A. P. and Taylor, E. F. (1998), "9-5 Barrier Penetration: Tunnelling", in *An Introduction to Quantum Physics*, CRC Press, pp. 383-386.
- Funakubo, H. (2005), "Spontaneous Polarization and Crystal Orientation Control of MOCVD PZT and Bi 4Ti 3O 12-Based Films", in *Ferroelectric Thin Films*, Springer, Berlin, pp. 77-91.
- Garrett, C. G. B. and Brattain, W. H. (1955), "Physical theory of semiconductor surfaces", *Physical Review*, vol. 99, no. 2, pp. 376-387.
- Giocondi, J. L. and Rohrer, G. S. (2001a), "Photochemical reduction and oxidation reactions on barium titanate surfaces", *Materials Research Society Symposium - Structure Property Relationships of Oxide Surfaces and Interfaces*, Vol. 654, Boston, MA, Materials Research Society, pp. AA7.4.1.
- Giocondi, J. L. and Rohrer, G. S. (2001b), "Spatial separation of photochemical oxidation and reduction reactions on the surface of ferroelectric BaTiO<sub>3</sub>", *The Journal of Physical Chemistry B*, vol. 105, no. 35, pp. 8275-8277.
- Giocondi, J. L. and Rohrer, G. S. (2001c), "Spatially selective photochemical reduction of Silver on the surface of ferroelectric Barium Titanate", *Chemistry of Materials*, vol. 13, no. 2, pp. 241-242.
- Giocondi, J. L., Samadzadeh, S. and Rohrer, G. S. (2003), "Orientation dependence of the photochemical reactivity of BaTiO<sub>3</sub>", *Solid-State Chemistry of Inorganic Materials IV*, Vol. 755, Boston, MA, Materials Research Society, pp. 315.
- Goodeve, C. F. and Kitchener, J. A. (1938), "Photosensitisation by titanium dioxide", *Transactions of the Faraday Society*, vol. 34, pp. 570-579.
- Grätzel, M. (2001), "Photoelectrochemical cells", *Nature*, vol. 414, pp. 338-344.
- Hagenbeck, R. (2001), "Electrical properties at grain boundaries in titanate ceramics", *Solid State Phenomena*, vol. 80-81, pp. 21-32.
- Hagenbeck, R., Schneider-Stormann, L., Vollmann, M. and Waser, R. (1996), "Numerical simulation of the defect chemistry and electrostatics at grain boundaries in titanate ceramics", *Materials Science and Engineering: B*, vol. 39, no. 3, pp. 179-187.
- Hanson, J. N., Rodriguez, B. J., Nemanich, R. J. and Gruverman, A. (2006), "Fabrication of metallic nanowires on a ferroelectric template via photochemical reaction", *Nanotechnology*, vol. 17, pp. 4946-4949.
- Hatton, G. D., Shortland, A. J. and Tite, M. S. "The production technology of Egyptian blue and green frits from second millennium BC Egypt and Mesopotamia", *Journal of Archaeological Science*, vol. In Press, Corrected Proof.

- Hotsenpiller, P. A., Bolt, J. D., Farneth, W. E., Lowekamp, J. B. and Rohrer, G. S. (1998), "Orientation dependence of photochemical reactions on TiO<sub>2</sub> surfaces", *Journal of Physical Chemistry B*, vol. 102, no. 17, pp. 3216-3226.
- Huang, Z., Zhang, Q. and Whatmore, R. W. (1998), "The Role of an Intermetallic Phase on the Crystallization of Lead Zirconate Titanate in Sol gel Process", *Journal of Materials Science Letters*, vol. V17, no. 14, pp. 1157-1159.
- Inoue, Y., Sato, K. and Sato, K. (1989), "Photovoltaic and photocatalytic behaviour of a ferroelectric semiconductor, lead strontium zirconate, with a polarisation axis perpendicular to the surface", *Journal of the Chemical Society, Faraday Transactions I*, vol. 85, no. 7, pp. 1765-1774.
- Jaffe, B., Cook, W. R. and Jaffe, H. (1971), *Piezoelectric Ceramics*, 1st ed, Academic Press Inc, London.
- Jana, N. R. (2004), "Shape effect in nanoparticle self-assembly", *Angewandte Chemie - International Edition*, vol. 43, no. 12, pp. 1536-1540.
- Jenkins, T. E. (1995), "Electrical conductivity", in *Semiconductor science: Growth and characterization techniques*, 1st ed, Prentice Hall, , pp. 151-155.
- Jones, P. M. (2003), "Investigation into the nanoscale interactions of SPM tips with ferroelectric surfaces", MSc Thesis, Cranfield University.
- Kalinin, S. V. and Bonnell, D. A. (2004), "Screening phenomena on oxide surface and its implications for local electrostatic and transport measurements", *Nano Letters*, vol. 4, no. 4, pp. 555-560.
- Kalinin, S. V. and Bonnell, D. A. (2001), "Local potential and polarization screening on ferroelectric surfaces", *Physical Review B*, vol. 63, no. 12, pp. 125411-125413.
- Kalinin, S. V., Bonnell, D. A., Alvarez, T., Lei, X., Hu, Z., Ferris, J. H., Zhang, Q. and Dunn, S. (2002), "Atomic polarization and local reactivity on ferroelectric surfaces: A new route towards complex nanostructures", *Nano Letters*, vol. 2, no. 6, pp. 589-593.
- Kalinin, S. V., Bonnell, D. A., Alvarez, T., Lei, X., Hu, Z., Shao, R. and Ferris, J. H. (2004), "Ferroelectric lithography of multicomponent nanostructures", *Advanced Materials*, vol. 16, no. 9-10, pp. 795-799.
- Keidel, E. (1929), "Die Beeinflussung der Lichtechtheit von Teerfarblacken durch Titanweiss [Influence of titanium white on the fastness to light of coal-tar days]", *Farben-Zeitung*, vol. 34, pp. 1242-1243.
- Kholkin, A. L., Yarmarkin, V. K., Goltsman, B. M. and Baptista, J. L. (2001), "Photoelectric evaluation of polarization and internal field in PZT thin film", *Integrated Ferroelectrics*, vol. 35, no. 1-4, pp. 261-268.

- Khomutov, G. B., Kislov, V. V., Antipina, M. N. and Gainutdinov, R. V. (2003), "Interfacial nanofabrication strategies in development of new functional nanomaterials and planar supramolecular nanostructures for nanoelectronics and nanotechnology", *Microelectronic Engineering*, vol. 69, no. 1, pp. 373-383.
- Kim, Y., Buhlmann, S., Kim, J., Park, M., No, K., Kim, Y. K. and Hong, S. (2007), "Local surface potential distribution in oriented ferroelectric thin films", *Applied Physics Letters*, vol. 91, no. 5., pp. 052906-052909.
- Kiselev, D. A., Bdikin, I. K., Selezneva, E. K., Bormanis, K., Sternberg, A. and Kholkin, A. L. (2007), "Grain size effect and local disorder in polycrystalline relaxors via scanning probe microscopy", *Journal of Physics D: Applied Physics*, vol. 40, no. 22, pp. 7109-7112.
- Kobayashi, T., Ichiki, M., Tsaur, J. and Maeda, R. (2005), "Effect of multi-coating process on the orientation and microstructure of lead zirconate titanate (PZT) thin films derived by chemical solution deposition", *Thin Solid Films*, vol. 489, no. 1-2, pp. 74-78.
- Lairson, B. M., Visokay, M. R., Sinclair, R., Hagstrom, S. and Clemens, B. M. (1992), "Epitaxial Pt(001), Pt(110), and Pt(111) films on MgO(001), MgO(110), MgO(111), and Al[sub 2]O[sub 3](0001)", *Applied Physics Letters*, vol. 61, no. 12, pp. 1390-1392.
- Lee, H., Hesse, D., Zakharov, N. and Gösele, U. (2002), "Ferroelectric Bi<sub>3.25</sub>La<sub>0.75</sub>Ti<sub>3</sub>O<sub>12</sub> Films of Uniform a-Axis Orientation on Silicon Substrates", *Science*, vol. 296, no. 5575, pp. 2006-2009.
- Lee, H., Kang, Y. S., Cho, S. J., Xiao, B. and Morkoc, H. (2005), "Dielectric functions and electronic band structure of lead zirconate titanate thin films", *Journal of Applied Physics*, vol. 98, no. 9, pp. 94108-1 - 94108-10.
- Lee, J. and Joo, S. (2002), "Analysis of grain-boundary effects on the electrical properties of Pb(Zr,Ti)O<sub>3</sub> thin films", *Applied Physics Letters*, vol. 81, no. 14, pp. 2602-2604.
- Lei, X., Kalinin, S. V., Hu, Z. and Bonnell, D. A. (2004), "Ferroelectric lithography of multicomponent nanostructure", *Ceramic Nanomaterials and Nanotechnology II*, Vol. 148, Nashville, TN, American Ceramic Society, pp. 39.
- Lei, X., Li, D., Shao, R. and Bonnell, D. A. (2005), "In situ deposition/positioning of magnetic nanoparticles with ferroelectric nanolithography", *Journal of Materials Research*, vol. 20, no. 3, pp. 712-718.
- Loweckamp, J. B., Rohrer, G. S., Hotsenpiller, P. A., Bolt, J. D. and Farneth, W. E. (1998), "Anisotropic photochemical reactivity of bulk TiO<sub>2</sub> Crystals", *Journal of Physical Chemistry B*, vol. 102, no. 38, pp. 7323-7327.
- Mackenzie, J. and Xu, Y. (1997), "Ferroelectric materials by the Sol-Gel method", *Journal of Sol-Gel Science and Technology*, vol. 8, pp. 673-679.



- Many, A., Goldstein, Y. and Grover, N. B. (1965), "Semiconductor-electrolyte interface", in *Semiconductor Surfaces*, 1st ed, North-Holland Publishing Company, Amsterdam, pp. 415-425.
- Markvart, T. (2000), "How solar cells work", in Markvart, T. (ed.) *Solar Cells*, 2nd ed, John Wiley and Son, Chichester, pp. 29-34.
- Matsuura, H. (2000), "Calculation of band bending in ferroelectric semiconductor", *New Journal of Physics*, vol. 2. pp.8.1-8.11.
- Mihara, T., Watanabe, H., Yoshimori, H., De Araujo, C. A., Melnick, B. and McMillan, L. D. (1992), "Process dependent electrical characteristics and equivalent circuit model of sol-gel based PZT capacitors", *Integrated Ferroelectrics*, vol. 1, no. 2, pp. 269-291.
- Mills, A. and Le Hunte, S. (1997), "An overview of semiconductor photocatalysis", *Journal of Photochemistry and Photobiology A: Chemistry*, vol. 108, no. 1, pp. 1-35.
- Mulvaney, P. (2001), "Nanoscale Materials in Chemistry", in Klabunde, K. J. (ed.) Wiley and Sons, Canada, pp. 121-128.
- Ozin, G. A. and Arsenault, A. (2005), "Nanochemistry Basics", in *Nanochemistry: A chemical approach to nanomaterials*, 1st ed, The Royal Society of Chemistry, Cambridge, pp. 1-33.
- Padovani, S., Sada, C., Mazzoldi, P., Brunetti, B., Giulivi, A., D'Acapito, F. and Battaglin, G. (2003), "Copper in glazes of renaissance luster pottery: Nanoparticles, ions, and local environment", *Journal of Applied Physics*, vol. 93, no. 12, pp. 10058-10063.
- Pandey, S. K., James, A. R., Raman, R., Chatterjee, S. N., Goyal, A., Prakash, C. and Goel, T. C. (2005), "Structural, ferroelectric and optical properties of PZT thin films", *Physica B: Condensed Matter*, vol. 369, no. 1-4, pp. 135-142.
- Pintilie, L. and Alexe, M. (2005), "Metal-ferroelectric-metal heterostructures with Schottky contacts. I. Influence of the ferroelectric properties", *Journal of Applied Physics*, vol. 98, no. 12, pp. 1-8.
- Pintilie, L., Lisca, M. and Alexe, M. (2005), "Lead-based ferroelectric compounds: insulators or semiconductors", *Integrated Ferroelectrics*, vol. 73, pp. 37-48.
- Pintilie, L. and Pintilie, I. (2001), "Ferroelectrics: new wide-gap materials for UV detection", *Materials Science and Engineering: B*, vol. 80, no. 1-3, pp. 388-391.
- Pleskov, Y. V. and Gurevich, Y. Y. (1986), *Semiconductor photoelectrochemistry*, 1st ed, Consultants Bureau, New York.

- Popov, A. P., Priezhev, A. V., Lademann, J. and Myllyla, R. (2005), "TiO<sub>3</sub> nanoparticles as an effective UV-B radiation skin-protective compound in sunscreens", *Journal of Physics, D: Applied Physics*, vol. 38, pp. 2564-2570.
- Raymond, M. V. and Smyth, D. M. (1996), "Defects and charge transport in perovskite ferroelectrics", *Journal of Physics and Chemistry of Solids*, vol. 57, no. 10, pp. 1507-1511.
- Roy, S. S., Gleeson, H., Shaw, C. P., Whatmore, R. W., Huang, Z., Zhang, Q. and Dunn, S. (2000), "Growth and characterisation of lead zirconate titanate (30/70) on indium tin oxide coated glass for oxide ferroelectric-liquid crystal display application", *Integrated Ferroelectrics*, vol. 29, no. 3-4, pp. 189-213.
- Scott, J. F. (2000), *Ferroelectric memories*, Springer, Berlin ; London.
- Scott, J. F. (1999), "Device physics of ferroelectric thin-film memories", *Japanese Journal of Applied Physics*, vol. 38, pp. 2272-2274.
- Scott, J. F., Watanabe, K., Hartmann, A. J. and Lamb, R. N. (1999), "Device models for PZT/Pt, BST/Pt, SBT/Pt, and SBT/Bi ferroelectric memories", *Ferroelectrics*, vol. 225, no. 1-4, pp. 83-90.
- Shaw, C. P., Roy, S. S., Whatmore, R. W., Gleeson, H., Huang, Z., Zhang, Q. and Dunn, S. (2001), "Growth and characterisation of lead zirconate titanate (30/70) thin films using TiO<sub>2</sub> seeding for oxide ferroelectric-liquid crystal display application", *Ferroelectrics*, vol. 256, pp. 159-174.
- Silva, M. S., Cilense, M., Orhan, E., Goes, M. S., Machado, M. A. C., Santos, L. P. S., Paiva-Santos, C. O., Longo, E., Varela, J. A., Zaghet, M. A. and Pizani, P. S. (2005), "The nature of the photoluminescence in amorphized PZT", *Journal of Luminescence*, vol. 111, no. 3, pp. 205-213.
- Smyth, D. M. (1991), "Charge motion in ferroelectric thin films", *Second Symposium on Integrated Ferroelectrics*, Vol. 116, 6-8 March 1990, Monterey, CA, USA, pp. 117.
- Sun, S., Mendes, P., Critchley, K., Diegoli, S., Hanwell, M., Evans, S. D., Leggett, G. J., Preece, J. A. and Richardson, T. H. (2006), "Fabrication of gold micro and nanostructures by photolithographic exposure of thiol-stabilized gold nanoparticles", *Nano Letters*, vol. 6, no. 3, pp. 345-350.
- Tanaka, K., Harada, K. and Murata, S. (1986), "Photocatalytic deposition of metal ions onto TiO<sub>2</sub> powder", *Solar energy*, vol. 36, no. 2, pp. 159-161.
- Torres, J. and Cervera-March, S. (1992), "Kinetics of the photoassisted catalytic oxidation of Pb(II) in TiO<sub>2</sub> suspensions", *Chemical Engineering Science*, vol. 47, no. 15-16, pp. 3857-3862.
- Trasatti, S. (1986), "Absolute electrode potential : an explanatory note", *Pure and Applied Chemistry*, vol. 58, no. 7, pp. 955-966.

- Tryk, D. A., Fujishima, A. and Honda, K. (2000), "Recent topics in photoelectrochemistry: Achievements and future prospects", *Electrochimica Acta*, vol. 45, no. 15-16, pp. 2363-2376.
- Tuttle, B. A., Voigt, J. A., Goodnow, D. C., Lamppa, D. L., Headley, T. J., Eatough, M. O., Zender, G., Nasby, R. D. and Rodgers, S. M. (1993), "Highly Oriented, Chemically Prepared Pb(Zr, Ti)O<sub>3</sub> Thin Films", *Journal of the American Ceramic Society*, vol. 76, no. 6, pp. 1537-1544.
- Van de Krol, R. and Tuller, H. L. (2002), "Electroceramics - the role of interfaces", *Solid State Ionics*, vol. 150, pp. 167-179.
- Walter, P., Welcomme, E., Hallegot, P., Zaluzec, N. J., Deeb, C., Castaing, J., Veyssiere, P., Breniaux, R., Leveque, J. - and Tsoucaris, G. (2006), "Early Use of PbS Nanotechnology for an Ancient Hair Dyeing Formula", *Nano Letters*, vol. 6, no. 10, pp. 2215-2219.
- Wang, Y. X. and Zhong, W. L. (2002), "First principles study on the ferroelectricity of the perovskite ABO<sub>3</sub> ferroelectrics", *Chinese Physics*, vol. 11, no. 7, pp. 714-719.
- Warner, J. H. and Tilley, R. D. (2005), *Advanced Materials*, vol. 17, no. 1, pp. 2997-3001.
- Waser, R. and Hagenbeck, R. (2000), "Grain boundaries in dielectric and mixed-conducting ceramics", *Acta Materialia*, vol. 48, pp. 797-825.
- Wouters, D. J., Willems, G. J. and Maes, H. E. (1995), "Electrical conductivity in ferroelectric thin films", *Microelectronic Engineering*, vol. 29, no. 1-4, pp. 249-256.
- Xu, Y. (2001), "Ferroelectric thin films fabricated by Sol-Gel technique", *6th International Conference on Solid-State and IC Technology*, Vol. 1, Shanghai, IEEE, Piscataway, NJ, pp. 696-699.
- Yamamoto, M., Kashiwagi, Y., Sakata, T., Mori, H. and Nakamoto, M. (2005), "Synthesis and morphology of star-shaped gold nanoplates protected by poly(N-vinyl-2-pyrrolidone)", *Chemistry of Materials*, vol. 17, no. 22, pp. 5391-5393.
- Yang, W. C., Rodriguez, B. J., Gruverman, A. and Nemanich, R. J. (2004), "Polarisation-dependant electron affinity of LiNbO<sub>3</sub> surfaces", *Applied Physics Letters*, vol. 85, no. 12, pp. 2316-2318.
- Zhang, W. (2003), "Nanoscale iron particles for environmental remediation: An overview", *Journal of Nanoparticle Research*, vol. 5, no. 3-4, pp. 323-332.
- Zheng, K., Lu, J. and Chu, J. (2004), "A novel wet etching process of Pb(Zr,Ti)O<sub>3</sub> thin films for applications in microelectromechanical system", *Japanese Journal of Applied Physics, Part 1: Regular Papers and Short Notes and Review Papers*, vol. 43, no. 6 B, pp. 3934-3937.

- Zhong, X., Xie, R., Sun, L., Lieberwirth, I. and Knoll, W. (2005), "Synthesis of dumbbell-shaped manganese oxide nanocrystals", *Journal of Physical Chemistry B*, vol. 110, no. 1, pp. 2-4.
- Zhu, X. Y. (1994), "Surface photochemistry", *Annual Review of Physical Chemistry*, vol. 45, pp. 113-144.

## **Appendixes**

# Photo-reduction of silver salts on highly heterogeneous lead zirconate titanate

P M Jones and S Dunn

Nanotechnology Centre, Cranfield University, Bedfordshire MK43 0AL, UK

E-mail: [s.c.dunn@cranfield.ac.uk](mailto:s.c.dunn@cranfield.ac.uk)

Received 16 January 2007, in final form 1 March 2007

Published 5 April 2007

Online at [stacks.iop.org/Nano/18/185702](http://stacks.iop.org/Nano/18/185702)

## Abstract

This paper presents the work undertaken to determine the influences on the photo-induced growth of silver nanoclusters on the surfaces of lead zirconate titanate thin films. The lead zirconate titanate films were grown on indium tin oxide coated glass. They exhibited a highly textured surface and can be treated as wide bandgap semiconductors that exhibit ferroelectric behaviour. We show that there is a preferential deposition of silver metal on the ferroelectric films that is related not only to the polarization state of the ferroelectric domains but also to the surface defects such as grain boundaries and defects within the film. The greatest deposition rates are found to occur at grain boundaries where there is an approximately 40:1 ratio of silver clusters when compared to the native positive domains exhibited by the lead zirconate titanate. We propose that the mechanism for cluster growth depends on the availability, and diffusion rate, of electrons into the growing cluster and that the clusters grow from a discrete nucleation point. We also show that the growth of a monolayer of silver is sufficient to prevent the formation of electron–hole pairs by blocking the UV irradiation and that the silver nanoparticles are readily removed from the surface using an ultrasonic bath leading to a possible new method of manufacturing metal nanoparticles.

(Some figures in this article are in colour only in the electronic version)

## 1. Introduction

The ability of semiconducting materials to engage in photochemical reactions is well known—the evolution of electron–hole pairs through sufficiently high energy irradiation allows both reduction and oxidation to occur through the donation of the hole or electron. Recently it has been shown that it is possible to treat ferroelectric materials as wide bandgap semiconductors where both oxidation and reduction of materials has been demonstrated [1, 2] and that the surface polarization can influence the absorption of large polar molecules. There are certain advantages to using a ferroelectric material in photochemical reactions which stem from the spatial separation of the oxidation and reduction regions [3]. A further peculiarity stems from the spontaneous polarization of ferroelectrics. This leads to unique surface properties where a polarization dependent surface charge develops [4]. There is now a growing body of literature which is showing that ferroelectric surfaces can be used to perform ‘nanolithography’ and be used for the directed growth of metal nanoparticles [5].

When the bulk of a ferroelectric is broken by an interface, such as at the surface or a grain boundary, a space charge region forms. In order to form an energetically stable state there are two possible screening processes; one internal, the other external to the material. The external process can be described as ions or polarizable molecules of opposite sign to the surface charge adsorbing on the surface due to charge attraction. This is described by classic DLVO theory and is the Stern layer associated with charged surfaces [1]. Internal screening takes the form of a space charge region. The polarization of the surface of the ferroelectric is dependent on the orientation of the ferroelectric domain due to the dipole developed in the distorted crystal lattice.

It has been stated that ferroelectrics such as lead zirconate titanate (PZT) can be thought of as wide bandgap semiconductors [6] rather than pure insulators. It has been shown that an energy of between 4.1 eV [7] and 4.5 eV [8] is required to generate silver nanoclusters on the surface of PZT. The bandgap for PZT has been variously shown to be in the region of 3.2–3.7 eV [9]. There is however one

### Photochemical Growth of Silver Nanoparticles on $c^-$ and $c^+$ Domains on Lead Zirconate Titanate Thin Films

Steve Dunn,\* Paul M. Jones, and Diego E. Gallardo

*Contribution from the Nanotechnology Centre, Cranfield University, Building 30, Cranfield, MK43 0AL, United Kingdom*

Received March 7, 2007; E-mail: s.c.dunn@cranfield.ac.uk

**Abstract:** The photochemical growth of silver nanoparticles on the negative domains of lead zirconate titanate thin films is reported. A sample of highly [100] orientated lead zirconate titanate, with a ratio of 30:70, that was 65–70 nm thick grown on Pt-coated MgO was poled by use of piezoresponse force microscopy to produce defined regions of surface positive and negative polarization. A comparison between the growth of silver nanoparticles on the surface of the lead zirconate titanate when illuminated with two sources of super band gap UV is given. In both cases the wavelength of illumination leads to growth on the positive domains but only illumination with a Honle H lamp, with a high photon output over 250–200 nm, caused significant growth of silver nanoparticles on the negative domain. The deposition on the negative domain is explained in terms of changed band bending due to the excitation of electrons into the conduction band, the rate of decay to the ground state, and dimensions of the ferroelectric film. The rate of deposition of silver nanoparticles on the negative domains is approximately half that on the positive domains.

#### Introduction

There has been growing interest in processes that can be used to provide control of the development of nanostructures that are both highly defined and well controlled. One such technique that has been showing increased promise in the past 2–3 years is that of ferroelectric lithography. Ferroelectric lithography has been shown to produce nanostructures that have a variety of potential uses, such as interconnects in nanoelectronic<sup>1</sup> or microelectronic devices, chemical sensors,<sup>2</sup> or labels in biological and other sensing systems.<sup>3</sup> Recently it has been shown that lead zirconate titanate (PZT) can be used to make and release silver nanoparticles of varying sizes<sup>4</sup> and that lithium niobate can be used to produce very high aspect ratio silver nanowires.<sup>5</sup> Where it is possible to reproduce with good fidelity a nanostructure, there exists an opportunity to generate a nanolithographic technique. Where this is not possible, then there may exist a method of producing interesting or functional nanoparticles on surfaces that can subsequently be removed and used in a useful manner.

When the bulk of a ferroelectric is broken by an interface, such as at the surface or a grain boundary, a depolarization field forms. In order to form an energetically stable state, there are two possible screening processes; one internal, the other external to the material. The external process can be described as ions or polarizable molecules of opposite sign to the surface charge adsorbing on the surface due to charge attraction. This is described by classic Derjaguin–Landau–Verwey–Overbeek

(DLVO) theory and is the Stern layer associated with charged surfaces. Internal screening takes the form of a space-charge region forming due to band bending when in close proximity to the interface. The polarization of the surface of the ferroelectric is dependent on the orientation of the ferroelectric domain due to the dipole developed in the distorted crystal lattice. In positive domains the surface charge will be negative, and in negative domains it will be positive.

It has been stated that lead-based ferroelectrics such as PZT can be thought of as wide band gap semiconductors<sup>6,7</sup> rather than pure insulators. Work by Kalinin et al.<sup>8</sup> and Giocondi and Rohrer<sup>9</sup> showed that band bending due to the ferroelectric nature of the material has a major impact on the nature of the photochemical reactions that take place on the surface. It is possible to discuss the processes taking place at the surface interface using common semiconductor terminology.<sup>7</sup> There is, however, one major addition that must be considered and that is the domain-dependent polarization effects. Ferroelectric materials such as PZT have a macroscopic polarization that induces the accumulation of charges at the surfaces. In positive domains, a positive charge is present at the surface of the material. This surface charge is screened by external and internal mechanisms. The internal mechanism consists of the formation of a negative space-charge region below the surface. This creates an internal electric field that bends the energy bands near the surface of the material. The external mechanism consists of the adsorption of foreign negatively charged molecules at the

- (1) Wissner-Gross, A. *Nanotechnology* **2006**, *17*, 4986–4990.
- (2) Fan, Z.; Liu, J. *Appl. Phys. Lett.* **2005**, *86*, 123510–123511.
- (3) Salata, O. J. *Nanobiotech.* **2004**, *2*–3, 3–9.
- (4) Jones, P. M.; Dunn, S. *Nanotechnology* **2007**, 185702–185708.
- (5) Hanson, J. N.; Rodriguez, B. J.; Nemanich, R. J.; Gruverman, A. *Nanotechnology* **2006**, *17*, 4946–4949.

- (6) Boerasu, I.; Pintilie, L.; Pereira, M.; Vasilevskiy, I.; Gomes, M. J. M. *J. Appl. Phys.* **2003**, *93*, 4776–4783.
- (7) Pintilie, L.; Lisca, M.; Alexe, M. *J. Optoelectron. Adv. Mater.* **2006**, *8*, 7–12.
- (8) Kalinin, S. V.; Bonnell, D. A.; Alvarez, T.; Lei, X.; Hu, Z.; Ferris, J. H.; Zhang, Q.; Dunn, S. *Nano Lett.* **2002**, *6*, 589–593.
- (9) Giocondi, J. L.; Rohrer, G. S. *J. Phys. Chem. B* **2001**, *105*, 8275–8277.

# Insights into the relationship between inherent materials properties of PZT and photochemistry for the development of nanostructured silver

Steve Dunn,\* Divya Tiwari, Paul M. Jones and Diego E. Gallardo

Received 16th July 2007, Accepted 14th September 2007

First published as an Advance Article on the web 25th September 2007

DOI: 10.1039/b710894j

Recently there has been great interest in using patterned ferroelectric materials for the photochemical growth of metal nanostructures. Variations in surface and sub-surface structure influence the photochemical processes. Here we show that crystallography, and hence remnant polarization, of the ferroelectric affects photo-deposition. The ratio of metal growth on  $c^-$  and  $c^+$  domains varies from 1 : 2 for [100] to 1 : 100 for [111]. This is shown to be dependent on the variations in the band structure.

The desire to produce highly defined and well controlled metal nanostructures has been an area of research that has been gaining interest. Such metal nanostructures have a wide variety of applications that range from interconnects for nanoelectronic devices<sup>1</sup> to sensors for biological systems.<sup>2</sup> One technique that has been increasingly investigated over the past 5 years is ferroelectric lithography, which was first reported by Giocondi and Rohrer<sup>3</sup> in 2001 and then further investigated by Kalinin *et al.*<sup>4</sup> where the term ferroelectric lithography was first used. Since that time further work has shown that surface features on the ferroelectric,<sup>5</sup> energy of irradiation<sup>6</sup> and defect density<sup>7</sup> can all affect the density and morphology of metal nanoparticles produced by photoexcitation of the ferroelectric. Where it is possible to reproduce with good fidelity a nanostructure, there exists an opportunity to generate a nanolithographic technique. Where this is not possible there may exist a method to produce interesting nanostructures that can subsequently be removed and be useful elsewhere. Previously it has been shown that ferroelectric materials can be made with surface features as fine as 7 nm with good structural control.<sup>8,9</sup>

When the bulk of a ferroelectric is broken by an interface such as a surface or grain boundary a depolarization field forms. Two possible screening processes can occur to produce an energetically stable state: one internal, the other external to the material. If we think of lead based ferroelectrics such as lead zirconate titanate (PZT) as wide bandgap semiconductors<sup>10,11</sup> rather than pure insulators then we are able to describe the behaviour of the material in terms of standard semi-conductor theory.<sup>4</sup> The work by Kalinin *et al.*<sup>4</sup> and Giocondi and Rohrer<sup>3</sup> shows that band bending due to the ferroelectric nature of the material has a major impact on the photochemical reactions that take place on the surface. There is, however, one factor that must be considered: domain dependant polarization effects. Ferroelectric materials such as PZT have a macroscopic polarization that induces the

accumulation or depletion of charges at the surfaces. In positive domains, a positive polarization charge is present at the surface of the material. Internal screening takes the form of a space-charge region forming due to band bending when in close proximity to the interface. The polarization of the surface of the ferroelectric is dependent on the orientation of the ferroelectric domain due to the dipole developed in the distorted crystal lattice. Previous work has commented that the space charge region does not form complete screening of the internal dipole.<sup>12</sup> Therefore an external mechanism exists, which consists of the adsorption of foreign charged molecules at the surface. This is described by classic Derjaguin–Landau–Verwey–Overbeek (DLVO) theory and is the Stern layer associated with charged surfaces. In both types of domain, the polarization field is cancelled at equilibrium by the screening mechanisms.

When the ferroelectric is exposed to high energy ultraviolet light, electron–hole pairs formed near or within the space-charge region are driven apart by the internal electric field.<sup>13</sup> Mobile electrons are then forced to migrate to the surface of positive domains<sup>14</sup> and towards the bulk in negative domains. If a positive domain is immersed in a metal salt solution such as  $\text{AgNO}_3$  and exposed to ultraviolet light, the accumulated electrons below the surface can react with the  $\text{Ag}^+$  cations in solution. These electrons tunnel across the barrier and reduce the silver cation to form metal atoms that are adsorbed on the ferroelectric surface. Giocondi and Rohrer<sup>3</sup> pointed out that the adsorption of the Ag onto the surface cannot be ion polarization dependent as the  $\text{Ag}^+$  ions and the surface of the ferroelectric  $c^+$  domain are both positive. This means that the ion should be repelled if the process was polarity driven. The successful formation of the silver clusters supports the theories of Zhu<sup>13</sup> and Kalinin.<sup>14</sup> Further work has shown that the density of states of the ferroelectric material and the energy of irradiation can impact on the photochemical deposition process.<sup>6</sup> By irradiating a sample of PZT with a high dose of high energy photons a different pattern of photo-deposited silver metal was seen compared with that obtained from a lower energy source.<sup>6</sup> The differences in the deposition of the silver were explained in terms of the density of states of the PZT and changes in the band bending.

PZT films, with a zirconium : titanium ratio of 30 : 70, were made using sol–gel (maximum processing temperature of 530 °C). The sol was then spin coated onto a prepared substrate, which in our case was 100 nm of Pt sputtered onto either [100] MgO or [111] silicon.<sup>9</sup> The sample was 1 cm<sup>2</sup>. The PZT films exhibited good [111] orientation if grown on Si or good [100] orientation if grown on MgO, orientation as determined by X-ray diffraction (XRD), and consisted of discrete 70–100 nm grains with a random

Nanotechnology Centre, Cranfield University, Building 30, Cranfield, UK MK43 0AL. E-mail: s.c.dunn@cranfield.ac.uk



# Photochemical Investigation of a Polarizable Semiconductor, Lead-Zirconate-Titanate

P. M. Jones, D. E. Gallardo, and S. Dunn\*

Nanotechnology Centre, Cranfield University, Bedfordshire, MK43 0AL United Kingdom

Received February 5, 2008. Revised Manuscript Received July 14, 2008

In this work, we have investigated the photochemical reaction with a variety of metal salts on a polarizable semiconductor, lead zirconate titanate (PZT 30/70 [111]). The exact position of the band edges can influence properties such as the width of the space-charge region and barriers for charge injection, which play an important role in devices built with such materials such as FeRAM and MLC. Observations show that there can be metal deposition on positive domains or photodecomposition on negative domains. The exact reaction was found to be dependent on the reduction potential of the cation and whether a nitrate or chloride salt was used. We show that for certain cations such as  $\text{Fe}^{2+}$ , with a reduction potential near the edge of the conduction band of the PZT, either reduction or photodecomposition can happen. This effect can be explained because of the presence of an uncertainty in the location of the band edges at the surface of the PZT. The exact position of these edges is determined by the Fermi level's pinning location, which is dependent on the surface states specific to each sample. Therefore, the location of the band edges is sensitive to the crystallization process during manufacture within a range of energies. Issues such as the location of the conduction band with respect to the vacuum and size of the band gap are of interest when incorporating ferroelectric materials into devices and impact on fundamental properties such as fatigue.

Ferroelectric materials, such as lead-zirconate-titanate (PZT) or barium titanate, have been used in a variety of applications such as non-volatile memory devices (NV RAM) because of their reversible polarity or capacitors because of the high dielectric constant. A continuing question regarding the use of ferroelectrics in NV RAM and other devices is controlling fatigue and leakage current; therefore, determining the interaction between the electrode and ferroelectric material. In all of these devices, it is important to know the position of the band edges, as it influences the operating parameters of the device and the possible failure mechanisms. This interest ranges from addressing questions such as the impact of size on a Schottky barrier to the processing of the material. We have selected PZT as the photoactive surface in order to investigate the position of the band edges using a photochemical technique because of the ease in patterning the surface for selective REDOX reactions and its high photostability and polarizability when in thin film form. As PZT has a high polarizability, it can effectively separate any photogenerated electron/hole pairs. Additionally, ferroelectrics such as PZT can be treated as polarizable wide band gap semiconductors, and when illuminated with super bandgap UV,<sup>1,2</sup> electron–hole pairs form.

In the case of a ferroelectric material, the depolarization field is partially, if not completely, internally screened.<sup>3</sup> The

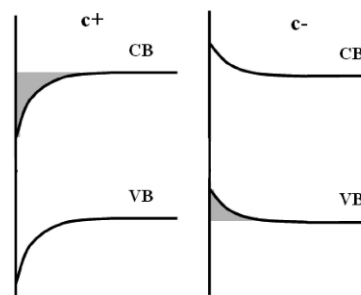


**Figure 1.** Configuration of the band edges at the surface of polarized PZT (p-type). In  $c^+$  domains (left), the depolarisation field causes downward band bending and  $h^+$  depletion. Photogenerated  $e^-$  will move toward the surface and can take part in reduction reactions. In  $c^-$  domains (right), the bands are bent upward and there is a  $h^+$  accumulation at the surface. Photogenerated  $e^-$  will move away from the surface, preventing reduction reactions, whereas oxidation reactions are allowed by the presence of accumulated and photogenerated  $h^+$ .

configuration of the valence and conduction band edges at the surface of the PZT is determined by the polarization charges and surface states introduced by defects and dangling bonds.<sup>4</sup> The density of these charges is thought to influence the pinning of the Fermi level.<sup>5</sup> Under these conditions, the band diagram at the surface in positive ( $c^+$ ) and negative ( $c^-$ ) domains can be described as in Figure 1. The depolarization field causes downward bending and hole ( $h^+$ ) depletion at the surface of  $c^+$  domains, whereas in the  $c^-$

\* Corresponding author. E-mail: s.c.dunn@cranfield.ac.uk.

- (1) Yang, W. C.; Rodriguez, B. J.; Gruverman, A.; Nemanich, R. J. *Appl. Phys. Lett.* **2004**, 85, 2316.
- (2) Pintilie, L.; Liscu, M.; Alexe, M. *J. Optoelectron. Adv. Mater.* **2006**, 8, 7.
- (3) Fridkin, V. M., *Photoferroelectrics*; Springer-Verlag: New York, 1979, 46.

- (4) Dunn, S.; Tiwari, D.; Jones, P. M.; Gallardo, D. E. *J. Mater. Chem.* **2007**, 17, 4460.

- (5) Bard, A. J.; Bocarsly, A. B.; Fan, F. F.; Walton, E. G.; Wrighton, M. S. *J. Am. Chem. Soc.* **1980**, 102, 3671.

## Conferences

**Presented - Ferroelectrics UK, 2006, Birmingham, UK**

### **Boundary effects on the deposition of Ag onto PZT thin films under UV irradiation.**

Paul Jones, Steve Dunn

The deposition of metal salts onto ferroelectric substrates using UV radiation has already been done by groups such as Bonnell's<sup>1</sup>. Preferential Ag deposition on to positively poled domains has been attributed to surface band bending due to the polar nature of the materials. To date the films studied have been highly orientated or single crystal substrates and thus the domain structure was the main factor affecting metal deposition. The experimental results for Ag nanocluster deposition under UV irradiation on to sol gel derived PZT on ITO is presented here. The structure of the film was of mix of connected and individual perovskite rosettes in a pyrochlore matrix. Where rosettes meet each a grain boundary forms and it was observed that Ag clusters preferentially deposited at these interfaces more rapidly than elsewhere on the surface.

The experimental work showed that the order of preference for metal deposition was first at grain boundaries and then the positively poled perovskite surface of the rosette. We believe that the preferential deposition at the grain boundaries could be accounted for as follows. At grain boundaries (GB) an atomic mismatch occurs which in turn affects the properties of that area relative to the bulk. A depletion region forms on both sides of the boundary and generates a potential difference (PD), the highest level being at the boundary core. The PD will be higher at the core than that caused by band bending at the film surface. When irradiated with super bandgap UV light (200-300nm) electron/hole pairs are formed. The electrons are attracted to the surface of the film in positive domains by the positive potential. Due to the higher PD at the GB the electrons in the surrounding area on either side of the boundary will be attracted to it and thus more electrons will be available for metal ion reduction and thus cluster formation.

---

<sup>1</sup> Bonnell, D. A. and Kalinin, S. V. (2002), *Ferroelectric Thin Films X*, Vol. 688, pp. 317-328.

**Presented – International Symposium on Applied Ferroelectrics, 2007, Nara city, Japan**

**The effect of wavelength on the deposition of Ag onto PZT thin films during UV irradiation.**

Paul Jones, Steve Dunn

Abstract: The deposition of metal salts onto ferroelectric substrates using UV radiation has been undertaken by the authors. Preferential Ag deposition on to positively poled domains has been attributed to surface band bending due to the polar nature of the materials. The experimental results for Ag nanocluster deposition under UV irradiation on to sol-gel derived PZT are presented here. When irradiated with super bandgap UV light ranging from 200 to 300nm electron/hole pairs are formed. The electrons are attracted to the surface of the film in positive domains and at grain boundaries due to band bending. At grain boundaries more electrons are available from the surrounding area and metal cluster formation is faster at these points. By varying the wavelength of the UV light it is possible to control the growth rate and size of the clusters.

# Poster

## Nanomaterials and Nanomanufacture, 2007, Dublin, Ireland

### Nanoparticle Synthesis by Photo Induced Reduction and Oxidation Processes on PZT Thin Films

Paul Jones, Steve Dunn

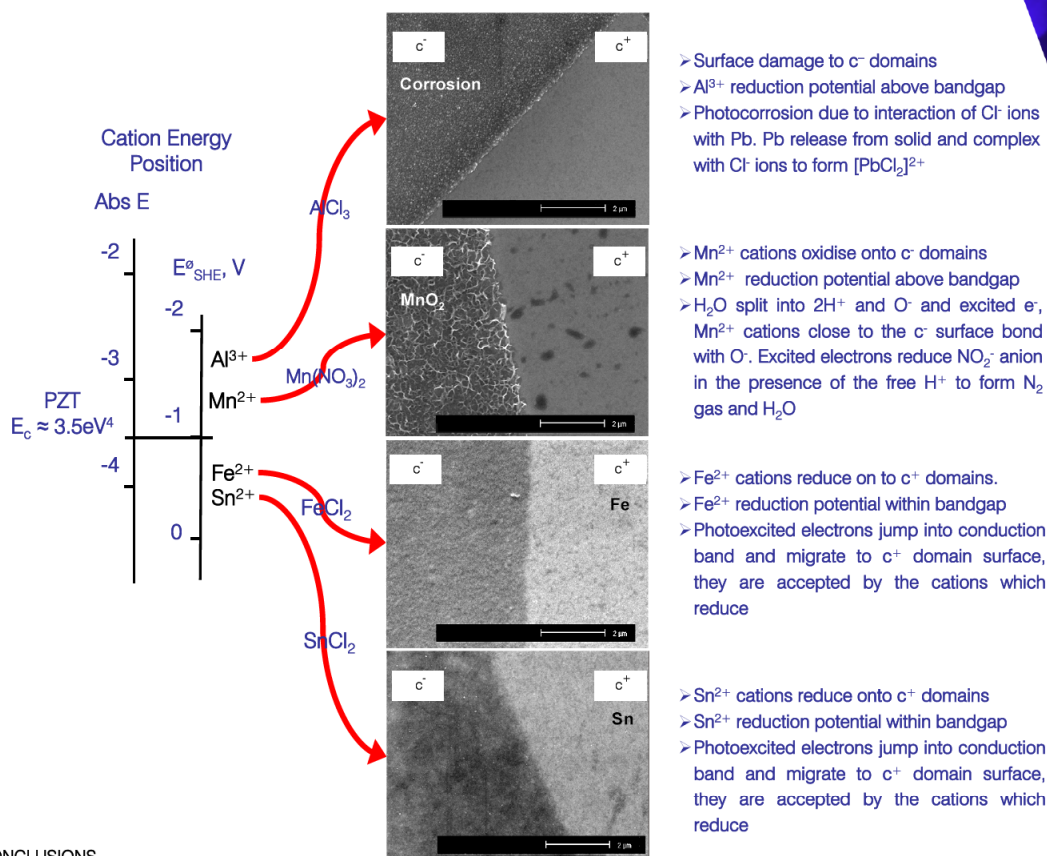
**Cranfield**  
UNIVERSITY

#### INTRODUCTION

- Reduction and oxidation of metal salts on ferroelectric surfaces under UV irradiation have been found to be domain specific<sup>1</sup> and related to energy band bending in the surface.<sup>2</sup>
- The aim of this work is to investigate the effect of cation reduction potential with respect to the bandgap of the ferroelectric on the reduction and oxidation processes taking place on the surface.

#### EXPERIMENTAL PROCEDURE

- Films used: 70nm thick PZT (30/70) [111] orientated<sup>3</sup>
- Metal salts used:  $\text{SnCl}_2$ ,  $\text{FeCl}_2$ ,  $\text{Mn}(\text{NO}_3)_2$ ,  $\text{AlCl}_3$
- PZT samples immersed in individual salt solutions and irradiated with super bandgap UV for 2 hours.
- Samples rinsed and dried then analysed with SEM and EDX.



#### CONCLUSIONS

- The redox reactions that occur between a metal salt solution and a PZT surface are related to its redox position relative to the bandgap.
- When salt reduction potential is within the bandgap there is a tendency to reduce on the +ve domains.
- As salt reduction potential moves towards the conduction band edge the reduction rate decreases and finally stops when the band edge is reached.
- Nitrate salts with reduction potential above band edge cations have tendency to oxidise onto the negative domains.
- Chloride salts with metal cations above the band edge have tendency to corrode surface on negative domains

#### References

- <sup>1</sup> Kalinin, S. V.; Bonnell, D. A. *Physical Review B* 2001, 12, 125411-125413
- <sup>2</sup> Jones, P. M.; Dunn, S. *Nanotechnology* 2007, 18, 185702-185708
- <sup>3</sup> Zhang, Q.; Huang, Z.; Vickers, M. E.; Whatmore, R. W. *Journal of European Ceramic Society* 1999, 14, 1417-1421
- <sup>4</sup> Scott, J. F. *Japanese Journal of Applied Physics* 1999, 22, 2272-2274

Contact Details: paul.jones@cranfield.ac.uk, Tel. 01234 750111 ext 2722  
Nanotechnology Centre, Building 70, Cranfield University, Beds, MK43 0AL.  
www.cranfield.ac.uk/sas